

REPORT DOCUMENTATION PAGE				Form Approved OMB No. 0704-0188	
<small>maintaining the data needed, and completing and reviewing the collection of information. Send comments regarding this burden estimate or any other aspect of this collection of information, including suggestions for reducing the burden, to Department of Defense, Washington Headquarters Services, Directorate for Information Operations and Reports (0704-0188), 1215 Jefferson Davis Highway, Suite 1204, Arlington, VA 22202-4302. Respondents should be aware that notwithstanding any other provision of law, no person shall be subject to any penalty for failing to comply with a collection of information if it does not display a currently valid OMB control number. PLEASE DO NOT RETURN YOUR FORM TO THE ABOVE ADDRESS.</small>					
1. REPORT DATE (DD-MM-YYYY) 10-07-2003		2. REPORT TYPE Final Report		3. DATES COVERED (From - To) 23-Oct-01 - 23-Apr-03	
4. TITLE AND SUBTITLE  Experimental And Theoretical Study Of Hypersonic Laminar Flow Control Using Ultrasonically Absorptive Coatings (UAC)			5a. CONTRACT NUMBER ISTC Registration No: N2172		
			5b. GRANT NUMBER		
			5c. PROGRAM ELEMENT NUMBER		
			5d. PROJECT NUMBER		
6. AUTHOR(S)  Dr. Anatoly Maslov			5d. TASK NUMBER		
			5e. WORK UNIT NUMBER		
7. PERFORMING ORGANIZATION NAME(S) AND ADDRESS(ES) Institute of Theoretical and Applied Mechanics Institutsкая 4/1 Novosibirsk 630090 Russia				8. PERFORMING ORGANIZATION REPORT NUMBER  N/A	
9. SPONSORING/MONITORING AGENCY NAME(S) AND ADDRESS(ES)  EOARD PSC 802 BOX 14 FPO 09499-0014				10. SPONSOR/MONITOR'S ACRONYM(S)	
				11. SPONSOR/MONITOR'S REPORT NUMBER(S) ISTC 01-7005	
12. DISTRIBUTION/AVAILABILITY STATEMENT  Approved for public release; distribution is unlimited. /					
<div style="font-size: 2em; font-weight: bold;">20040625 102</div>					
13. SUPPLEMENTARY NOTES					
14. ABSTRACT  This report results from a contract tasking Institute of Theoretical and Applied Mechanics as follows: The project is focused on detail experimental and theoretical studies of hypersonic laminar flow control using ultrasonically absorptive coatings (UAC) of regular porosity. Parametrical calculations of boundary layer stability on porous and solid walls will be conducted and compared with the experimental data to be obtained using the artificial wave-packet method and hot-wire measurements. The experimental investigations will be performed in the blow-down wind tunnel T-326 in Hypersonic Flow Laboratory of ITAM SB RAS at Mach 6. Both natural and artificially excited disturbances will be investigated on solid and porous surfaces of a sharp cone model. Detailed experimental data on transition loci, characteristics of natural and artificially excited disturbances will be obtained. This will allow us to perform direct validation of theoretical modeling and verify the experimental data previously obtained. Results of this project will provide a launching pad for future efforts including breadboard validation of UAC concept for the laminar flow control on blunt bodies, rough surfaces etc.					
15. SUBJECT TERMS EOARD, Aviation Technology, Aircraft					
16. SECURITY CLASSIFICATION OF:			17. LIMITATION OF ABSTRACT		18. NUMBER OF PAGES
a. REPORT UNCLAS	b. ABSTRACT UNCLAS	c. THIS PAGE UNCLAS	UL		19a. NAME OF RESPONSIBLE PERSON Wayne A. Donaldson
					19b. TELEPHONE NUMBER (Include area code) +44 (0)20 7514 4299

**ISTC 2172-2001**

**Final  
Project Technical Report  
of ISTC 2172-2001**

**Experimental and theoretical studies of hypersonic laminar flow  
control using ultrasonically absorptive coatings (UAC)**

**Anatoly Alexandrovich Maslov  
(Project Manager)  
Institute of Theoretical and Applied Mechanics  
Russian Academy of Sciences, Siberian Branch**

**May 2003**

---

**This work was supported financially by European Office of Aerospace Research and Development and performed under the contract to the International Science and Technology Center (ISTC), Moscow.**

ISTC 2172-2001

**Experimental and theoretical studies of hypersonic laminar flow control using ultrasonically absorptive coatings (UAC)**

Anatoly Alexandrovich Maslov (Project Manager)  
Institute of Theoretical and Applied Mechanics \*

The objective of this project is the experimental and theoretical research of hypersonic laminar flow control using ultrasonically absorptive coatings of regular porosity.

**Major results:**

- Data on benchmark measurements of sound-absorption properties of arbitrary porous materials
- Theoretical data on acoustic properties of cylindrical pores including the gas rarefaction effect associated with Knudsen layer on the pore wall. It is shown that the UAC of regular microstructure, namely, the metal sheet perforated by equally spaced cylindrical blind holes of 450 mkm depth and 50 mkm diameter (spacing between holes 100 mkm), stabilizes the second mode. Parametric studies (performed for a 7 half-angle sharp cone at freestream Mach number 6) indicate that the UAC stabilization effect is much stronger on the cooled wall than on the adiabatic wall. The former case is more practical, since actual hypersonic vehicles have the wall temperature substantially lower than the adiabatic wall temperature.
- Mach=6 wind tunnel data on stability of hypersonic boundary layer on the porous and solid walls of a sharp cone. These data were obtained for natural disturbances and artificially excited wave-packets. It is shown that the porous coating stabilizes the second mode and weakly affect the first mode.
- The theoretical predictions of the UAC acoustic characteristics agree with the benchmark data.
- The theoretical predictions of the second-mode amplification on the solid and porous walls agree with the wind-tunnel data obtained for natural and artificial disturbances.
- Experimental and theoretical results may be used for design and testing of UAC with regular microstructures for hypersonic laminar flow control.

Keywords (about 10 words): Hypersonic flow, Boundary layer, Laminar-turbulent transition, Hot-wire anemometry, Coating with regular porosity, Ultrasonic absorption, Rarefaction effects, Stability, Laminar-flow control.

---

\*630090, Novosibirsk, Institutskaya st. 4/1, Russia

Phone +7-(383-2) 30-42-79 Fax +7-(383-2) 34-22-68

E-mail: admin@itam.nsc.ru

**The work has been performed by  
the following institutes and collaborators.**

**1. Participated institutes:**

**1.1 Leading institute:**

**Institute of Theoretical and Applied Mechanics**

**630090, Novosibirsk, Institutskaya st. 4/1, Russia**

**Phone +7-(383-2) 30-42-79 Fax +7-(383-2) 34-22-68**

**E-mail: admin@itam.nsc.ru**

**1.2 Subcontracted institutes: No**

**2. Foreign Collaborators**

**European Office of Aerospace Research and Development**

**223-231 Old Marylebone Road, London, United Kingdom, NW1 5TH**

**Phone +44 (0) 20 7514 4953, Fax +44 (0) 20 7514 4960**

**Email: rphillips@eoard.af.mil**

## **PROJECT MANAGER**

Professor Anatoly Maslov

Deputy Director of ITAM

**Address:** Institute of Theoretical and Applied Mechanics, Institutskaya st. 4/1, Novosibirsk,  
630090, Russia

**Telephone:** 7-(383-2)-30-38-80

**Fax:** 7-(383-2)-34-22-68

**e-mail:** maslov@itam.nsc.ru

## **Investigators:**

Dr. A.V. Fedorov

Dr. V.F. Kozlov

Dr. S.G. Mironov

Dr. A.N. Shplyuk

Post graduate student I.S. Tsyrlnikov

Post graduate student E.V. Burov

Eng. Boris Sapogov

## Abstract

Experimental and theoretical studies of hypersonic boundary-layer stabilization using a passive ultrasonically absorptive coating (UAC) of regular microstructure were conducted in order to evaluate the UAC performance for hypersonic laminar-flow control. The coating is a porous sheet perforated with equally spaced blind cylindrical holes of the average pore diameter  $50\text{ }\mu\text{m}$ , depth  $450\text{ }\mu\text{m}$  and average spacing  $100\text{ }\mu\text{m}$ . This coating is similar to that tested in the GALCIT T-5 shock tunnel of California Institute of Technology. Linear stability problem for hypersonic boundary layers on the porous wall was formulated using the boundary conditions, which simulate absorption of disturbance energy by a porous layer. These boundary conditions result from modeling of acoustic disturbances propagating inside a long cylindrical pore. Solutions for the dynamic density and dynamic compressibility are refined to account for the gas rarefaction effect associated with Knudsen layers on the pore walls. Parametric calculations of the UAC effect on the second-mode stability are performed for a sharp cone at freestream Mach number  $\approx 6$ . It is shown that the UAC strongly stabilizes the second mode in the cold-wall case typical for practical applications. Benchmark measurements of acoustic absorption by the porous coating are conducted using the acoustic interferometer developed in ITAM. These measurements agree well with theoretical predictions of the UAC impedance and absorption coefficient. The theoretical model gives a similarity law, which allows for extrapolation of benchmark data to low pressures and high frequencies typical for experiments in hypersonic wind tunnels and flight. Stability experiments are performed on a  $7^\circ$  half-angle sharp cone in the T-326 wind tunnel at freestream Mach number 5.95. The cone has a longitudinal half of its surface solid and the other the porous coating. Hot-wire measurements of natural and artificially excited disturbances are conducted on both porous and solid sides of the model. Analysis of mean profiles and RMS mass-flow pulsations show that the UAC roughness does not cause premature tripping of the boundary layer. Natural disturbance spectra indicate that the second mode is a dominant instability. The UAC stabilizes the second mode and weakly affects the first mode that is consistent with the theoretical predictions. Measurements of artificially excited wave packets show that the UAC leads to substantial decreasing of the wave-packet growth. The experimental data on phase speeds and amplitudes of the second-mode disturbances are compared with theoretical predictions. Satisfactory agreement is obtained on both solid and porous surfaces. The linear stability theory, benchmark measurements and wind-tunnel experiments confirm the concept of hypersonic boundary-layer stabilization using passive porous coatings of regular microstructure. Theoretical and experimental results of this effort can be used for evaluation of the UAC performance and design of hypersonic laminar flow control systems.

## **Acknowledgements**

This effort was performed at the Institute of Theoretical and Applied Mechanics SB RAS under International Science And Technology Center (ISTC) partner grant No. 1863. The funding was provided by the European Office of Aerospace Research and Development (EOARD). The authors are grateful for support of this research project to Dr. John D. Schmisser, Dr. Steven Walker and Dr. Wayne Donaldson. The authors are thankful to Dr. Norman Malmuth for fruitful discussions and Mr. Vladimir Kiselev who served as the tunnel technician over many hours of wind tunnel testing.

## Table of Contents

Nomenclature	9
Introduction	11
Chapter I. Theoretical modeling of UAC Performance	13
1.1. Linear Stability Analysis	13
1.1.1. Mean flow	13
1.1.2. Linear stability problem	14
1.2. Acoustic properties of UAC	17
1.2.1. Background	18
1.2.2. Problem formulation	18
1.2.3. Solution of the problem	20
1.2.4. Numerical examples	21
1.2.5. Admittance of porous layer	24
1.3. Parametric studies of the UAC effect on the second mode	25
1.3.1. Basic parameters and mean flow	25
1.3.2. Stability characteristics for adiabatic wall	28
1.3.3. Stability characteristics for cold wall	32
1.3.4. Rarefaction effect	38
1.4. Summary	41
Chapter II. Benchmark Measurements of UAC Characteristics	42
2.1. Modeling of acoustic propagation in porous materials	42
2.2. Measurement of propagation constant, acoustic resistance, and sound-absorption coefficient	47
2.3. Summary	56
Chapter III. Wind Tunnel Experiments and Comparison with Theory	57
3.1. Experimental model	57



3.1.1. Perforated sheet	58
3.1.2. Technology of manufacturing	60
3.2. Experimental equipment and techniques	63
3.2.1. Wind tunnel	63
3.2.2. Alignment of the model at zero angles	63
3.2.3. Traverse system	64
3.2.4. Hot-wire anemometer system	64
3.2.5. System of measurement control and data acquisition	65
3.2.6. The system of high-frequency glow discharge	66
3.2.7. Processing of wave characteristics of the disturbances	66
3.2.8. Measurements of natural and artificial disturbances	67
3.3. Results of measurements	68
3.3.1. Mean flow	68
3.3.2. Natural disturbances	68
3.3.3. Artificial wave packets	69
3.4. Comparison with linear stability theory	70
3.5. Summary	71
Conclusions	96
Future Effort	98
References	99
Appendix	103

# Nomenclature

## For Chapters I and III

$A$	= disturbance amplitude
$A_x, A_y, A_z$	= admittance components
$A_\theta$	= thermal admittance
$\tilde{C}$	= dynamic compressibility
$C_p$	= specific heat capacity under constant pressure
$C_X$	= longitudinal phase velocity of the wave packet
$f$	= frequency
$F$	= $\omega^* \nu_e^* / U_e^{*2}$ frequency parameter
$h$	= porous layer thickness
$Kn$	= Knudsen number
$l^*$	= $\sqrt{\nu_e^* L^* / U_e^*}$
$M$	= Mach number
$m$	= propagation constant
$p$	= pressure disturbance
$P$	= mean pressure
$P_0$	= stagnation pressure
$Pr$	= Prandtl number
$Q$	= mass flow disturbance
$r_0$	= pore radius
$R$	= $\sqrt{U_e^* L^* / \nu_e^*}$
$Re$	= Reynolds number
$Re_1$	= unit Reynolds number
$s$	= pore spacing
$SA, SF$	= amplitude and phase spectra with respect to the transversal wave number $\beta$
$SA_0$	= value of $SA$ at $\beta=0$
$T$	= temperature
$T_0$	= stagnation temperature
$u, v, w$	= velocity disturbance
$U, V$	= mean-flow velocity components
$x, y, z$	= Cartesian coordinates
$X, Y, Z$	= hot-wire coordinates
$Z_0$	= characteristic impedance
$\alpha, \beta$	= wavenumber components
$\delta$	= boundary-layer thickness
$\delta^*$	= boundary-layer displacement thickness
$\varepsilon$	= $l^* / L^*$ small parameter
$\gamma$	= specific heat ratio
$\rho$	= density
$\tilde{\rho}$	= dynamic density
$\kappa$	= heat conductivity

## For Chapter II

$C$	= complex compressibility
$c$	= speed of sound
$d$	= diameter of the interferometer tube
$f$	= frequency
$H$	= $r_0\sqrt{\rho_0\omega/\eta}$ scale parameter
$h$	= porous-layer thickness
$k$	= wave number
$k_0$	= structural constant
$k_1$	= added mass coefficient
$L$	= length of the interferometer tube
$n$	= standing wave factor
$P$	= pressure
$Pr$	= Prandtl number
$q$	= pore length
$r_0$	= pore radius
$s$	= thickness of the porous sample
$s_h$	= shape factor
$W$	= wave resistance
$Z$	= specific impedance
$Z_{ex}$	= input impedance
$\alpha$	= absorption coefficient
$\rho$	= complex dynamic density
$\omega$	= angular frequency
$\phi$	= porosity
$\sigma$	= flow resistance
$\eta$	= viscosity
$\varphi$	= absorption phase
$\lambda$	= wavelength
$\gamma$	= specific heat ratio
$\Gamma$	= propagation constant

## List of Acronyms

ADC	analog-digital converter
CCA	constant current anemometer
ITAM	Institute of Theoretical and Applied Mechanics, Russia
PSE	parabolized stability equations
RMS	root-mean-square
UAC	ultrasonically absorptive coating

## Introduction

Laminar-turbulent transition leads to substantial increase of the aerodynamic drag and surface heating of hypersonic vehicles (Lin et al., 1984; Tartabini et al., 2000). Transition also affects engine performance and aerodynamic control. The ability to increase the laminar run is of critical importance in design and optimization of aerospace planes. Estimates for the National Aerospace Plane (Whitehead, 1989) indicated that payload-to-gross-weight ratio would nearly double if the boundary layer on the vehicle surface were fully laminar, compared to fully turbulent.

Aspects of hypersonic boundary-layer transition control are discussed by Kimmel (2003). Smoothing and shaping of the vehicle surface help to avoid early transition due to roughness, leading-edge contamination as well as cross-flow and Görtler instabilities. However, with these measures the laminar run may still be short because of the first and/or second mode amplification (Mack, 1984; Malik et al., 1990). The wall cooling, which naturally occurs on hypersonic vehicle surfaces, strongly stabilizes the first mode (Lysenko & Maslov, 1984) while destabilizes the second mode (Malik, 1989). This indicates that hypersonic laminar flow control concepts should address the second-mode instability, especially for cruise airbreathers, due to the extended period of hypersonic flight at relatively small angle of attack. Since these vehicles have predominantly planar shape with sharp leading edges and the local Mach numbers are high ( $M_e > 6$ ), the second mode may be a dominant instability leading to laminar-turbulent transition.

The second mode is the result of an inviscid instability present due to a region of supersonic mean flow relative to the disturbance phase velocity. This mode belongs to the family of trapped acoustic modes propagating in a wave-guide between the wall and the sonic line (Mack, 1984; Guschin & Fedorov, 1989). The existence of the second mode was established by the experiments of Kendall (1975), Demetriades (1974), Stetson *et al.* (1983, 1992), and Kimmel *et al.* (1995). Once the second mode sets in, it becomes the dominant instability since its growth rate tends to exceed that of the first mode. For insulated surfaces, this occurs for Mach number larger than 4. For cooled surfaces, the second mode can dominate at even lower Mach numbers (Lysenko & Maslov, 1984).

In high-speed flows, the second mode is associated with disturbances of relatively high frequency corresponding to the ultrasonic band. Malmuth *et al.* (1998) assumed that a passive ultrasonically absorptive coating (UAC) of fine porosity may suppress these fluctuations and, at the same time, may not trip the boundary layer due to roughness effects; *i.e.*, the passive UAC may stabilize the second mode by a disturbance energy extraction mechanism. This hypothesis was examined by the inviscid linear stability analysis. Using the WKB method, Malmuth *et al.* (1998) formulated the boundary condition on an ultrasonically absorptive wall for the second and higher modes, and showed that the absorption does cause a strong stabilization of the second mode. Later, Fedorov & Malmuth (2001) analyzed the absorption effect at finite Reynolds numbers using viscous linear stability theory and found that viscosity weakly affects the stabilization mechanism. They also considered an ultrasonically absorptive surface of a particular type; namely, the wall covered by a porous coating with cylindrical blind micro-holes, and showed that a relatively thin coating (of the thickness  $\sim 0.1$  of the boundary-layer displacement thickness) can dramatically reduce the second-mode growth rate.

These theoretical findings led to the expectation that a passive porous coating may be exploited for hypersonic laminar flow control. The concept was verified in the GALCIT T-5 shock tunnel of Caltech (Rasheed *et al.*, 2001) by testing a  $5^\circ$  half-angle sharp cone. The cone has a longitudinal half of its surface solid and the other a porous sheet perforated with equally spaced

blind cylindrical holes of the average pore diameter 60  $\mu\text{m}$ , depth 500  $\mu\text{m}$  and average spacing 100  $\mu\text{m}$ . The model was instrumented by thermocouples, and the transition onset point was determined from the Stanton number distributions measured simultaneously on both sides of the model for each run. The experiments were performed for the ranges of the freestream total enthalpy  $4.18 \leq H_0 \leq 13.34$  MJ/kg and the freestream Mach number  $4.59 \leq M_\infty \leq 6.4$ . The porous coating delayed transition by a significant amount. For the majority of runs, the boundary layer on the porous surface was laminar up to the model base, while transition on the solid surface was observed at a half of the cone length. The experiments qualitatively confirmed the theoretical prediction of Fedorov & Malmuth (2001). However, quantitative comparison was not feasible because the cone was not long enough to measure the transition locus on the porous surface. Since the boundary-layer disturbances were not measured, these experiments did not give direct evidence of the second-mode instability, and its effect on the transition process was not clear. This motivated us to perform a series of stability experiments on sharp cones covered by porous coatings of various microstructures. Further theoretical research was also needed to address randomly porous coatings as well as to account for rarefied gas effects on the UAC performance.

The first series of stability experiments (Fedorov et al., 2003a,b) was conducted in the Mach 6 wind tunnel of the Institute Theoretical of Applied Mechanics (ITAM, Novosibirsk, Russia) on a  $7^\circ$  half-angle sharp cone whose longitudinal half surface was solid and other half surface was covered by a thin porous coating of random structure, namely, a fibrous absorbent material (felt metal). Hot-wire measurements of natural disturbances and artificially excited wave packets were performed on both solid and porous surfaces. Stability analyses for 2-D and 3-D disturbances showed that the porous coating stabilizes the second mode and marginally destabilizes the first mode. These results are in a qualitative agreement with the experimental data for natural disturbances. The theoretical predictions (including nonparallel effects) are in a good quantitative agreement with the stability measurements for artificially excited wave packets associated with the second mode (Fedorov et al., 2003a,b).

In this report, we discuss stability experiments and calculations, which has been performed for a  $7^\circ$  half-angle sharp cone with the porous coating of regular microstructure similar to that tested in the GALCIT T-5 shock tunnel (Rasheed et al., 2001). In Chapter I we: formulate stability problem for disturbances in the boundary layer on porous wall; investigate propagation of disturbances within pores including the gas rarefaction effect and specify boundary conditions for the boundary-layer disturbances on the UAC surface; perform parametric studies of the UAC stabilization effect on the second mode. In Chapter II we present benchmark measurements of UAC characteristics and their comparisons with the theoretical model. In Chapter III we: discuss experimental setup, a sharp cone model and instrumentation; describe the measurement techniques and data processing; present results of stability measurements for natural and artificial disturbances, compare experimental data with predictions of linear stability theory. Then we conclude the report and discuss future efforts.

# Chapter I. Theoretical modeling of UAC Performance

## 1.1. Linear Stability Analysis

### 1.1.1. Mean flow

For the laminar boundary layer on a flat plate or a sharp cone at zero angle of attack, equations are written in the self-similar form (Hayes & Probstein, 1959)

$$(Cf'')' + ff'' = 0, \quad (1.1)$$

$$\left(\frac{C}{\text{Pr}}g'\right)' + fg' + \frac{U_e^{*2}}{H_e^*} \left[ C \left(1 - \frac{1}{\text{Pr}}\right) f'f'' \right]' = 0, \quad (1.2)$$

$$C = \frac{\rho^* \mu^*}{\rho_e^* \mu_e^*}, \quad \frac{U_e^{*2}}{H_e^*} = \frac{(\gamma - 1)M_e^2}{1 + \frac{\gamma - 1}{2}M_e^2}, \quad \frac{\rho_e^*}{\rho^*} = \left(1 + \frac{\gamma - 1}{2}M_e^2\right)g - \frac{\gamma - 1}{2}M_e^2 f'^2. \quad (1.3)$$

Here  $f'(\eta) = U^*/U_e^*$ ,  $g(\eta) = H^*/H_e^*$ ,  $\rho$ ,  $\mu$ ,  $\text{Pr}$  and  $\gamma$  are the streamwise velocity, total enthalpy, density, viscosity, Prandtl number and specific heat ratio, respectively; primes denote differentiation with respect to  $\eta$ ; asterisk stands for dimensional quantities. The independent variables are given by the Howarth-Dorodnitsyn transformations and Mangler transformation of coordinates

$$\xi = \int_0^x \rho_e^* \mu_e^* U_e^{*2} r_w^{*2j} dx^*, \quad \eta = \frac{U_e^* r_w^{*j}}{\sqrt{2\xi}} \int_0^y \rho^* dy^*, \quad (1.4)$$

where  $x$  is coordinate along an external streamline;  $y$  is coordinate normal to the body surface;  $r_w$  is distance from the symmetry axis to the wall surface;  $j = 0$  for planar flow and  $j = 1$  for axisymmetric flow. It is assumed that the porous coating weakly affects the mean flow weakly, and the standard boundary conditions are imposed on the wall surface

$$\eta = 0: f = f' = 0, g = g_w \text{ (or } g' = 0 \text{ for adiabatic wall)}, \quad (1.5)$$

$$\eta \rightarrow \infty: f' = 1, g = 1. \quad (1.6)$$

In all calculations discussed hereafter, the fluid is a perfect gas of  $\gamma = 1.4$  and  $\text{Pr} = 0.708$ . The viscosity-temperature dependency is approximated by Sutherland's law

$$\mu(T) = \frac{(1 + S)}{(T + S)} T^{3/2}, \quad (1.7)$$

where  $S = 110/T_e^*$ ;  $\mu = \mu^*/\mu_e^*$  and  $T = T^*/T_e^*$  are nondimensional viscosity and temperature.

### 1.1.2. Linear stability problem

Stability analysis includes nonparallel effects associated with downstream growth of the boundary-layer thickness. Effects relevant to the cone surface curvature and conical divergence of streamlines are neglected. The analysis is based on the method of multiple scales applied by Gaster (1974) to incompressible boundary layers and extended by Padhye & Nayfeh (1979) to compressible flows. This method (with insignificant variations) has been used to investigate the nonparallel effect on stability of supersonic boundary layers (Gaponov, 1980; El-Hady, 1980; Tumin & Fedorov, 1982). Its extension to the case of multiple modes was discussed by Zhigulev & Tumin (1982) and Fedorov & Khokhlov (2002).

Following Fedorov & Khokhlov (2002) we outline the nonparallel linear stability analysis for a monochromatic wave. The coordinates  $(x, y, z)$  are made nondimensional using the boundary-layer scale  $l^* = \sqrt{\nu_e^* L^* / U_e^*}$ , where the distance  $L^*$  from the leading edge is assumed to be much larger than  $l^*$ , and the ratio  $\varepsilon = l^* / L^*$  is treated as a small parameter. Time  $t$  and pressure  $P$  are referenced to  $l^* / U_e^*$  and  $\rho_e^* U_e^{*2}$  respectively; other flow characteristics are made nondimensional using their quantities at the upper boundary-layer edge. Introducing the slow variable,  $x_1 = x^* / L^* = \varepsilon x$ , we specify the mean-flow velocity components  $(U, V)$  and temperature  $T$  as

$$U = U(x_1, y), \quad V = \varepsilon V_0(x_1, y), \quad T = T(x_1, y). \quad (1.8)$$

A monochromatic disturbance is represented by the vector function

$$\mathbf{Z} = (u, \frac{\partial u}{\partial y}, v, p, \theta, \frac{\partial \theta}{\partial y}, w, \frac{\partial w}{\partial y})^T, \quad (1.9)$$

$$\mathbf{Z}(x, y, z, t) = \mathbf{F}(x, y) \exp(i\beta z - i\omega t),$$

where  $u, v, w, p$  and  $\theta$  are velocity components, pressure and temperature;  $\beta = \beta^* l^*$  and  $\omega = \omega^* l^* / U_e^*$ . The amplitude vector-function  $\mathbf{F}(x, y)$  satisfies a system of partial differential equations that resulted from Fourier transform of the linearized Navier-Stokes equations with respect to time and  $z$ -coordinate. These equations with the boundary conditions are written in the matrix-operator form

$$\mathbf{H}(y, \partial_y, x_1, \varepsilon \partial_{x_1}, \omega, \beta) \mathbf{F} = 0. \quad (1.10)$$

$$y = 0: F_1 = A_x F_4, F_3 = A_y F_4, F_5 = A_\theta F_4, F_7 = A_z F_4, \quad (1.11)$$

$$y \rightarrow \infty: F_1, F_3, F_5, F_7 \rightarrow 0. \quad (1.12)$$

Here the admittance components  $A_x, A_y, A_z$  and the thermal admittance  $A_\theta$  are complex quantities, which couple velocity and temperature disturbances with the pressure disturbance on the porous surface. The admittances depend on properties of the porous material, mean-flow characteristics on the wall surface, and disturbance frequency. These dependencies are specified in Section 1.2 for the UAC of regular microstructure. On the solid wall  $A_x = A_y = A_z = A_\theta = 0$ , which corresponds to no-slip conditions and zero temperature

perturbation on the surface of high thermal conductivity.

We consider a partial solution of the problem (1.10)-(1.12), which is a discrete mode of the complex eigenvalue  $\alpha(x_1, \beta, \omega)$ . The amplitude vector-function is expressed in the form

$$\mathbf{F} = (\mathbf{F}_0 + \varepsilon \mathbf{F}_1 + \dots) \exp(i\varepsilon^{-1}S), \quad S = \int \alpha(x_1) dx_1. \quad (1.13)$$

Substituting (1.13) into (1.10)-(1.12) and grouping terms of the same order of magnitude with respect to  $\varepsilon$  we obtain a sequence of problems for  $\mathbf{F}_j(x_1, y)$ ,  $j = 0, 1, \dots$ . In the zero-order approximation, the eigenvalue problem is written as

$$\left( \frac{\partial}{\partial y} - \mathbf{H}_0 \right) \mathbf{F}_0 = 0, \quad (1.14)$$

$$y = 0: F_{01} = A_x F_{04}, F_{03} = A_y F_{04}, F_{05} = A_\theta F_{04}, F_{07} = A_z F_{04}, \quad (1.15)$$

$$y \rightarrow \infty: F_{01}, F_{03}, F_{05}, F_{07} \rightarrow 0. \quad (1.16)$$

This problem describes stability of a locally parallel mean flow. Here the matrix  $\mathbf{H}_0$  has dimension  $8 \times 8$ ; its non-zero elements are given in Appendix. Solution of the problem (1.14)-(1.16) is expressed in the form

$$\mathbf{F}_0 = c(x_1) \zeta(x_1, y, \alpha), \quad (1.17)$$

where  $\zeta$  is eigenvector normalized by the condition  $\zeta_4(x_1, 0, \alpha) = 1$ ; i.e., the pressure-disturbance amplitude on the wall surface is  $c(x_1)$ . For spatial instability of two-dimensional boundary layers, the angular frequency  $\omega$  and the transverse wavenumber component  $\beta$  are real, whereas  $\alpha$  is a complex eigenvalue. If  $\text{Im } \alpha < 0$ , then the disturbance amplifies downstream with the spatial growth rate  $\sigma = -\alpha_i$ . The amplitude coefficient  $c(x_1)$  is determined from the first-order approximation, which leads to the inhomogeneous problem

$$\left( \frac{\partial}{\partial y} - \mathbf{H}_0 \right) \mathbf{F}_1 = -i \frac{\partial \mathbf{H}_0}{\partial \alpha} \frac{\partial \mathbf{F}_0}{\partial x_1} + \mathbf{H}_1 \mathbf{F}_0, \quad (1.18)$$

$$y = 0: F_{11} = A_x F_{14}, F_{13} = A_y F_{14}, F_{15} = A_\theta F_{14}, F_{17} = A_z F_{14}, \quad (1.19)$$

$$y \rightarrow \infty: F_{11}, F_{13}, F_{15}, F_{17} \rightarrow 0. \quad (1.20)$$

The right-hand side of (1.18) is associated with the nonparallel effect; the vector  $\mathbf{G} = \mathbf{H}_1 \mathbf{F}_0$  is given in Appendix. The problem (1.18)-(1.20) has a nontrivial solution if its right-hand side is orthogonal to the eigenvector  $\xi(x_1, y, \alpha)$  of the adjoint problem

$$\left( \frac{\partial}{\partial y} + \mathbf{H}_0^T \right) \bar{\xi} = 0, \quad (1.21)$$



$$y = 0: \bar{\xi}_2 = \bar{\xi}_6 = \bar{\xi}_8 = 0, \bar{\xi}_4 + A_x \bar{\xi}_1 + A_y \bar{\xi}_3 + A_\theta \bar{\xi}_5 + A_z \bar{\xi}_7 = 0, \quad (1.22)$$

$$y \rightarrow \infty: \bar{\xi}_2, \bar{\xi}_4, \bar{\xi}_6, \bar{\xi}_8 \rightarrow 0, \quad (1.23)$$

where the overbar denotes a complex conjugate value. The orthogonality condition leads to the ordinary differential equation for the amplitude function  $c(x_1)$

$$\left\langle \xi, \frac{\partial \mathbf{H}_0}{\partial \alpha} \zeta \right\rangle \frac{dc}{dx_1} = \left[ - \left\langle \xi, \frac{\partial \mathbf{H}_0}{\partial \alpha} \frac{\partial \zeta}{\partial x_1} \right\rangle - i \left\langle \xi, \mathbf{H}_1 \zeta \right\rangle \right] c, \quad (1.24)$$

where the scalar product is defined as

$$\langle \mathbf{f}, \mathbf{g} \rangle = \int_0^\infty \sum_{j=1}^8 \bar{f}_j g_j dy. \quad (1.25)$$

Substituting solution of (1.24) into (1.17) and (1.13), we express the amplitude vector in the form

$$\mathbf{F} = [c_0 \zeta(x_1, y) + O(\varepsilon)] \exp \left( i\varepsilon^{-1} \int [\alpha(x_1) + \varepsilon W(x_1) + O(\varepsilon^2)] dx_1 \right), \quad (1.26)$$

$$W(x_1) = \frac{i \left\langle \xi, \frac{\partial \mathbf{H}_0}{\partial \alpha} \frac{\partial \zeta}{\partial x_1} \right\rangle - \langle \xi, \mathbf{H}_1 \zeta \rangle}{\left\langle \xi, \frac{\partial \mathbf{H}_0}{\partial \alpha} \zeta \right\rangle}, \quad (1.27)$$

where  $c_0$  is constant. The amplification rate of any physical quantity can be calculated using (1.26) and (1.27). For example, the  $x$ -component of mass flow disturbance is

$$Q(x_1, y) = [c_0 q(x_1, y) + O(\varepsilon)] \exp \left( i\varepsilon^{-1} \int [\alpha(x_1) + \varepsilon W(x_1) + O(\varepsilon^2)] dx_1 \right), \quad (1.28)$$

$$q = [\zeta_1 + (\gamma M_e^2 \zeta_4 - \zeta_5 / T) U] / T. \quad (1.29)$$

The disturbance growth rate is a logarithmic derivative of (1.28), which is expressed in the form

$$\sigma(x_1, y) = -\alpha_i + \varepsilon \left( \frac{\partial \ln |q(x_1, y)|}{\partial x_1} - W_i \right) + O(\varepsilon^2). \quad (1.30)$$

Due to the nonparallel effect, the growth rate depends on the vertical coordinate  $y$ . In accordance with the experimental measurements of Chapter III,  $\sigma(x_1, y)$  is calculated at  $y = y_m$  relevant to the maximum of mass-flow disturbance in the boundary layer. This maximum lies in the critical layer, where the mean-flow velocity is close to the phase velocity.

The zero-order and first-order approximations of  $\sigma$  were validated by comparison with the experimental data of Kendall (1967) and the calculations of Chang *et al.* (1991) performed in the framework of linear parabolized stability equations (PSE). Figure I.1 shows the first-mode growth rate as a function of the nondimensional frequency,  $F = \omega^* \nu_e^* / U_e^{*2}$ , for the boundary

layer on a flat plate at the Mach number  $M_e = 2.2$  and the Reynolds number  $R = \sqrt{U_e^* L^*} / \nu_e^* = 1000$ . The wave angle is  $\psi = \arctan(\beta / \alpha_r) = 60^\circ$  that approximately corresponds to most unstable waves. The results are in good agreement with the linear PSE calculations that confirms the method discussed above.

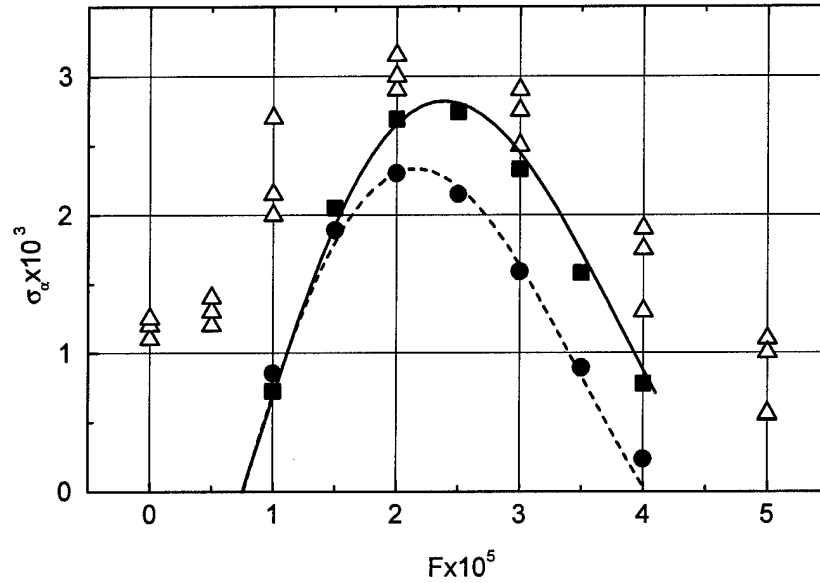


**Fig. 1.1.** The first-mode growth rate as a function of frequency; boundary layer on a flat plate at  $M_e = 2.2$ ,  $R = 1000$ , the wave angle  $\psi = \arctan(\beta / \alpha_r) = 60^\circ$ : triangles, the experiment of Kendall (1967); dashed line, parallel theory (pres.); solid circles, parallel theory, Chang et al. (1991); solid line, non-parallel theory (pres.); solid squares, non-parallel PSE, Chang et al. (1991).

## 1.2. Acoustic properties of UAC

In this section, the solution describing propagation of monochromatic acoustic waves inside a cylindrical pore filled with low-density gas is obtained. The analysis is focused on the most practical case, when corpuscular effects are appreciable only inside thin Knudsen layers forming on solid surfaces. Beyond Knudsen layers gas is treated as a continuum media. Its dynamics is governed by the linearized Navier-Stokes equations with the boundary conditions of the first-order approximation with respect to Knudsen number. The boundary conditions include a nonzero relative macroscopic gas velocity and temperature jumps on the pore surface. Acoustic properties of the perforated panel tested in the wind tunnel T-326 (see Chapter III) are discussed. It is shown that the rarefied gas effects can lead to essential changes of acoustic absorption in the range of nondimensional parameters relevant to the wind-tunnel conditions.

### 1.2.1. Background

Solutions of Navier-Stokes equations, which account for effects of energy dissipation in acoustic waves traveling inside a circular tube, are known since the latter half of XIX century (Kirchoff, 1868; Strutt, 1894). These solutions are widely used in analyses of acoustical properties of waveguides and perforated panels as well as in developments of semi-empirical models predicting sound absorption by rigid-frame porous media (Zwikker & Kosten, 1949; Biot, 1956a,b; Delany & Bazley, 1970; Attenborough, 1987; Johnson et al., 1987; Allard & Champoux, 1992).

The flow resistance and heat conductivity of micro-porous materials strongly depend on ambient pressure (Deryagin, 1946; Dulnev et al., 1974). This dependency is associated with molecular nature of gas inside the pores. The interaction of gas molecules with solid surfaces and molecular collisions in space obey different laws. This leads to formation of Knudsen layers on solid surfaces. The Knudsen layer thickness is of the order of molecular mean free path  $\lambda$ . Beyond the Knudsen layer, gas can be treated as a continuum media. However, molecular processes inside the Knudsen layer affect the boundary conditions. On macroscopic level, the rarefaction effects lead to slipping and temperature jumps on the interface boundaries.

Kundt & Warburg (1875) were the first who revealed experimentally the slipping in the gas outflow from a circular tube. They showed that the volume rate of laminar low-density gas flow inside the tube exceeded the volume rate predicted by the Poiseuille law. Maxwell (1952) gave qualitative explanation to this phenomenon by means of molecular-kinetic consideration. Smoluchowski (1899) discovered physical reasons causing the temperature discontinuity on the surface of a solid body submerged into non-uniformly heated gas of low density. Since the work of Kundt & Warburg (1875), the mentioned above effects were thoroughly investigated using experimental and theoretical methods. Detail reviews of these studies are given in (Goodman & Wachman, 1976; Patterson, 1956; Shidlovski, 1965) and many other monographs.

Since the molecular mean free path  $\lambda$  is inversely proportional to the pressure, the molecular effects become appreciable in the whole gas volume at sufficiently low pressures, and the described above model is invalid. However, in this case a contribution of the rarefied gas into averaged macroscopic properties of a porous material is, as a rule, so small that its theoretical modeling is not interesting for practice.

Slipping and temperature discontinuities on the interface boundaries are observed in media with non-uniform distributions of velocity and temperature. Such non-uniformities are continuously generated by acoustic waves propagating within pores. As a consequence, acoustic properties of porous media should be exposed to the molecular effects at sufficiently low pressures. For the T-326 wind tunnel conditions, the Knudsen number is  $Kn = \lambda / r_0 \sim 0.1$  ( $r_0$  is pore radius of the perforated sheet), and acoustic absorption of the porous layer may be quite different from that predicted in the framework of continuum fluid. Similar situations may occur in many practical cases such as propagation of sound in micro ducts. However, we have not found any publications on this subject. Hereafter we discuss results of our theoretical and experimental studies of the rarefaction effects on acoustic properties of the porous material comprising isolated cylindrical micro-pores.

### 1.2.2. Problem formulation

Consider propagation of a monochromatic acoustic wave inside an infinitely long circular tube of radius  $r_0$ , which represents an isolated pore. The tube is filled with gas of low density. The molecular effects are assumed to be appreciable in the Knudsen layer only. Beyond the Knudsen

layer and far from the tube ends, the disturbance generated by infinitesimal oscillating pressure gradient  $\text{Re}\{(d\tilde{p}/dz)\exp(i\omega t)\}$  is governed by the linearized momentum and energy equations. For the amplitudes of velocity  $\tilde{u}$  and temperature  $\tilde{T}$ , these equations can be written in the form

$$\begin{cases} \Delta \tilde{u} + \Lambda^2 \tilde{u} = \frac{1}{\mu} \frac{d\tilde{p}}{dz} , \\ \Delta \tilde{T} + \text{Pr} \Lambda^2 \tilde{T} = -\frac{i\omega}{\kappa} \tilde{p} , \end{cases} \quad (1.31)$$

where the  $z$ -axis is directed along the pore axis, the origin of the reference system is placed in the area center of the tube cross-section;  $i = \sqrt{-1}$ ,  $\omega = 2\pi f$  is circular frequency;  $\text{Pr}$  is Prandtl number ( $\text{Pr} = \mu c_p / \kappa$ );  $C_p$  is specific heat capacity under constant pressure;  $\mu$  and  $\kappa$  are dynamic viscosity and heat conductivity of gas inside the tube;  $\Lambda = \sqrt{-i\omega\rho_0 r_0^2 / \mu}$ ;  $\rho_0$  is gas density in equilibrium;  $\Delta = \frac{1}{r} \frac{\partial}{\partial r} \left( r \frac{\partial}{\partial r} \right)$  is Laplacian, where  $r$  is radius dimensionalized using the pore radius  $r_0$ .

In the first-order approximation with respect to small (but finite) Knudsen number, the boundary conditions are

$$u_g = -A_u \text{Kn} \left( \frac{\partial u}{\partial r} \right)_w, \quad (1.32a)$$

$$T_g = -A_E \frac{\text{Kn}}{\text{Pr}} \left( \frac{\partial T}{\partial r} \right)_w, \quad (1.32b)$$

where  $u_g$  and  $T_g$  are gas velocity and temperature on the solid surface; the dimensionless factors  $A_u$  and  $A_E$  depend, mainly, on laws of interaction between gas molecules and the solid surface; the subscript  $w$  denotes quantities on the pore wall.

In the framework of elementary kinetic theory (see, for example, Goodman & Wachman, 1976), the dimensionless coefficients  $A_u$ ,  $A_E$  and the Knudsen number  $\text{Kn}$  can be expressed in terms of the molecular tangential impulse  $\alpha_u$  and energy  $\alpha_E$  accommodation coefficients and other macroscopic parameters as

$$A_u = \alpha_u^{-1} - 0.5, \quad A_E = 2\gamma(\alpha_E^{-1} - 0.5)/(\gamma + 1),$$

$$\text{Kn} = 4\mu/(\rho_0 \bar{c} r_0),$$

where  $\gamma$  is specific heat ratio;  $\bar{c} = \sqrt{8R_g T_0 / \pi}$  is mean module of molecular velocity vector;  $R_g$  is gas constant per unit mass;  $T_0$  is gas temperature in equilibrium. In addition, we assume that the solid surface temperature  $T_w$  in (1.32b) is constant. The boundary conditions for more general cases, in particular, for rapidly varying wall temperature  $T_w$ , are given by Patterson

(1956) and Shidlovski (1965).

The discussed above formulation is based on the assumption that the Knudsen layer thickness is much less than the pore radius ( $\lambda \ll r_0$ ). This allows us to use the continuum media model beyond the Knudsen layers. However, besides the Knudsen number the problem depends on the ratio of the mean free path to the Stokes layer thickness  $\delta_a \sim \sqrt{\mu/\omega\rho_0}$ . As a result, the solution is a function of both  $Kn$  and the product  $Kn|\Lambda|$ , which should be small also. The condition  $Kn|\Lambda| \ll 1$  becomes important for disturbances of relatively high frequency, when the Stokes layer thickness is less (or much less) than the pore radius; i.e.,  $|\Lambda| > 1$ .

### 1.2.3. Solution of the problem

Using the substitutions, which are valid for the time factor  $\exp(i\omega t)$ ,

$$\tilde{u}(r, z) = -\frac{1}{i\omega\rho_0} \frac{d\tilde{p}}{dz} \{1 - F(r, B_u, \Lambda)\}, \quad (1.33)$$

$$\tilde{T}(r, z) = \frac{\tilde{p}}{\rho_0 C_p} \{1 - F(r, B_E, \Lambda\sqrt{\text{Pr}})\}, \quad (1.34)$$

where  $B_u = A_u Kn$ ,  $B_E = (A_E / \text{Pr}) Kn$ , we obtain that the function  $F(r, B, \zeta)$  is a solution of the Bessel equation

$$\left( \frac{1}{r} \frac{d}{dr} \left( r \frac{d}{dr} \right) + \zeta^2 \right) F(r, B, \zeta) = 0, \quad (1.35)$$

with the boundary condition

$$1 - F(1, B, \zeta) = B \frac{dF(r, B, \zeta)}{dr} \Big|_{r=1}. \quad (1.36)$$

Here  $B = B_u$  and  $\zeta = \Lambda$  in the expression (1.33) for the velocity amplitude;  $B = B_E$  and  $\zeta = \Lambda\sqrt{\text{Pr}}$  in the expression (1.34) for the temperature amplitude.

The solution of (1.35), (1.36) is expressed it terms of Bessel function of first kind of zero order

$$F(r, B, \zeta) = C J_0(\zeta r), \quad (1.37)$$

where  $C$  is integration constant, which is determined from the boundary condition (1.36) as

$$C = \frac{1}{J_0(\zeta)[1 - 0.5B\zeta^2 Q(\zeta)]}, \quad Q(\zeta) = \frac{2J_1(\zeta)}{\zeta J_0(\zeta)}. \quad (1.38)$$

Averaging (1.33)-(1.34) over the pore cross-section as  $\langle \tilde{f} \rangle = 2 \int_0^1 \tilde{f}(r) r dr$ , we obtain

$$\langle \tilde{u}(z) \rangle = -\frac{1}{i\omega\rho_0} \frac{d\tilde{p}}{dz} \{1 - \langle F(B_u, \Lambda) \rangle\}, \quad (1.39)$$

$$\langle \tilde{T}(z) \rangle = \frac{\tilde{p}}{\rho_0 C_p} \left\{ 1 - \left\langle F(B_E, \sqrt{\text{Pr}}\Lambda) \right\rangle \right\}, \quad (1.40)$$

Finally, using the general relations

$$i\omega\tilde{\rho}(\omega)\langle \tilde{u}(z) \rangle = -\frac{d\tilde{p}}{dz}, \quad (1.41)$$

$$\tilde{C}(\omega) = \rho_0^{-1} \left( \langle \tilde{\rho} \rangle / \tilde{p} \right) = \frac{1}{p_0} - \frac{\langle \tilde{T} \rangle}{T_0 \tilde{p}} = \frac{1}{p_0} \left( 1 - \frac{\rho_0 R \langle \tilde{T} \rangle}{\tilde{p}} \right), \quad (1.42)$$

where  $p_0$  is unperturbed ambient pressure, we can express the complex dynamic density  $\tilde{\rho}(\omega)$  and the dynamic compressibility  $\tilde{C}(\omega)$  as

$$\tilde{\rho}(\omega) = \rho_0 / \{1 - \langle F(B_u, \Lambda) \rangle\}, \quad (1.43)$$

$$\tilde{C}(\omega) = \frac{1}{\gamma p_0} \left\{ 1 + (\gamma - 1) \left\langle F(B_E, \sqrt{\text{Pr}}\Lambda) \right\rangle \right\}, \quad (1.44)$$

$$\langle F(B, \zeta) \rangle = \frac{Q(\zeta)}{1 - 0.5B\zeta^2 Q(\zeta)}. \quad (1.45)$$

In the case of  $\text{Kn} = 0$ , the formulas (1.43)-(1.45) coincide with (2.3), (2.4) discussed in Chapter II.

#### 1.2.4. Numerical examples

The absorptive coating tested in the benchmark experiments is a panel with equally spaced cylindrical pores of circular cross-section. The mean pore diameter is 60  $\mu\text{m}$ , the pore depth is 500  $\mu\text{m}$ , and the mean spacing between pores is 100  $\mu\text{m}$ . Schematic picture of this perforated panel is shown in Fig. I.2.

The theoretical expressions (2.43)-(2.45) for dynamic density and dynamic compressibility are used for evaluation of the ambient pressure effect on acoustic properties of the cylindrical pore. The Bessel functions of complex argument are calculated using the approximations of the Kelvin functions presented in (Abramowitz, & Stegun, 1964).

Calculations were conducted for pressures  $p_0 = 1.013$  and 10.13 kPa at the gas temperature  $T_0 = 288.16$  K. The disturbance frequency varied from 0.8 kHz to 10 kHz. The molecular tangential impulse ( $\alpha_u$ ) and energy ( $\alpha_E$ ) accommodation coefficients are  $\alpha_u = \alpha_E = 0.9$ . At the pressure 1.013 kPa, the Knudsen number is  $\text{Kn} = \lambda/r_0 = 4.2 \cdot 10^{-1}$ . For the majority of calculations,  $|\Lambda| < 1$  corresponds to low-frequency disturbances.

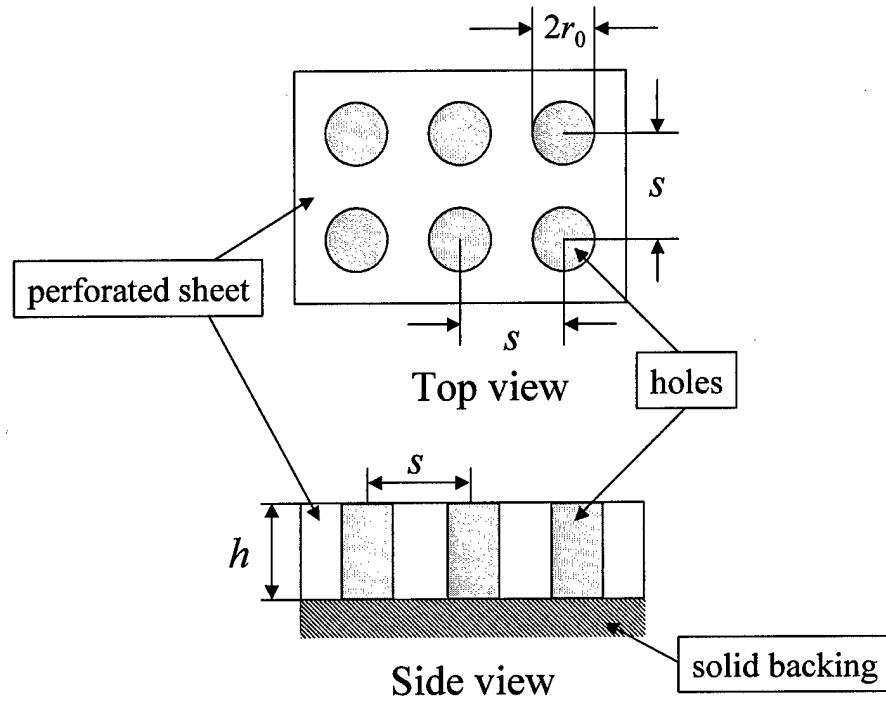


**Fig. I.2.** Schematic of the wall covered by the perforated sheet.

Results of calculations are shown in Figs. I.3-I.5. The real part of dynamic density,  $\text{Re}(\tilde{\rho})$ , is practically constant in the considered frequency band and fixed pressure (see Fig. I.3). The rarefaction effect leads to essential decrease of  $\text{Re}(\tilde{\rho})$  at  $p_0 = 1.013$  kPa. For the ambient pressure 10.13 kPa, this effect is negligible. Figure I.4 shows that the imaginary part of dynamic density,  $\text{Im}(\tilde{\rho})$ , is more sensitive to pressure variations than its real part. This sensitivity increases as the disturbance frequency decreases. For sound of low frequency ( $f \approx 1$  kHz), the rarefaction effect leads to approximately two times increase of  $\text{Im}(\tilde{\rho})$  at  $p_0 = 1.013$  kPa.

The real part of dynamic compressibility is practically constant,  $\text{Re}\{C(\omega)\gamma p_0\} \approx 1.4$ , in the considered ranges of pressure and frequency. Figure I.5 shows that the imaginary part,  $\text{Im}\{C(\omega)\gamma p_0\}$ , is approximately a linear function of frequency. The slope of this function essentially depends on the ambient pressure and Knudsen number. However, the module of  $\text{Im}\{C(\omega)\gamma p_0\}$  is much smaller than  $\text{Re}\{C(\omega)\gamma p_0\}$  and can be neglected in predictions of acoustic properties of the perforated panel.

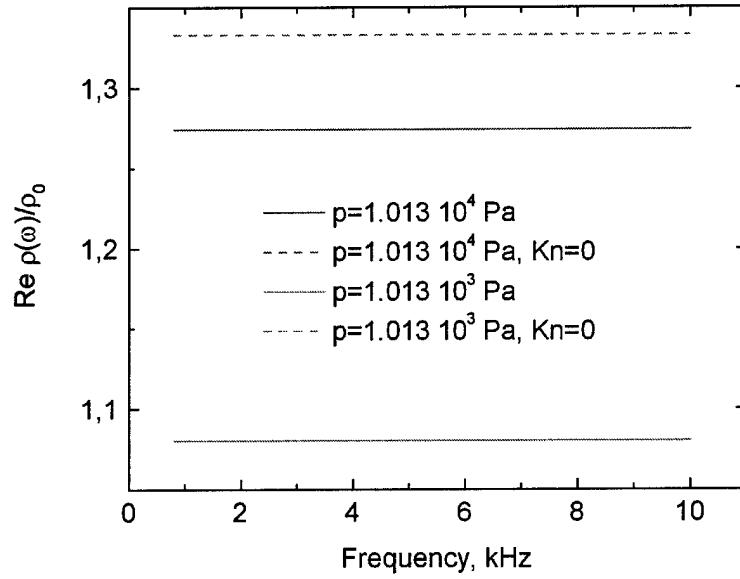


**Fig. I.3.** Theoretical dependence of the real part of dimensionless dynamic density for the cylindrical pore of radius  $30\mu\text{m}$  versus pressure and frequency (red solid and red dashed lines coincide).

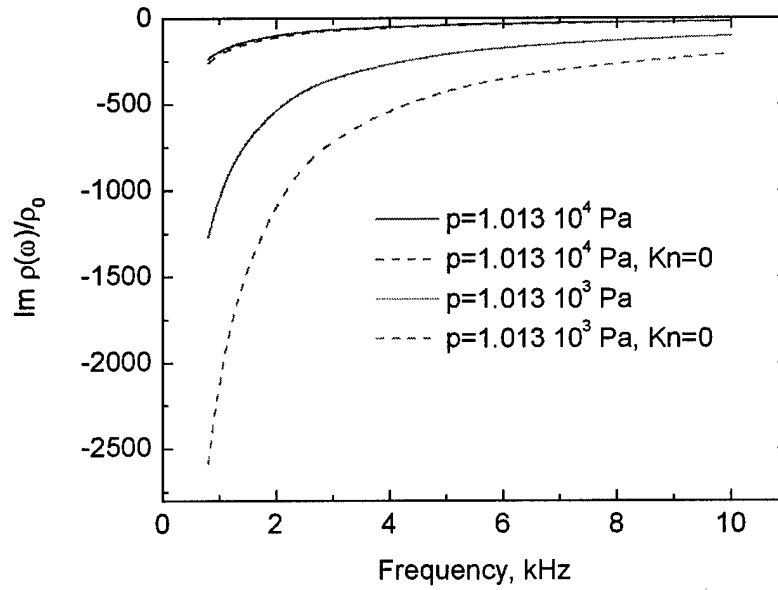


**Fig. I.4.** Theoretical dependence of the imaginary part of the dimensionless dynamic density for the cylinder pore of radius  $30\mu\text{m}$  versus pressure and frequency.



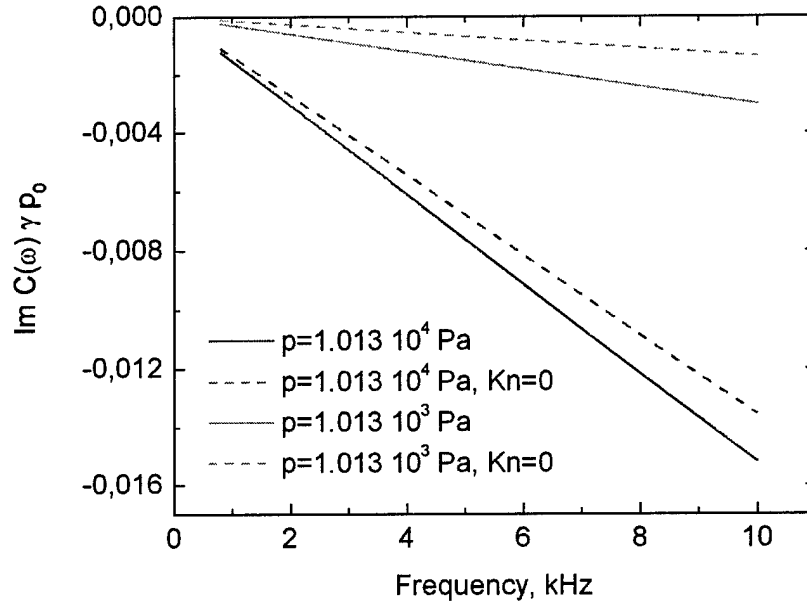


**Fig. 1.5.** Theoretical dependence of the imaginary part of the dimensionless dynamic compressibility for the cylinder pore of radius 30μm versus pressure and frequency.

### 1.2.5. Admittance of porous layer

As shown by Fedorov & Malmuth (2001) and Fedorov et al. (2003a,b), the admittances  $A_x$ ,  $A_z$  and  $A_y$  produce small effects on the boundary-layer instability, compared to the effect of  $A_y$ . This allows us to approximate the wall boundary conditions (1.11) as

$$F_1(0) = 0, \quad F_7(0) = 0, \quad F_5(0) = 0, \quad (1.46)$$

$$F_3(0) = A_y F_4(0).$$

The admittance component  $A_y$  is expressed in the form (Fedorov & Malmuth, 2001)

$$A_y = \frac{\phi}{Z_0} \tanh(mh), \quad (1.47)$$

where  $\phi$  is porosity,  $h = h^* / l^*$  is the porous-layer thickness,  $Z_0$  and  $m$  are the characteristic impedance and propagation constant of a porous medium, respectively. The two latter are functions of the complex dynamic density  $\tilde{\rho}$  and the complex dynamic compressibility  $\tilde{C}$ . Using the scaling of stability problem formulated in Section 1.1, we obtain

$$Z_0 = -\frac{\sqrt{\tilde{\rho} / \tilde{C}}}{M_e \sqrt{T_w}}, \quad m = \frac{i\omega M_e}{\sqrt{T_w}} \sqrt{\tilde{\rho} \tilde{C}}, \quad (1.48)$$

where the dimensionless complex dynamic density  $\hat{\rho}$  and dynamic compressibility  $\hat{C}$  are expressed in the form

$$\hat{\rho} = \frac{1}{1 - F(B_v, \varsigma)}, \quad (1.49)$$

$$\hat{C} = 1 + (\gamma - 1)F(B_E, \varsigma\sqrt{\text{Pr}}), \quad (1.50)$$

$$F(B_v, \varsigma) = \frac{Q(\varsigma)}{1 - 0.5B_v\varsigma^2Q(\varsigma)}, \quad (1.51)$$

$$F(B_E, \varsigma\sqrt{\text{Pr}}) = \frac{Q(\varsigma\sqrt{\text{Pr}})}{1 - 0.5B_E(\varsigma\sqrt{\text{Pr}})^2Q(\varsigma\sqrt{\text{Pr}})}, \quad (1.52)$$

$$\varsigma = \sqrt{i\omega\rho_0 r_0^2 / \mu}.$$

Note that in the boundary-layer stability problem the time factor is  $\exp(-i\omega t)$ . For this reason, the argument  $\varsigma = \sqrt{i\omega\rho_0 r_0^2 / \mu}$ , which is used in stability analyses, is different from the argument  $\Lambda = \sqrt{-i\omega\rho_0 r_0^2 / \mu}$  in the relations (1.43)-(1.45) derived for disturbances  $\sim \exp(i\omega t)$ . The formulas (1.49)-(1.52) coincide with those of Fedorov & Malmuth (2001) used for the modeling of  $A_y$  at  $\text{Kn} = 0$ .

### 1.3. Parametric studies of the UAC effect on the second mode

In this section, we discuss parametric studies of the UAC effect on the second-mode instability for the T-326 wind tunnel conditions. These studies are performed in the framework of local-parallel linear stability theory; i.e., the growth rate (1.30) is calculated at  $\varepsilon = 0$ . The nonparallel effects will be included in Chapter III for comparison of stability calculations with the wind-tunnel data.

#### 1.3.1. Basic parameters and mean flow

Calculations are performed for a  $7^\circ$  half-angle sharp cone at the freestream Mach number  $M_\infty \approx 6$ . Flow parameters at the upper boundary layer edge are:

1. Mach number  $M_e = 5.3$
2. Temperature  $T_e^* = 56.4$  K
3. Stagnation temperature calculated at the specific heat ratio  $\gamma = 1.4$   
 $T_0^* = (1 + (\gamma - 1)M_e^2 / 2)T_e^* = 373.255$  K

4. Unit Reynolds number  $Re_1 = U_e / \nu_e$  is varied in the range  $Re_1 = (8.5 - 47.8) \times 10^6 \text{ m}^{-1}$

The cone length is  $L = 0.5 \text{ m}$ . Its surface is thermally insulated:  $T_w^* = T_{ad}^*$ .

The porous coating characteristics correspond to the experiments in T-326 wind tunnel:

1. Average pore radius  $r^* = 25 \text{ } \mu\text{m}$
2. Coating thickness  $h^*$  is variable
3. Average pore spacing  $s^* = 100 \text{ } \mu\text{m}$
4. Porosity  $\phi \approx 0.2$

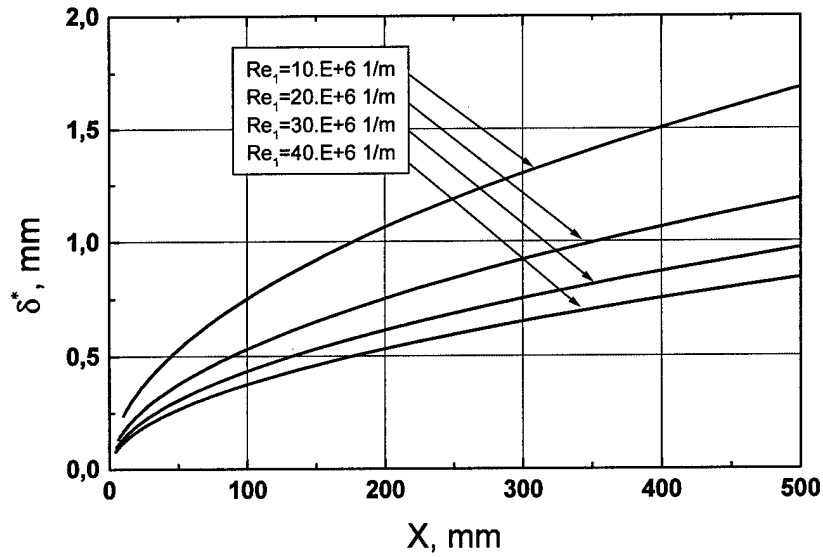


**Fig. I.6.** Boundary-layer displacement thickness at various unit Reynolds numbers  $Re_1$ ; adiabatic cone, local Mach number  $M_e = 5.3$ , local temperature at the upper boundary-layer edge  $T_e = 56.4 \text{ K}$ .

The eigenvalue problem (1.14)-(1.16) is solved at Prandtl number  $Pr = 0.708$  and specific heat ratio  $\gamma = 1.4$ . The dynamic viscosity is calculated using the Sutherland formula; the second viscosity is  $\mu_2^* = 0.8\mu^*$ .

Figure I.6 shows the boundary-layer displacement thickness  $\delta^*(x^*)$ . The nondimensional mean-flow profiles  $U(y)$  and  $T(y)$ ,  $y = y^* / \delta^*$ , are shown in Figs. I.7 and I.8, respectively. The boundary-layer thickness,  $\delta \approx 1.3\delta^*$ , is marked by arrow. The adiabatic wall temperature is  $T_{ad} = 5.707T_e$ .

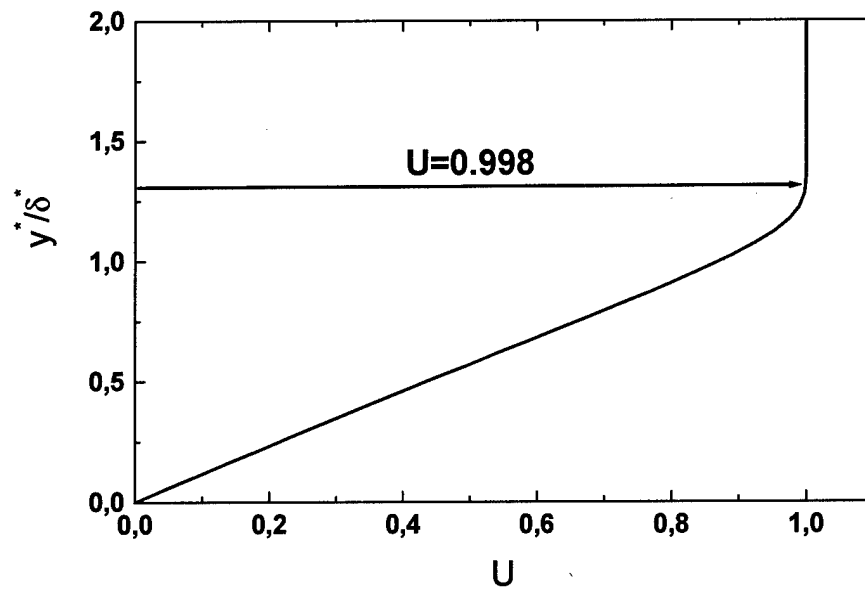


**Fig. I.7.** Mean-flow velocity profile; adiabatic cone, local Mach number  $M_e = 5.3$ , temperature at the upper boundary-layer edge  $T_e = 56.4$  K.

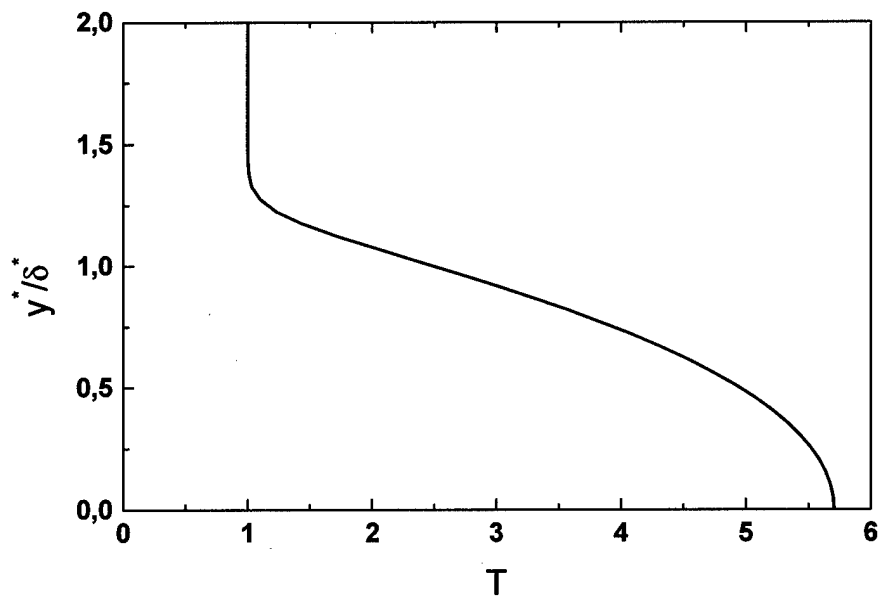


**Fig. I.8.** Mean temperature profile; adiabatic cone, local Mach number  $M_e = 5.3$ , temperature at the upper boundary-layer edge  $T_e = 56.4$  K.

### 1.3.2. Stability characteristics for adiabatic wall

We consider characteristics of the second mode. Since most unstable second-mode waves are two-dimensional, all calculations are performed for  $\beta = 0$ . Results are presented for the unit Reynolds numbers  $Re_1 \equiv \rho_e^* U_e^* / \mu_e^* = (10, 20, 30, 40) \times 10^6 \text{ m}^{-1}$  relevant to the experimental conditions.

#### Disturbances of maximum growth rate

Figures I.9 and I.10 show the disturbance wavelength  $\lambda = 2\pi / \text{Re}(\alpha)$  and the nondimensional frequency parameter  $F = \omega \nu_e / U_e^2$  for the second-mode waves of maximum growth rates. These characteristics are weakly sensitive to the porous coating; i.e., the disturbance wavelength and frequency on the porous and solid walls are almost equal. The ratio  $\lambda^* / \delta \approx 2$  is typical for the second-mode instability.

Figures I.11-I.14 show the maximum growth rates on solid and porous surfaces. The stabilization effect increases with the longitudinal coordinate  $X$ . Maximum stabilization is observed at  $Re_1 = 40 \times 10^{-6} \text{ m}^{-1}$  (see Fig. I.14) that corresponds to maximum of the ratio  $r^* / \delta^*$ .

Figures I.15-I.16 show disturbance characteristics for the porous-coating thickness  $h^* = 2r^*, 4r^*, 6r^*, 8r^*, 10r^*, \infty$  at the unit Reynolds number  $Re_1 = 10 \times 10^6 \text{ m}^{-1}$ . For  $h^* \geq 6r^*$ , the reflection from the pore bottom is small; i.e., the porous coating can be treated as infinitely thick. Similar trends are observed in the cases of  $Re_1 = (20 - 40) \times 10^6 \text{ m}^{-1}$ .

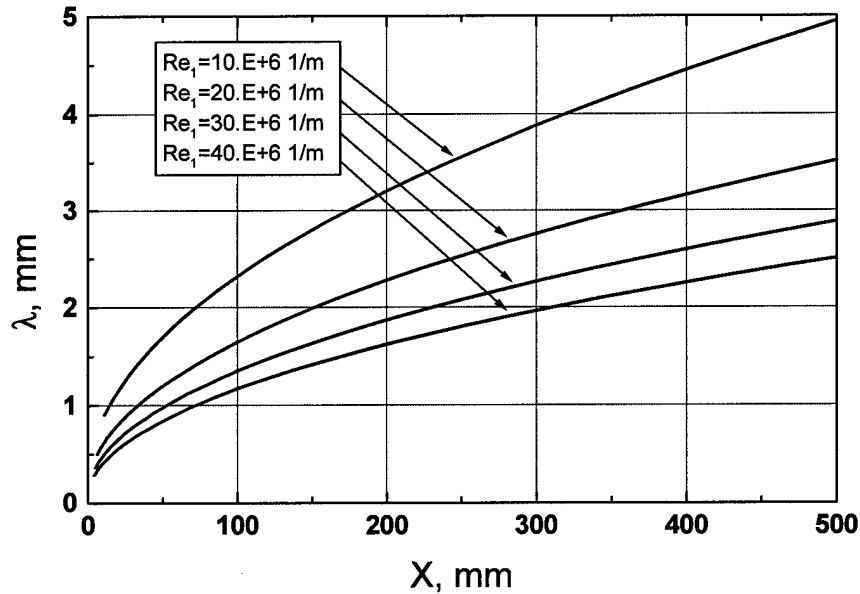


**Fig. I.9.** Wavelength of the most unstable second mode at various unit Reynolds numbers  $Re_1$ ;  $T_w = T_{ad}$ ,  $M_e = 5.3$ ,  $T_e = 56.4 \text{ K}$ .

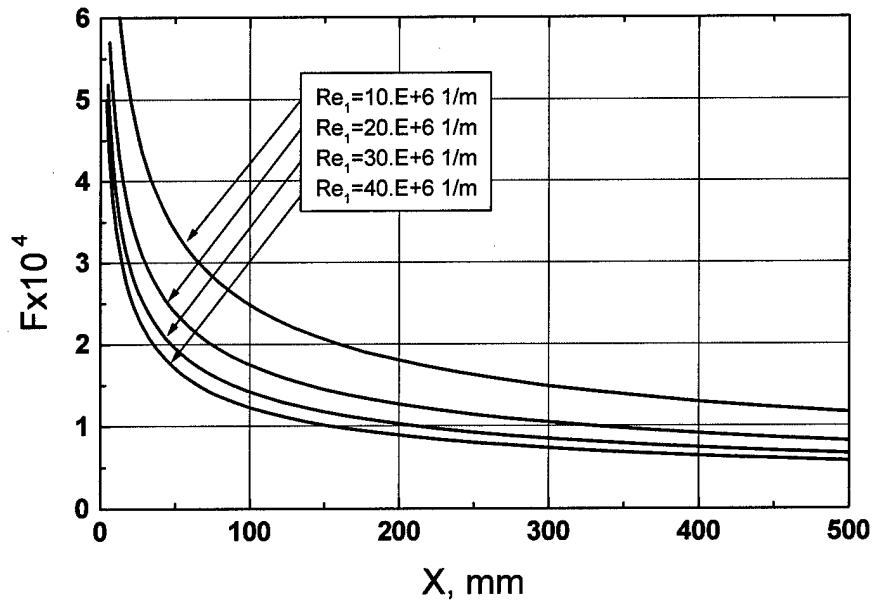


**Fig. I.10.** Frequency parameter of the most unstable second mode at various unit Reynolds numbers  $Re_1$ ;  $T_w = T_{ad}$ ,  $M_e = 5.3$ ,  $T_e = 56.4 \text{ K}$ .

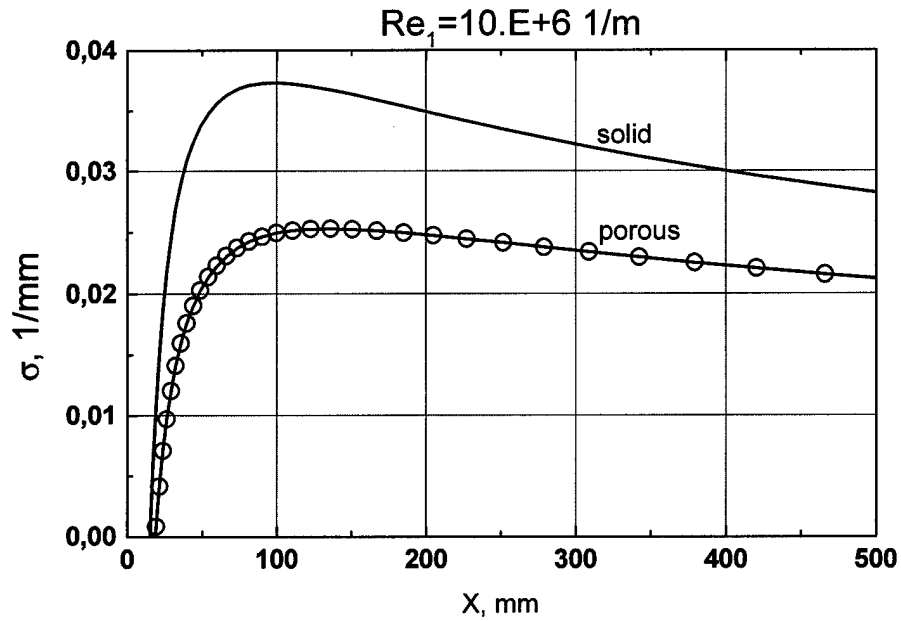


**Fig. I.11.** Spatial growth rate of most unstable disturbance on solid and porous surfaces;  $Re_1 = 10^7 \text{ m}^{-1}$ ,  $T_w = T_{ad}$ ,  $M_e = 5.3$ ,  $T_e = 56.4 \text{ K}$ .

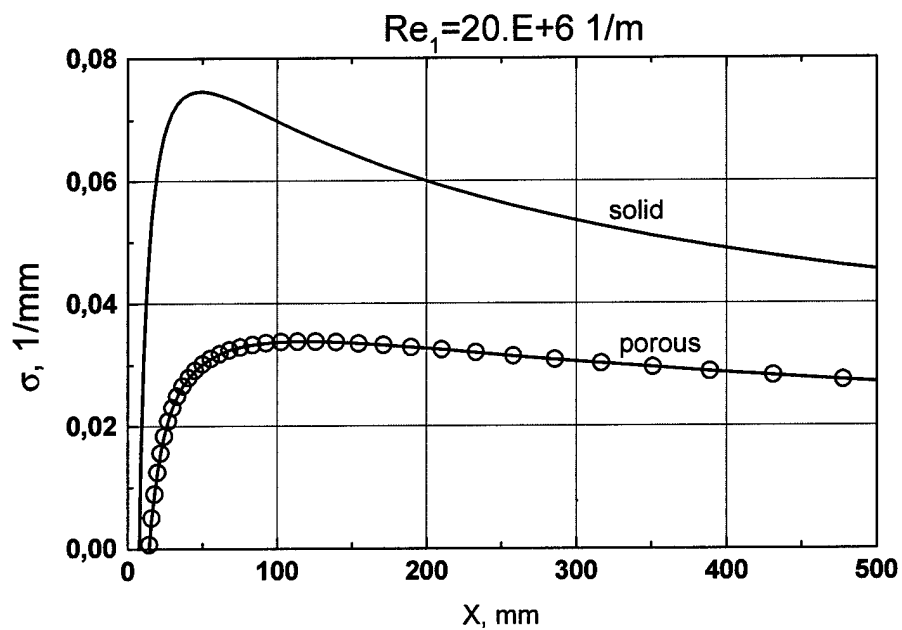


**Fig. I.12.** Spatial growth rate of the most unstable disturbance on solid and porous surfaces;  
 $Re_1 = 2 \times 10^7 \text{ m}^{-1}$ ,  $T_w = T_{ad}$ ,  $M_e = 5.3$ ,  $T_e = 56.4 \text{ K}$ .

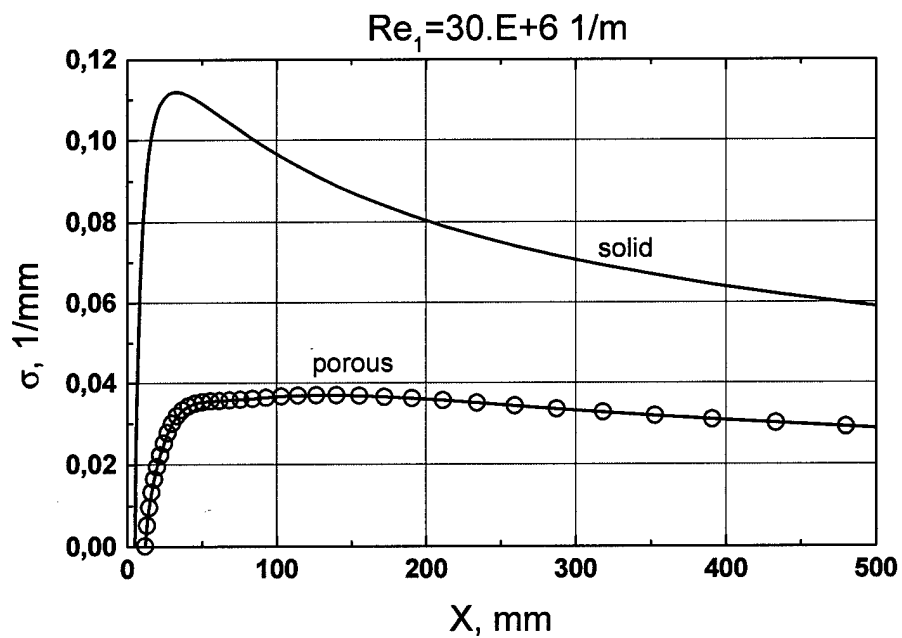


**Fig. I.13.** Spatial growth rate of the most unstable disturbance on solid and porous surfaces;  
 $Re_1 = 3 \times 10^7 \text{ m}^{-1}$ ,  $T_w = T_{ad}$ ,  $M_e = 5.3$ ,  $T_e = 56.4 \text{ K}$ .

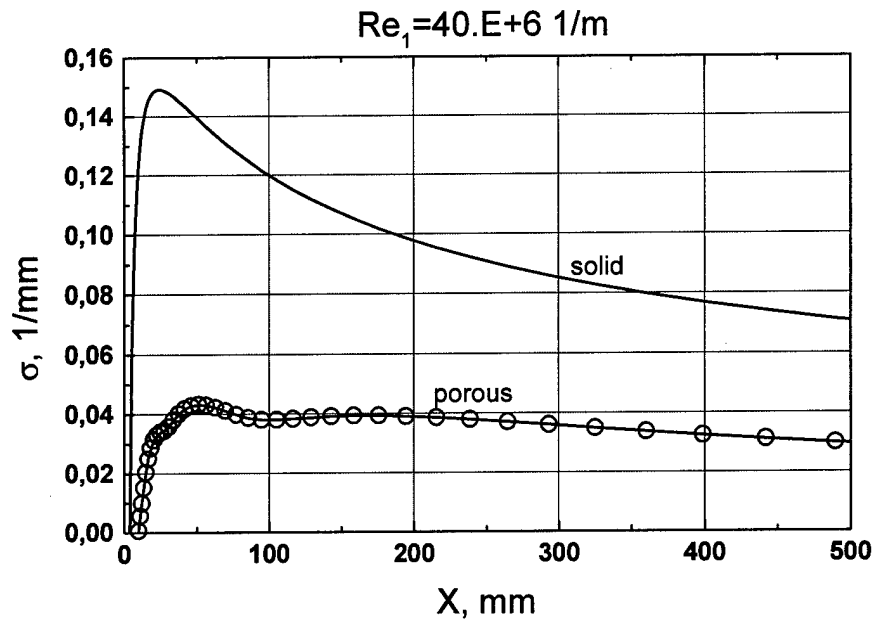


**Fig. I.14.** Spatial growth rate of the most unstable disturbance on solid and porous surfaces;  $Re_1 = 4 \times 10^7 \text{ m}^{-1}$ ,  $T_w = T_{ad}$ ,  $M_e = 5.3$ ,  $T_e = 56.4 \text{ K}$ .

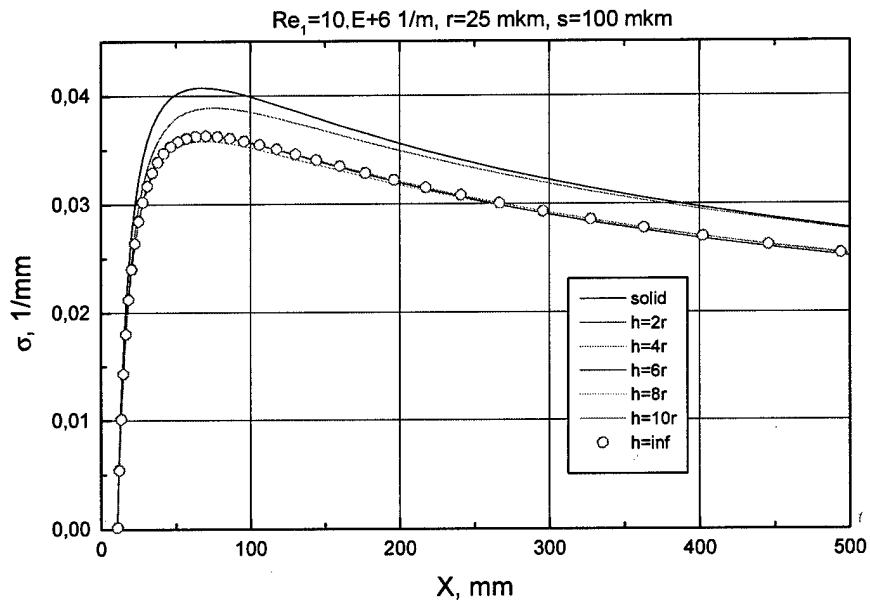


**Fig. I.15.** Maximal growth rate for UAC of various thickness;  $Re_1 = 10^7 \text{ m}^{-1}$ ,  $T_w = T_{ad}$ ,  $M_e = 5.3$ ,  $T_e = 56.4 \text{ K}$ .



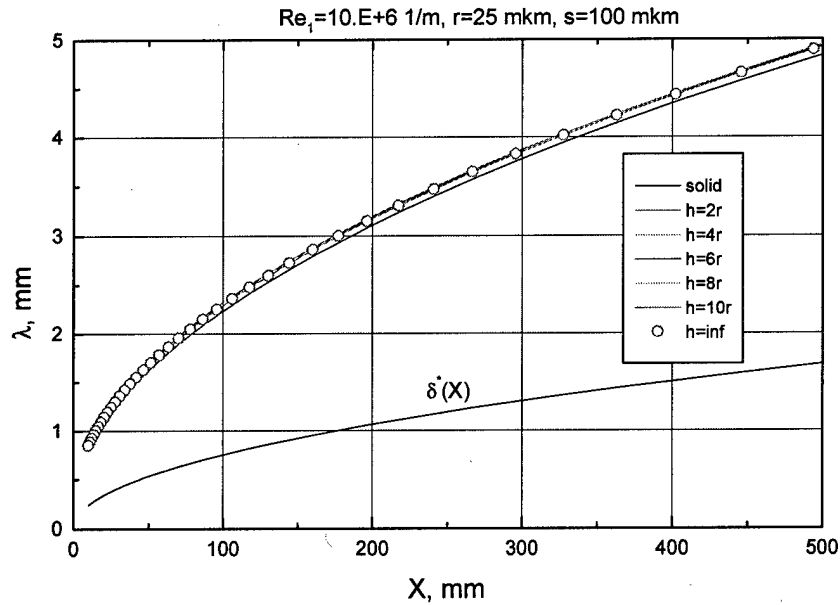


**Fig. I.16.** Wavelength of most unstable waves for UAC of various thickness;  $Re_1 = 10^7 \text{ m}^{-1}$ ,  $T_w = T_{ad}$ ,  $Me = 5.3$ ,  $T_e = 56.4 \text{ K}$ .

#### Disturbances of various frequencies

Figures I.17 and I.18 show the growth rate as a function of  $X$  for various frequency parameters  $F = \omega^* \nu_e^* / U_e^{*2}$ . The disturbance of fixed frequency is stabilized by the porous coating at large  $X$ , while it is destabilized at small  $X$ . The net effect is small or even negative for relatively small  $F$ . This behavior is typical for the boundary layer on adiabatic wall. Note that aerodynamic surfaces of actual hypersonic vehicles correspond to small wall-temperature ratios:  $T_w / T_{ad} < 0.3$ . In this case the UAC performance is much higher as will be shown in the next section.

#### 1.3.3. Stability characteristics for cold wall

**The surface temperature**  $T_w = 3T_e \approx 169 \text{ K}$

Figures I.19 and I.21 show the maximum growth rate as a function of the longitudinal coordinate  $X$  for the solid wall (black line) and the porous wall (red line); unit Reynolds number is  $Re_1 = 10^7$  and  $2 \times 10^7 \text{ m}^{-1}$ , respectively. Figures I.20 and I.22 show the growth rate as a function of  $X$  for various frequency parameters  $F$  and the same mean-flow parameters. In this case, the net stabilization effect is positive.

**The surface temperature**  $T_w = 2T_e \approx 113 \text{ K}$

Figures I.23 and I.25 show the maximum growth rate as a function of the longitudinal coordinate  $X$  for the solid wall (black line) and the porous wall (red line); unit Reynolds number

$Re_1 = 10^7$  and  $2 \times 10^7 \text{ m}^{-1}$ , respectively. Figures I.24 and I.26 show the growth rate as a function of  $X$  for various frequency parameters  $F$ . In this case, the net stabilization effect is strong.

These calculations indicate that the UAC performance dramatically increases as the wall temperature decreases. This trend is favorable for practice because surfaces of actual hypersonic vehicle have wall temperatures essentially lower than the adiabatic temperature.

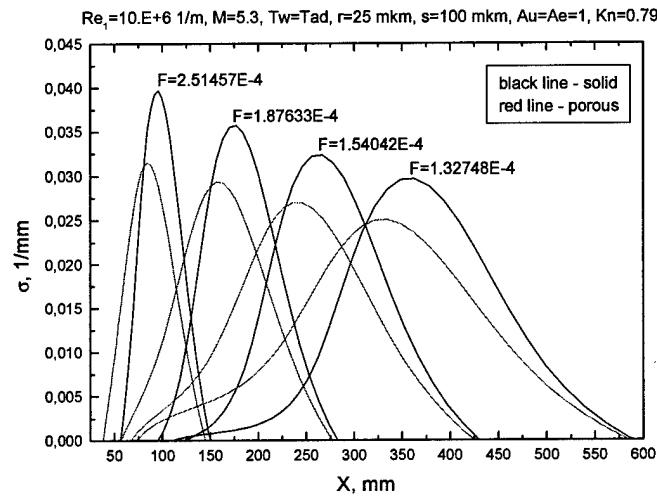


**Fig. I.17.** Second-mode growth rate distributions at various frequencies;  $Re_1 = 10^7 \text{ m}^{-1}$ ,  $T_w = T_{ad}$ ,  $M_e = 5.3$ ,  $T_e = 56.4 \text{ K}$ .

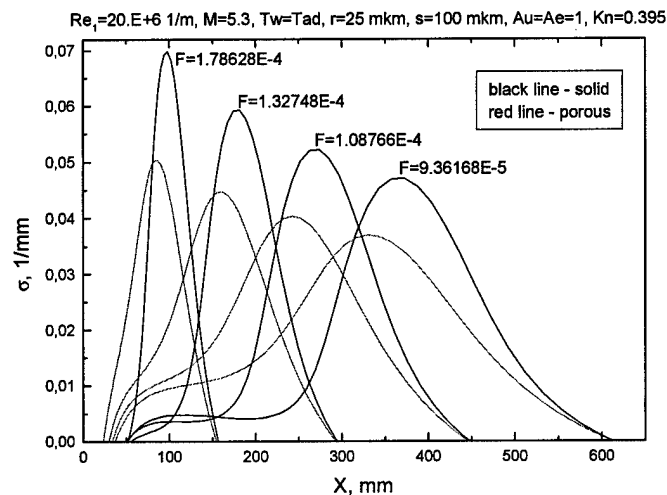


**Fig. I.18.** Second-mode growth rate distributions at various frequencies;  $Re_1 = 2 \times 10^7 \text{ m}^{-1}$ ,  $T_w = T_{ad}$ ,  $M_e = 5.3$ ,  $T_e = 56.4 \text{ K}$ .

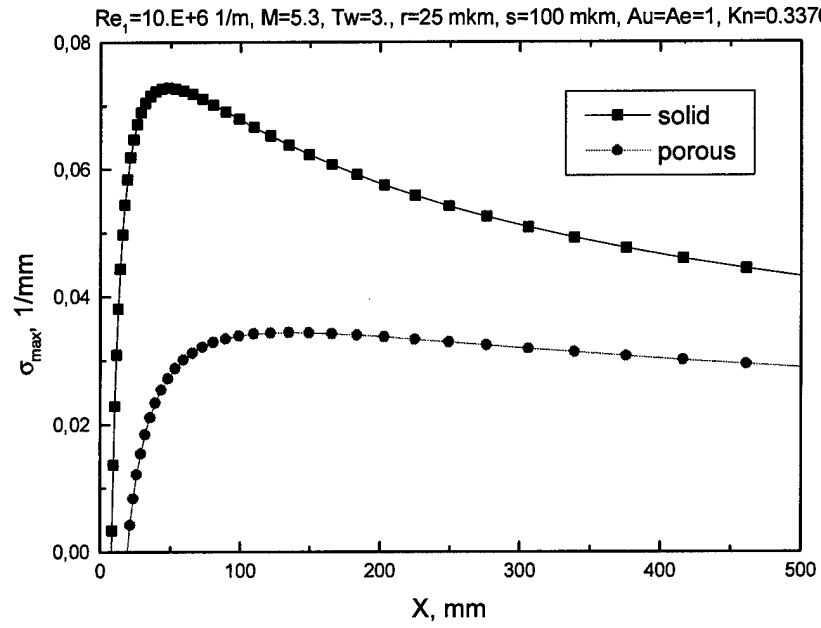


**Fig. I.19.** Maximum growth rate of the second mode;  $T_w = 3T_e$ ,  $Re_1 = 10^7 \text{ m}^{-1}$ ,  $M_e = 5.3$ ,  $T_e = 56.4 \text{ K}$ .

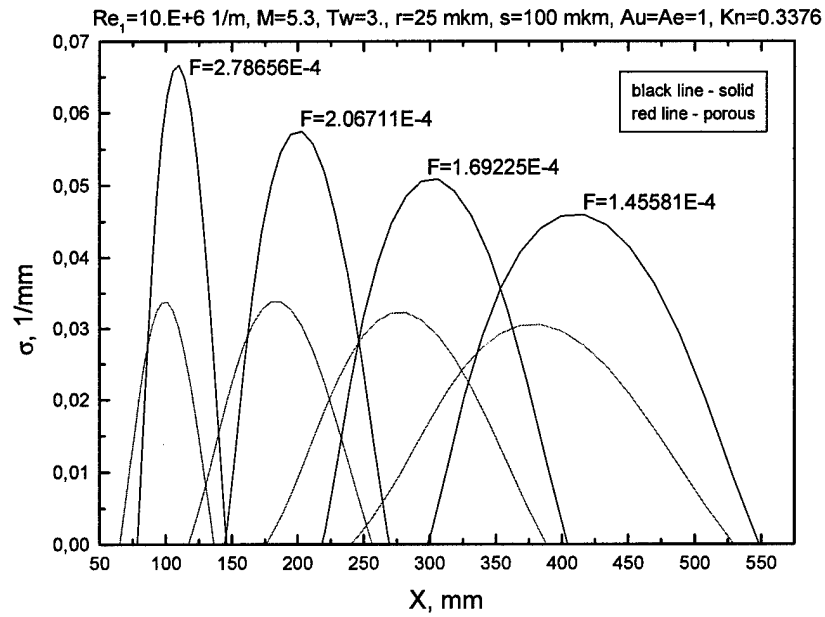


**Fig. I.20.** Second-mode growth rates for various frequencies;  $T_w = 3T_e$ ,  $Re_1 = 10^7 \text{ m}^{-1}$ ,  $M_e = 5.3$ ,  $T_e = 56.4 \text{ K}$ .

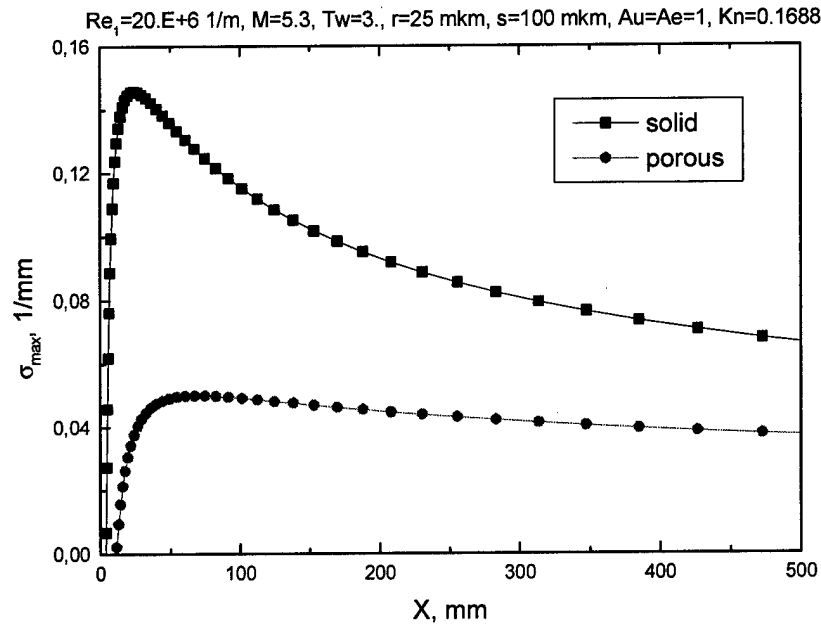


**Fig. I.21.** Maximum growth rate of the second mode;  $T_w = 3T_e$ ,  $Re_1 = 2 \times 10^7 \text{ m}^{-1}$ ,  $M_e = 5.3$ ,  $T_e = 56.4 \text{ K}$ .

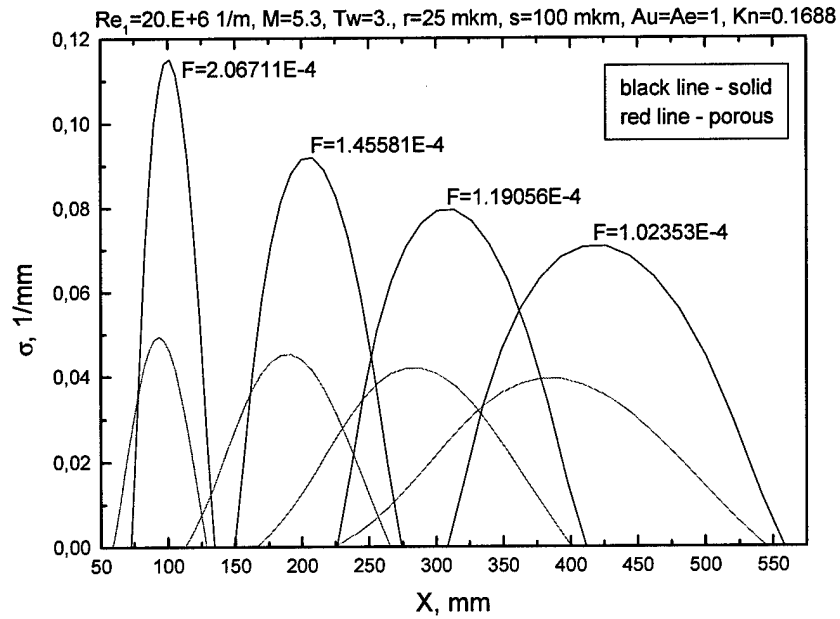


**Fig. I.22.** Second-mode growth rates for various frequencies;  $T_w = 3T_e$ ,  $Re_1 = 2 \times 10^7 \text{ m}^{-1}$ ,  $M_e = 5.3$ ,  $T_e = 56.4 \text{ K}$ .

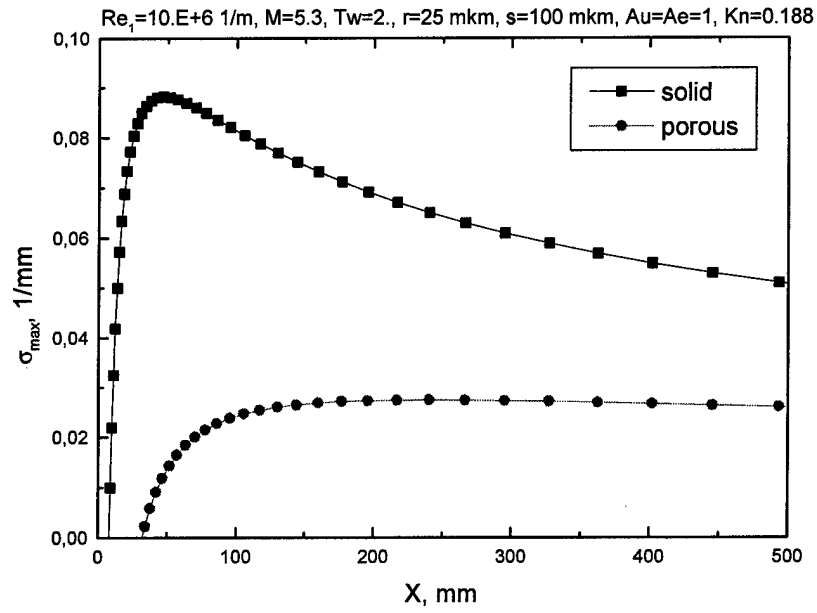


**Fig. I.23.** Maximum growth rate of the second mode;  $T_w = 2T_e$ ,  $Re_1 = 10^7 \text{ m}^{-1}$ ,  $M_e = 5.3$ ,  $T_e = 56.4 \text{ K}$ .

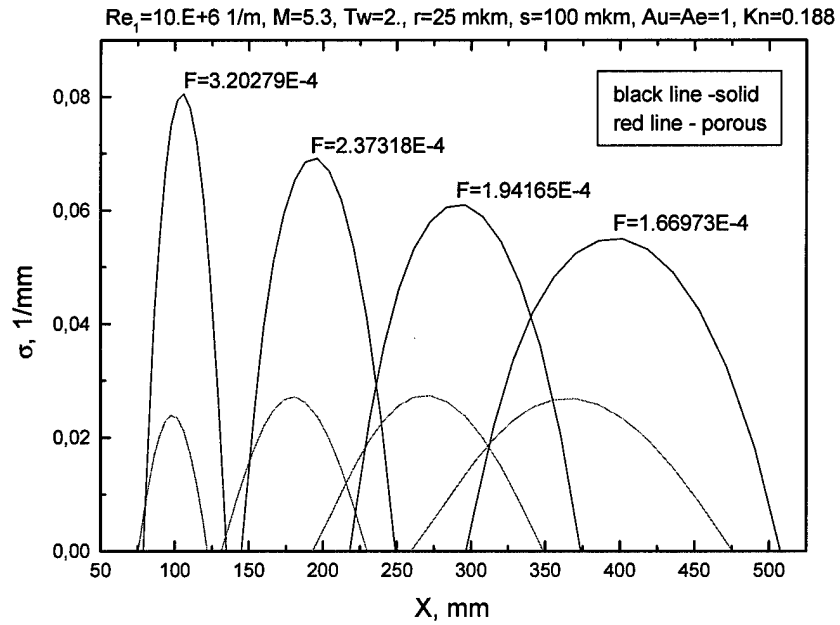


**Fig. I.24.** Second-mode growth rates for various frequencies;  $T_w = 2T_e$ ,  $Re_1 = 10^7 \text{ m}^{-1}$ ,  $M_e = 5.3$ ,  $T_e = 56.4 \text{ K}$ .

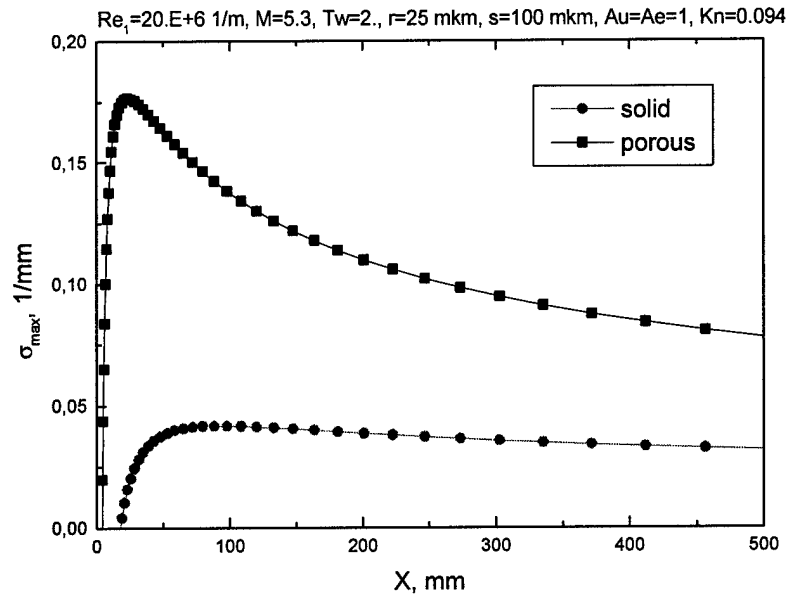


**Fig. I.25.** Maximum growth rate of the second mode;  $T_w = 2T_e$ ,  $Re_1 = 2 \times 10^7 m^{-1}$ ,  $M_e = 5.3$ ,  $T_e = 56.4$  K.

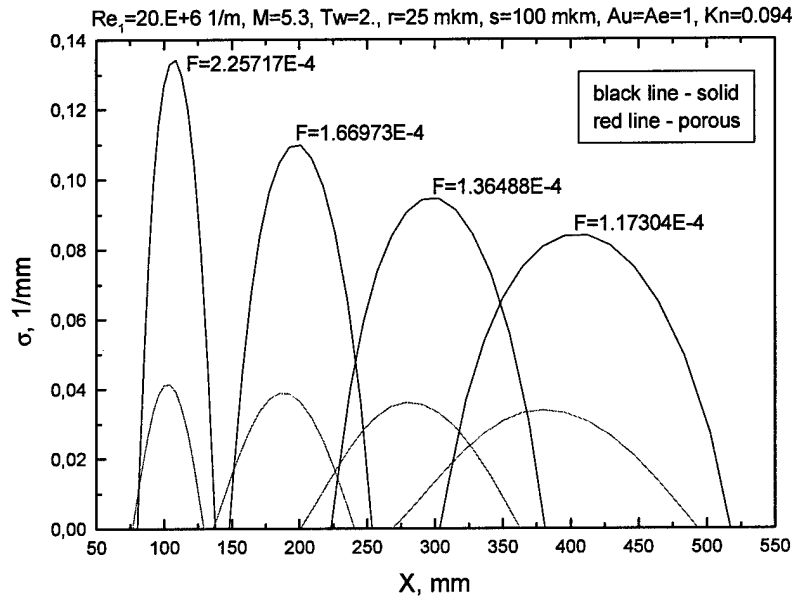


**Fig. I.26.** Second-mode growth rates for various frequencies;  $T_w = 2T_e$ ,  $Re_1 = 2 \times 10^7 m^{-1}$ ,  $M_e = 5.3$ ,  $T_e = 56.4$  K.

### 1.3.4. Rarefaction effect

Because of relatively small mean-flow densities the rarefaction effects inside pores may be important. Hereafter, the Knudsen number is determined as

$$\text{Kn} = \frac{\mu_w^* \sqrt{2\pi R_g T_w^*}}{r^* P_w^*}, \quad (1.53)$$

where  $R_g = 287 \text{ J/(kg K)}$  is gas constant. The Knudsen number can be also expressed in terms of basic nondimensional parameters as

$$\text{Kn} = \frac{\mu_w M_e}{r R} \sqrt{2\pi\gamma T_w}. \quad (1.54)$$

Figure I.27 shows the disturbance growth rate as a function of the coating thickness  $h$  with and without the Knudsen layer. Calculations were performed for the disturbance of fixed frequency  $F = 1.43 \times 10^{-4}$  at the Reynolds number  $R = 13262$ . The rarefaction effect makes pores to be more transparent with respect to disturbances. This leads to stronger stabilization of the second mode.

The maximum growth rates for the adiabatic wall covered by the UAC of  $r^* = 25 \mu\text{m}$ ,  $s^* = 100 \mu\text{m}$  and various  $h^*$  are shown in Fig. I.28 for  $\text{Re}_1 = 10^7 \text{ m}^{-1}$ . The disturbance reflection from the pore bottom becomes negligible for  $h^* > 10r^*$ . Similar trends were obtained for the unit Reynolds numbers  $\text{Re}_1 = (2 - 3) \times 10^7 \text{ m}^{-1}$ .

Data shown in Figs. I.29-I.31 were calculated for infinitely deep holes in adiabatic wall. It is seen that the Knudsen layer on pore walls leads to additional stabilization of the second mode.

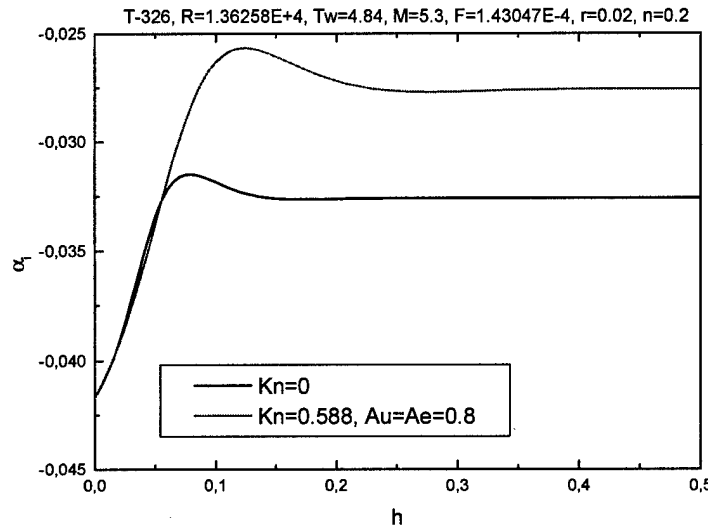


**Fig. I.27.** Second-mode growth rate as a function of the UAC thickness with and without Knudsen layer;  $T_w = 4.84T_e$ ,  $R = 13262$ ,  $F = 1.43 \times 10^{-4}$ ,  $M_e = 5.3$ ,  $T_e = 56.4 \text{ K}$ .

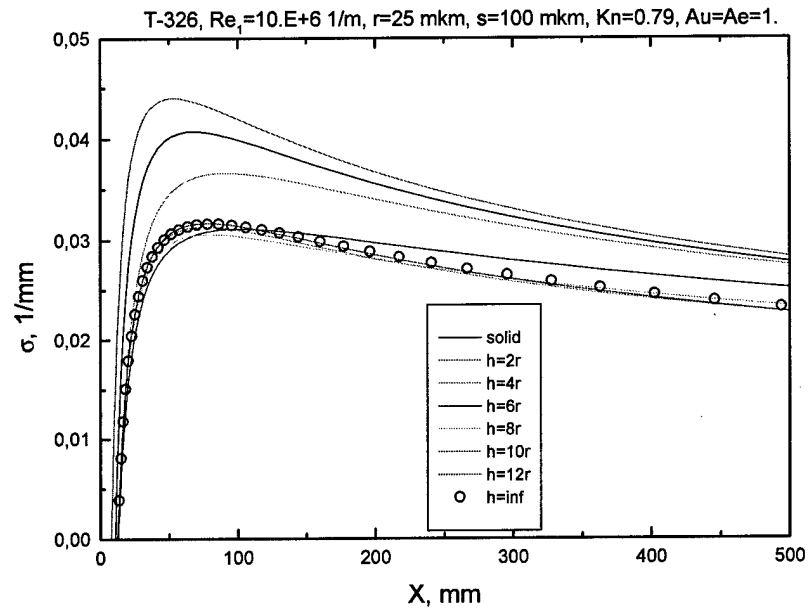


**Fig. I.28.** Maximum growth rate distributions for UAC of various thickness including the rarefaction effect;  $T_w = T_{ad}$ ,  $Re_1 = 10^7 \text{ m}^{-1}$ ,  $M_e = 5.3$ ,  $T_e = 56.4 \text{ K}$ ;  $Kn = 0.79$ .

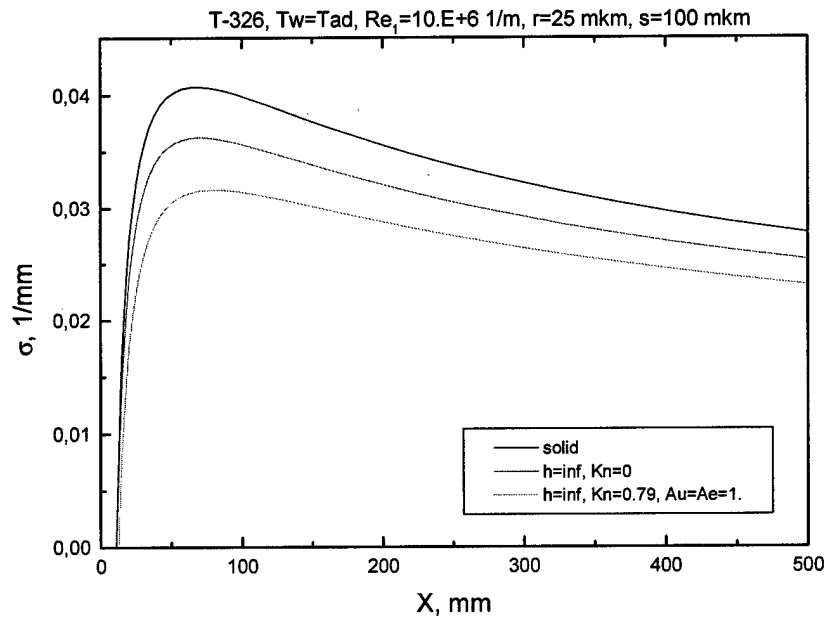


**Fig. I.29.** The rarefaction effect on maximum growth rates;  $T_w = T_{ad}$ ,  $Re_1 = 10^7 \text{ m}^{-1}$ ,  $M_e = 5.3$ ,  $T_e = 56.4 \text{ K}$ .



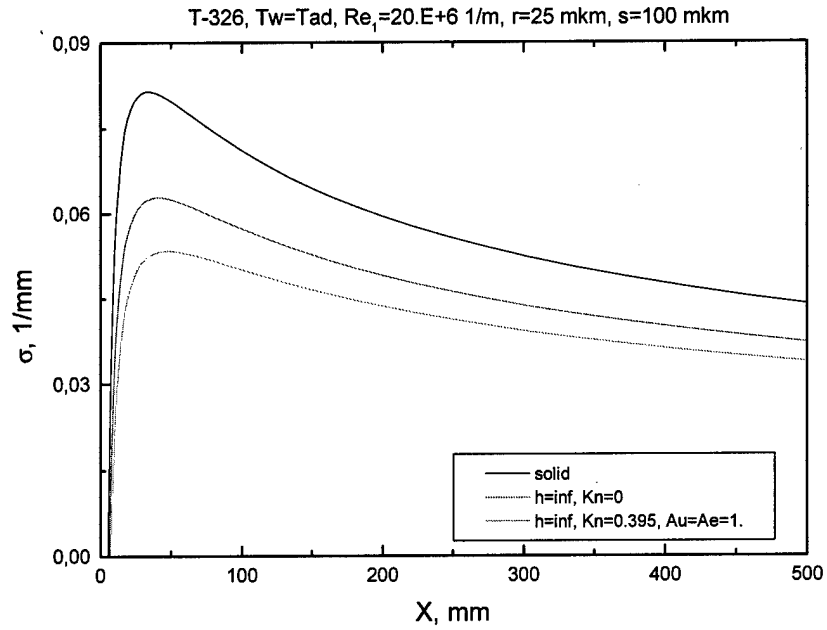


**Fig. I.30.** The rarefaction effect on maximum growth rates;  $T_w = T_{ad}$ ,  $Re_1 = 2 \times 10^7 m^{-1}$ ,  $M_e = 5.3$ ,  $T_e = 56.4 K$ .

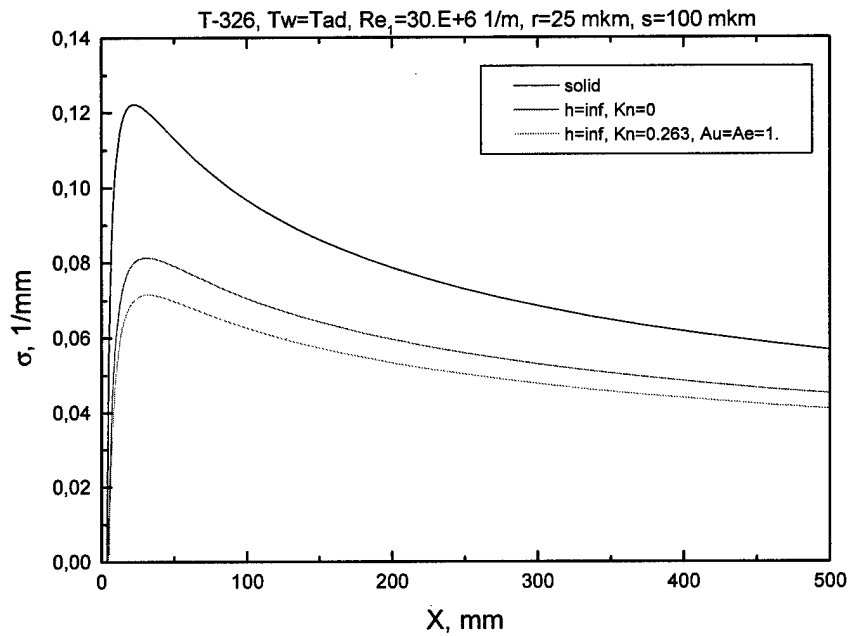


**Fig. I.31.** The rarefaction effect on maximum growth rates;  $T_w = T_{ad}$ ,  $Re_1 = 3 \times 10^7 m^{-1}$ ,  $M_e = 5.3$ ,  $T_e = 56.4 K$ .

## 1.4. Summary

Linear stability problem for three-dimensional disturbances in two-dimensional boundary layers on a porous wall was formulated in the framework of the asymptotic method of multiple scales. This problem differs from the typical stability problem because of new boundary conditions associated with absorption of disturbance energy by a porous coating. These boundary conditions are formulated in terms of the porous-wall acoustic admittances, which depend on the UAC microstructure.

Acoustic properties of a cylindrical pore were analyzed in the framework of linear acoustic theory. Dependencies of the dynamic density and dynamic compressibility on gas pressure and disturbance frequency were derived including the gas rarefaction effects. The analysis is focused on the most practical case when the molecular mean free path is smaller (or much smaller) than the pore radius. Calculations indicate that acoustic properties of the perforated panel essentially depend on Knudsen number in the considered ranges of pressure and frequency. The imaginary parts of dynamic density and dynamic compressibility are more sensitive to the pressure variation than their real parts.

Parametric calculations of the UAC effect on the second-mode stability are performed for the T-326 wind tunnel conditions including the gas rarefaction effect. In the case of adiabatic wall, the net stabilization effect is small or even negative for disturbances of relatively small frequencies. The UAC stabilization dramatically increases as the wall temperature ratio decreases. This trend is preferable for practice because surfaces of actual hypersonic vehicle are maintained at low wall-temperature ratios.

The rarefaction effect is appreciable for the T-326 conditions. The presence of the Knudsen layer on the pore wall leads to deeper penetration of disturbances into pores and provides stronger stabilization of the second mode.

The discussed above parametric studies were used for design the porous coating tested on a sharp cone in the T-326 wind tunnel (see Chapter III).

## Chapter II. Benchmark Measurements of UAC Characteristics

Design of ultrasonic absorptive coatings (UAC) for hypersonic boundary-layer stabilization requires sound-absorbing characteristics of porous materials. It is difficult to perform direct measurements of these characteristics in aerodynamic experiments due to low gas pressure ( $\approx 0.01$  bar) and high frequencies ( $f \approx 10^6$  Hz) of disturbances observed in hypersonic boundary layers. Under these conditions acoustic disturbances quickly attenuate via viscous dissipation of acoustic energy. The attenuation factor is proportional to  $f^2$  and inversely proportional to the gas density. For the frequency of 200 kHz and density corresponding to the pressure of 20-30 torr typical for free stream in a hypersonic wind tunnel, sound intensity drops  $e$ -times at the distance of few millimeters.

To overcome this difficulty it is suggested:

- Develop a theoretical model of acoustic absorption by a porous coating
- Perform benchmark measurements at low frequencies and verify the theoretical model
- Calculate the UAC characteristics for required ranges of frequencies and densities

This combined experimental and theoretical approach is accomplished in the present work.

### 2.1. Modeling of acoustic propagation in porous materials

The micrograph of the porous material is presented in Fig. II.1 (the large scale division is 0.1 mm). Microscopic measurements showed that holes have conical shape: the hole diameter is  $\approx 55$  micron from one side and  $\approx 40$  micron from the other side. The perforated sheet has the thickness  $h=0.5$  mm and the porosity  $\phi=0.3$ .

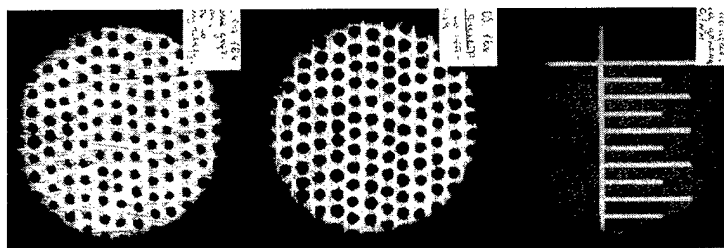


Fig. II.1 Micrograph of the perforated sheet (top view).

The porous material is modeled as a set of isolated cylindrical pores. Stinson & Champoux (1992) performed theoretical studies of acoustic disturbances propagating in cylindrical pores of arbitrary cross-section. The disturbance propagation depends on viscous effects in the tube and on heat conductivity. These effects can be modeled separately (Stinson & Champoux, 1992; Zwicker K., Kosten, 1952).

Propagation of acoustic disturbances in the cylindrical pore is characterized by the wave resistance  $W$  and the propagation constant  $\Gamma$ . These values can be expressed in terms of the complex dynamic density  $\rho(\omega)$  and the complex compressibility  $C(\omega)$  as

$$W = (\rho(\omega) / C(\omega))^{1/2} \quad (2.1)$$

$$\Gamma = i\omega(\rho(\omega)C(\omega))^{1/2}, \quad (2.2)$$

where  $C(\omega) = (1/\gamma P_0) \{ \gamma - (\gamma - 1) [\rho_0 / \rho(\text{Pr}\omega)] \}$ , which is valid for any cylindrical pore of constant cross-section;  $\rho_0$  is air density;  $\gamma$  is specific heat ratio; Pr is Prandtl number;  $\omega$  is angular frequency;  $P_0$  is air static pressure.

For a cylindrical pore of circular cross-section, the wave resistance  $W$  and the propagation constant  $\Gamma$  are shown in Figs. II.2 and II.3 as functions of the nondimensional parameter

$H = \frac{r_0}{\delta_a} = r_0 \left( \frac{\rho_0 \omega}{\eta} \right)^{1/2}$ , where  $r_0$  is pore radius;  $\delta_a$  is acoustic boundary-layer thickness;  $\eta$  is air dynamic viscosity. These dependencies were calculated using the relations given by Benade (1968): the complex density is expressed as

$$\rho(\omega) = \rho_0 [1 - 2T(\sqrt{-i}H) / \sqrt{-i}H]^{-1}, \quad (2.3)$$

where  $T(x) = J_1(x) / J_0(x)$ ;  $J_0$  and  $J_1$  - Bessel functions of zero and first order; the complex compressibility is

$$C(\omega) = (1/\rho_0 c^2) \left\{ 1 + (\gamma - 1) \left[ 2T(\sqrt{-i}\text{Pr}H) / \sqrt{-i}\text{Pr}H \right] \right\}. \quad (2.4)$$

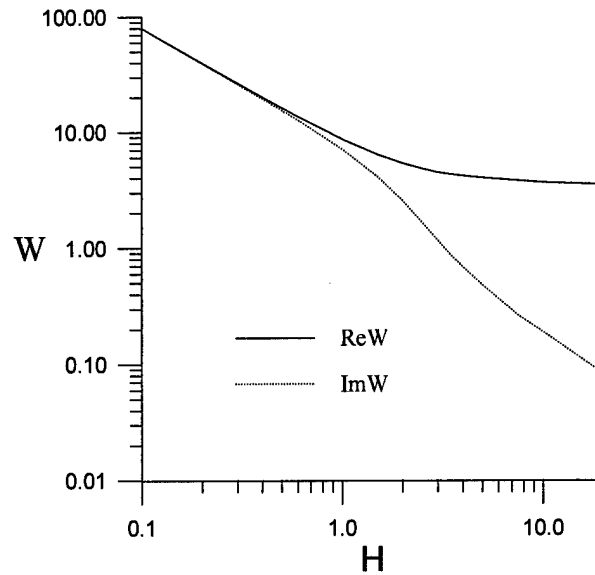


Fig. II.2 The wave resistance of cylindrical pore of circular cross-section.

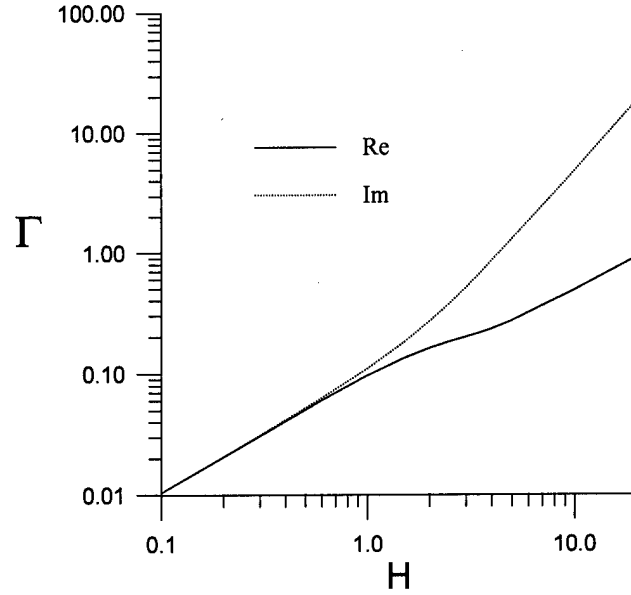


Fig. II.3 The propagation constant of cylindrical pore of circular cross section.

Consider a porous coating of the porosity  $\phi$ . The ratio of the pore length to the coating thickness is  $q$ ; the pore tortuosity is defined as  $q^2$ . The complex density of the porous material is introduced by the relation

$$i\omega\rho_b(\omega)v_b = -\frac{dp}{dz}, \quad (2.5)$$

where  $v_b$  is the mean velocity of the flow through the total cross section of the coating;  $\rho_b(\omega) = (q^2/\phi)\rho(\omega)$ . The coating compressibility is determined as  $C_b(\omega) = (\delta_b/\rho_0)/p$ , where  $\delta_b$  is acoustic pressure pulsations, averaged over the total cross section of the coating;  $C_b(\omega) = \phi C(\omega)$ . Then the wave resistance and the propagation constant are expressed in the form similar to the case of a single cylindrical pore

$$W = (\rho_b(\omega)/C_b(\omega))^{1/2}, \quad (2.6)$$

$$\Gamma = i\omega(\rho_b(\omega)C_b(\omega))^{1/2}. \quad (2.7)$$

For porous materials of complex microstructure, details of the pore shape are not available. Acoustic characteristics of these materials are determined with the assumption that actual pore structures may be simulated using cylindrical pores of effective size. For this purpose, the following non-acoustic characteristics of the porous material are used: porosity, tortuosity, and air resistance to the constant stream. These parameters can be determined regardless of acoustic measurements. In addition, so-called shape factor is introduced as a scale parameter multiplier to describe the material via cylindrical pores. In this framework, asymptotic approximations for

various frequency bands (namely, low-frequency band for small  $H$  and high-frequency band for large  $H$ ) are normally used.

For low frequencies, the complex density and compressibility are approximated as

$$\rho(\omega) = \sigma / i\omega + k_1 \rho_0 + \dots, \quad (2.8)$$

$$C(\omega) = (1/\gamma P_0) \{ \gamma - (\gamma - 1) [i\omega \rho_0 \text{Pr} / \sigma] \}, \quad (2.9)$$

where  $k_1$  is the structural coefficient independent on frequency (it is determined experimentally). According to Rzhevkin (1960), this coefficient is called as 'added mass coefficient'.

For high frequencies, viscous effects are appreciable in a thin layer on the pore wall (acoustic boundary layer). In this case, the complex density and compressibility are

$$\rho(\omega) \approx \rho_0 \left[ 1 + (2/r_0) (\eta / i\omega \rho_0)^{1/2} \right], \quad (2.10)$$

$$C(\omega) \approx \frac{1}{\gamma P_0} \left[ 1 + (\gamma - 1) \frac{2}{r_0} \left( \frac{\eta}{i\omega \rho_0 \text{Pr}} \right)^{1/2} \right]. \quad (2.11)$$

Stinson & Champoux (1992) performed calculations for various pore cross sections and showed that the frequency-independent structural factor can be used as a multiplier to the scale parameter to find the dynamic parameters of a porous material. The complex density is expressed in the form

$$\rho(\omega) = \rho_0 + (\sigma / i\omega) F(H). \quad (2.12)$$

The function  $F$  is modified as

$$F(H) = -\frac{1}{4} \frac{\sqrt{-iH} \cdot T(\sqrt{-iH})}{1 - 2T(\sqrt{-iH})/(\sqrt{-iH})}. \quad (2.13)$$

The scale parameter is defined as  $H = s_h (8\rho_0 \omega q^2 / \phi \sigma)^{1/2}$ , where  $s_h$  is the shape factor; for the cylindrical pore of circular cross-section  $s_h = 1$ . The complex compressibility is

$$C(\omega) = \left( \frac{1}{\gamma P_0} \right) \left\{ \gamma - (\gamma - 1) \left[ \frac{\rho_0}{\rho_0 + \sigma F(\sqrt{\text{Pr}H}) / (i\omega \text{Pr})} \right] \right\}. \quad (2.15)$$

In this case, the asymptotic expansions of  $\rho(\omega)$  and  $C(\omega)$  are expressed as:

$$\rho(\omega) = \sigma_x / i\omega + (1 + s_h^2 / 3) \rho_0, \quad (2.16)$$

$$C(\omega) = (1/\gamma P_0) \{ \gamma - (\gamma - 1) [i\omega \rho_0 \text{Pr} / \sigma] \} \quad (2.17)$$

- for low frequencies.

$$\rho(\omega) \approx \rho_0 \left[ 1 + s_h (\sigma / 2i\omega \rho_0)^{1/2} \right], \quad (2.18)$$

$$C(\omega) \approx \frac{1}{\gamma P_0} \left[ 1 + s_h (\gamma - 1) (\sigma / 2i\omega \text{Pr} \rho_0)^{1/2} \right] \quad (2.19)$$

- for high frequencies.

Here the relation between the structural factor  $s_h$  and the structural constant  $k_0$ , which is measured in experiments, has the simple form  $s_h = (2/k_0)^{1/2}$ .

With the approach it is possible to determine the model parameters and establish the relation of the porous coating impedance at high (ultrasonic) frequency with the impedance of the same coating of larger thickness at low (sonic) frequencies.

In general, the wave resistance and the propagation constant depend on the scale parameter  $H$  as

$$W' = \frac{W}{\rho_0 c} = \frac{q}{\phi} \left( \frac{f_\rho(H)}{f_c(H)} \right)^{1/2}, \quad (2.20)$$

$$\Gamma = \frac{i\omega}{c} q (f_\rho(H) f_c(H))^{1/2}, \quad (2.21)$$

where  $f_\rho(H)$  and  $f_c(H)$  are dimensionless functions of the complex density and compressibility; i.e.,  $W'_{H=const} = const$ , and  $\Gamma_{H=const} \sim \omega$  at  $H=const$ . For the input impedance of the porous layer attached to a rigid wall, we obtain

$$Z'_{ex} = \frac{Z_{ex}}{\rho c} \Big|_{H=const} = W'_0 c h \left( \Gamma_0 \frac{\omega}{\omega_0} h \right), \text{ at } \rho\omega/\eta = \rho_0\omega_0/\eta, \quad (2.22)$$

where  $W'_0$  and  $\Gamma_0$  are acoustic parameters at  $\omega_0, \rho_0$ .

Thus, the specific input impedance of the porous layer of thickness  $h$  at  $\omega_0, \rho_0$  equals to the input impedance of the porous layer of thickness  $h' = h \frac{\omega_0}{\omega}$  at  $\omega, \rho$ . The latter can be measured in experiments. This similarity is valid at  $H=const$ , that is equivalent to the condition  $\rho\omega = \rho_0\omega_0$  (assuming that the viscosity is constant). The wind-tunnel conditions ( $\rho_0 \sim 0.01\rho_{atm}$ ,  $\omega_0 \sim 300kHz$ ,  $h \sim 1$  mm) can be simulated in the benchmark experiment with  $\rho \sim 0.3\rho_{atm}$  и  $\omega \sim 10kHz$  m using the porous layer of  $h' \sim 30h$ .

## 2.2. Measurement of propagation constant, acoustic resistance, and sound-absorption coefficient

The propagation constant  $\Gamma_m = \beta_m + i\alpha_m$  and the dimensionless wave resistance  $W_1 = W_{r1} + iW_{i1}$  are measured using the method of acoustic interferometer. This method allows us to obtain the absorption coefficient for acoustic waves normally incident on the surface, and to find the complex impedance. However, due to geometrical and dissipation limits, this method can be applied to disturbances of the sound frequency band only.

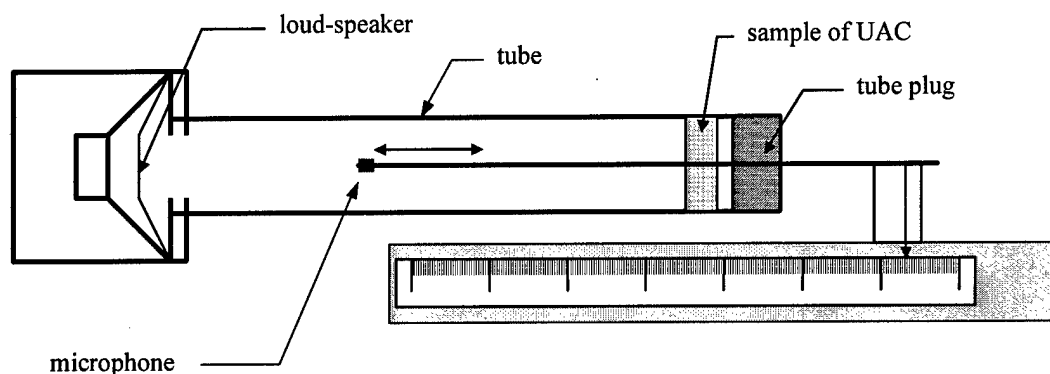


Fig. II.4 Scheme of acoustical interferometer.

The interferometer (Fig. II.4) comprises a cylindrical tube with rigid walls. One end of the tube is a rigid massive wall (tube plug). At the other end, there is a loud-speaker generating acoustic waves. A sample of porous material is placed near the tube plug. Inside the interferometer, there is a probe of 4 mm diameter with a microphone. This probe can be moved along the tube. Maximums and minimums of acoustic pressure  $p_{\max}, p_{\min}$  and their loci  $x_{\max}, x_{\min}$  are measured along the tube axis. These data are used for calculations of  $\Gamma_m$  and  $W_1$ . Parameters of the interferometer are given in the table:

Tube diameter, mm	21
Effective frequency band, kHz	0.6 - 8.5
Effective range of pressure, torr	760 ÷ 30
Sound intensity, dB	75 - 130
Probe phase correction, rad	<0.05
Probe/tube cross-section ratio	0.03



The first acoustic-pressure maximum is observed at the surface of the tube plug, the first minimum is at the distance  $\lambda/4$  from the wall, where  $\lambda$  is acoustic wavelength. These properties are used for tuning of the interferometer.

If the porous sample is placed near the tube plug, the first acoustic-pressure minimum is located at a distance differing from  $\lambda/4$ . The phase shift  $\delta$  of the reflection-from-sample factor is calculated using the measured values of  $x_{\min}, p_{\max}$  (at  $x_{\min}$ ) (Rzhevkin, 1960; Rosin, 1972;

Bogolepov, 1986) as  $2\delta = \frac{2\pi(x_{\min} - \lambda/4)}{\lambda/2}$ , and the standing-wave factor is  $n = |P_{\max} / P_{\min}|$ .

Using the values of  $\delta$  and  $n$ , the input impedance of the porous layer is determined as

$$Z_{ex} = X_{ex} + iY_{ex}, \quad (2.23)$$

$$X_{ex} = \frac{2n}{(n^2 + 1) - (n^2 - 1)\cos 2\delta}, \quad Y_{ex} = \frac{(n^2 - 1)\sin 2\delta}{(n^2 + 1) - (n^2 - 1)\cos 2\delta}. \quad (2.24)$$

The input impedance is expressed in terms of: the porous sample thickness  $s$ , the back-boundary impedance  $Z_2$ ,  $\Gamma_m$  and  $W$

$$Z_{ex} = W \frac{Z_2 \cosh \Gamma_m s + W \sinh \Gamma_m s}{Z_2 \sinh \Gamma_m s + W \cosh \Gamma_m s}. \quad (2.25)$$

Since the tube plug is absolutely rigid, the back-boundary impedance is  $Z_2 = \infty$ . Then, the input impedance of the porous layer is  $Z_{ex(s)} = W \cosh \Gamma_m s$ . If the porous layer is placed at the distance  $\lambda/4$  from the tube-plug surface, then  $Z_{ex(s+\lambda/4)} = W \sinh \Gamma_m s$ .

The input impedances  $Z_{ex(s)}$  and  $Z_{ex(s+\lambda/4)}$  are measured for the porous sample of the thickness  $s$  being attached to the rigid tube plug and being shifted to the distance  $\lambda/4$ , respectively. Then, the acoustic resistance is calculated as  $W = \sqrt{Z_{ex(s)} Z_{ex(s+\lambda/4)}}$ ; its dimensionless quantity is

$W_1 = \frac{W}{\rho_0 c_0} = W_{r1} + iW_{i1}$ . In turn, the propagation constant is determined as

$$\Gamma_m = \frac{1}{s} \operatorname{arth} \sqrt{Z_{ex(s+\lambda/4)} / Z_{ex(s)}}.$$

It is also possible to obtain  $\Gamma_m$  and  $W$  by measuring the input impedances  $Z_{ex(s)}$  and  $Z_{ex(2s)}$  of the two samples with the thickness  $s$  and  $2s$  respectively (both samples are attached to the tube plug). In this case, the acoustic resistance and the propagation constant are calculated using the relations

$$W = \frac{Z_{ex(s)}}{\cosh \Gamma_m s}, \quad \Gamma_m = \frac{1}{2s} \operatorname{arch} \left( \frac{Z_{ex(s)}}{Z_{ex(2s)}} - 1 \right)^{-1}. \quad (2.26)$$

We can also determine the absorption coefficient  $\alpha$  for acoustic waves of normally incidence, using the standing-wave factor  $n$  and the relation

$$\alpha = \frac{4n}{n^2 + 2n + 1} \quad (2.27)$$

The upper limit of acoustic frequency,  $f_{up}$ , corresponds to the case when the half wavelength is approximately equal to the largest transverse size of the tube:  $f_{up} = \frac{c_0}{2d}$ , where  $d$  is tube diameter. Below this frequency, the tube can be treated as a long line and acoustic waves are almost flat. The lower limit is estimated from the condition that the standing wave has at least two minimums and two maximums of the acoustic pressure:  $f_{low} = \frac{c_0}{2L}$ , where  $L$  is the interferometer tube length.

To determine the active component of the material impedance, and its dependence on the mean pressure, the resonance method is used. In this case, the porous material sample is placed at a certain distance from the rigid tube plug. The volume of air in the tube between the sample and the wall is the resonator volume. The resonant frequency is observed when the elastic and inertial components of the system impedance are equal to each other. At this frequency the absorption is maximal.

If a quarter of the wavelength equals the sample-to-rigid wall distance, the air impedance in the resonator's volume is zero; i.e., the total wave load is applied to the sample. In this case, the real parts of reactive ( $R$ ) and inertial ( $M$ ) components of the impedance are related to the porous material. If the half wavelength equals the sample-to-rigid wall distance, then the absorption is minimal.

In Fig. II.5, the absorption coefficient of the perforated sheet is shown as a function of the dimensionless frequency parameter  $kl$ , where  $k$  is wavenumber and  $l$  is the distance to the rigid wall.

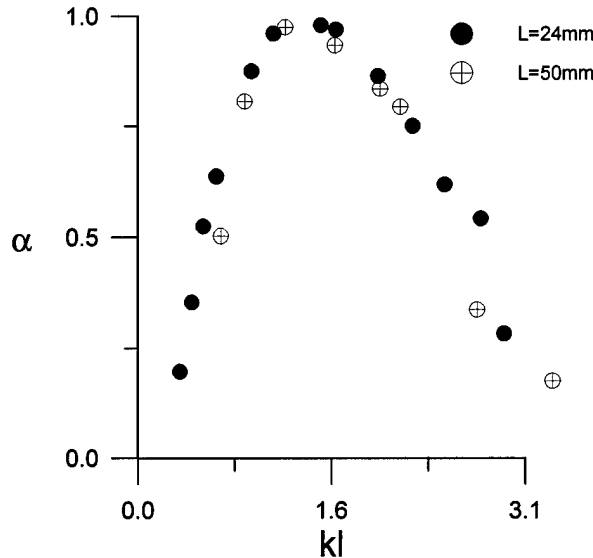


Fig. II.5 The absorption coefficient of the perforated sheet as a function of the dimensionless frequency parameter  $kl$  ( $k$  is wavenumber,  $l$  is the distance to the rigid wall); black symbols  $\tilde{\alpha}$   $l=24$  mm; white symbols  $\oplus$   $l=50$  mm.

The measurements were performed at atmospheric pressure. This distribution indicates the active component of the specific impedance is close to 1 at the resonant frequency; i.e., full absorption is observed. The reactive component of the impedance is not zero, since the resonant frequency is lower than  $kl/2$ .

Figure II.6 shows the real and imaginary parts of the specific input impedance for the porous sample attached to the wall. Figure II.7 shows the adsorption coefficient  $\alpha$  as a function of sound frequency. Note that below the frequency of 2 kHz the absorption was too low to be measured by the interferometer.

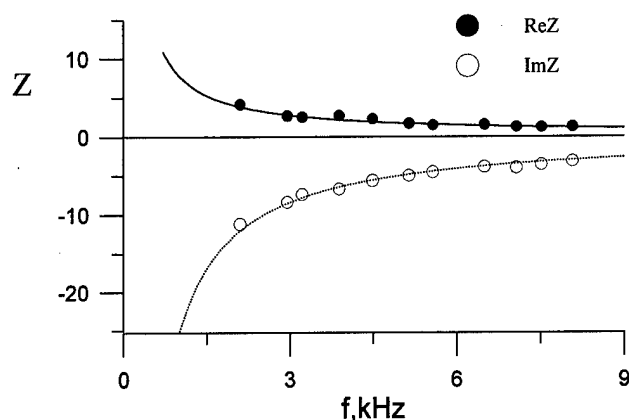


Fig. II.6 The specific input impedance for the porous sample attached to the tube plug.

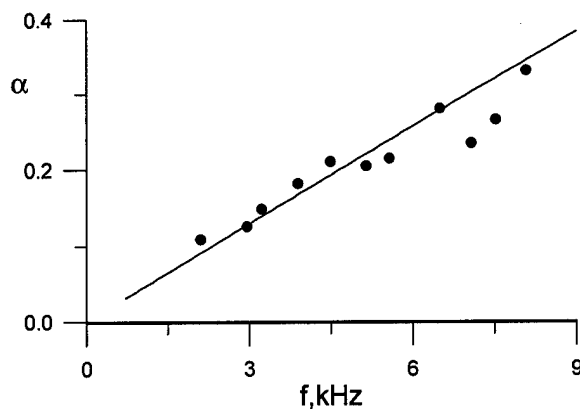


Fig. II.7 The adsorption coefficient for the porous sample attached to the tube plug.

The absorption coefficient increases almost linearly in the sonic frequency band. The absorption occurs with a small negative phase decreasing with frequency. The behavior of the input impedance indicates that the elastic components (which are inversely proportional to the frequency) are dominant.

For the porous sample placed at the distance  $\lambda/4$  from the tube-plug surface, the impedances of the air layer is negligible compared to the impedance of the rigid tube plug. With the appreciable

absorption in the volume between the sample and the wall this is not entirely correct (Voschukova, 1985). Nevertheless, this approach is commonly accepted. For this configuration, the input impedance is the impedance of load on the porous material. The results are shown in Figs. II.8 and II.9.

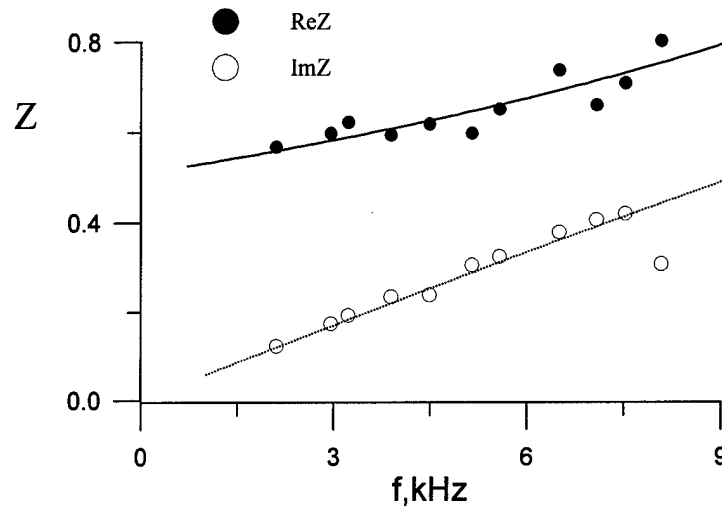


Fig. II.8 The specific input impedance for the porous sample at the distance  $\lambda/4$  from the tube plug.

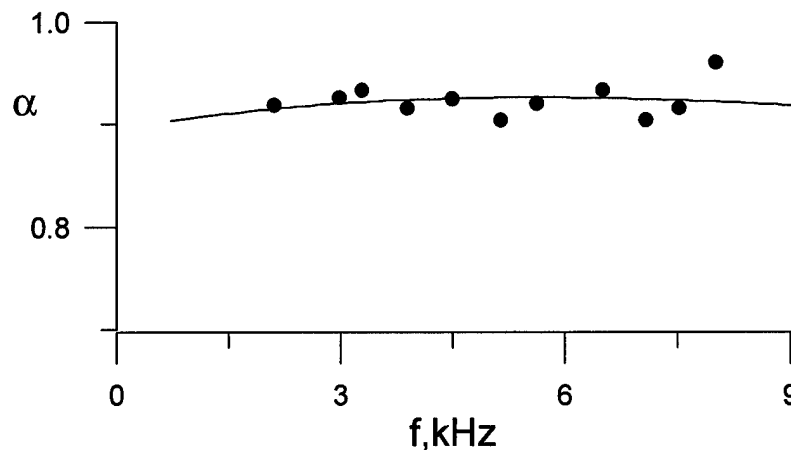


Fig. II.9 The absorption coefficient for the porous sample at the distance  $\lambda/4$  from the tube-plug surface.

Theoretically, as the frequency decreases the active component of the input impedance tends to the specific mechanical resistance and the active component tends to  $ik_1 \alpha \rho_0 h$ . The linear approximation of the experimental data gives  $R = 0.55$ , which is very close to the specific mechanical resistance  $= 0.56$ , which was measured directly. The parameter  $k_1$  is 1.363, which is

close to the theoretical quantity  $4/3$  for the cylindrical pore of circular cross-section. Moreover, the effective pore diameter, calculated from the experimental data, is  $53\text{ }\mu\text{m}$ , which is close to the average diameter  $50\text{ }\mu\text{m}$  of actual pores.

Sample	Structural factor $s$	Tortuosity $q^2$	Added mass coefficient $k_1$	Effective pore diameter, $\mu\text{m}$ .
Perforated sheet	1.04	1	1.363	53

At high frequencies, the active component of the input impedance and the absorption coefficient are significantly higher than their theoretical values. Voschukova (1985) pointed out that the considerable increase of the active component is associated with the increase of absorption in the resonator volume with decreasing of the resonator length.

The experimental values of the input impedance allow us to obtain the frequency dependencies for the wave resistance and the propagation constant. The latter can be used for predictions of the input impedances of various absorption systems with this porous material. For the sonic frequency band, the specific values of the wave resistance and the product  $\Gamma h$  of the propagation constant and the sample thickness are shown in Figs. II.10, II.11. The solid and dotted lines represent the theoretical dependencies, which agree well with the experimental data (symbols) in the sonic frequency band at atmospheric pressure. Using the theoretical model one can extrapolate these dependencies to other frequencies and ambient pressures.

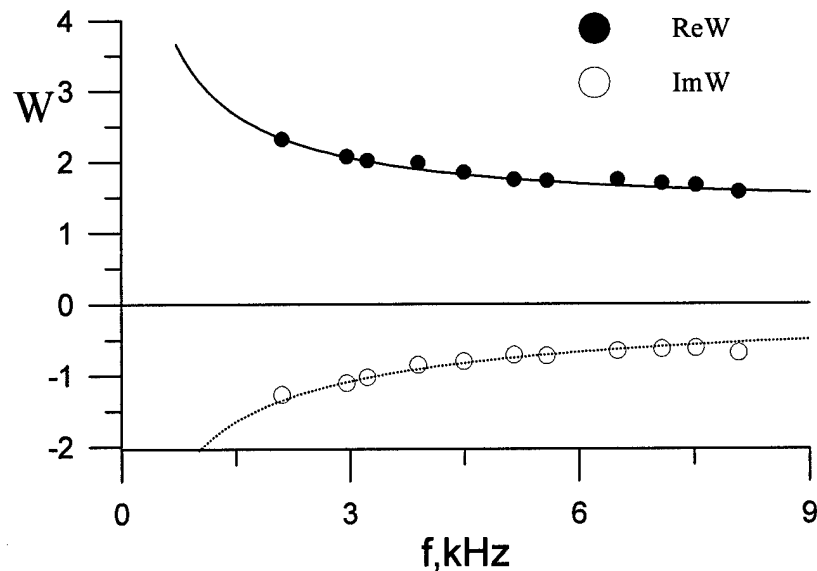


Fig. II.10 The specific wave resistance of the porous material; symbols  $\bullet$  experiment, lines - theory.

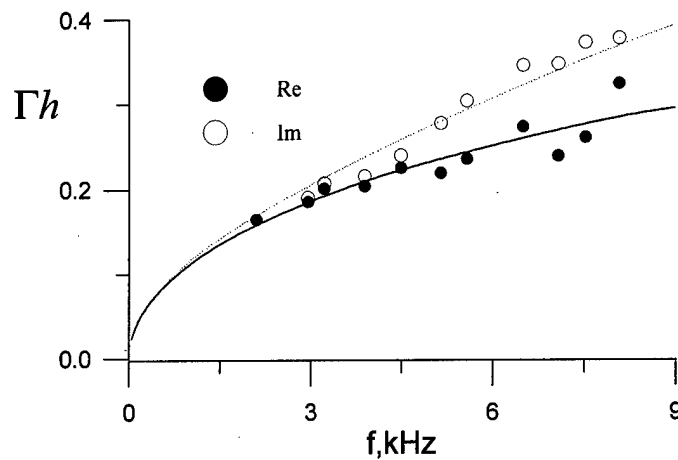


Fig. II.11 The product  $\Gamma h$  for the porous material; symbols - experiment, lines - theory.

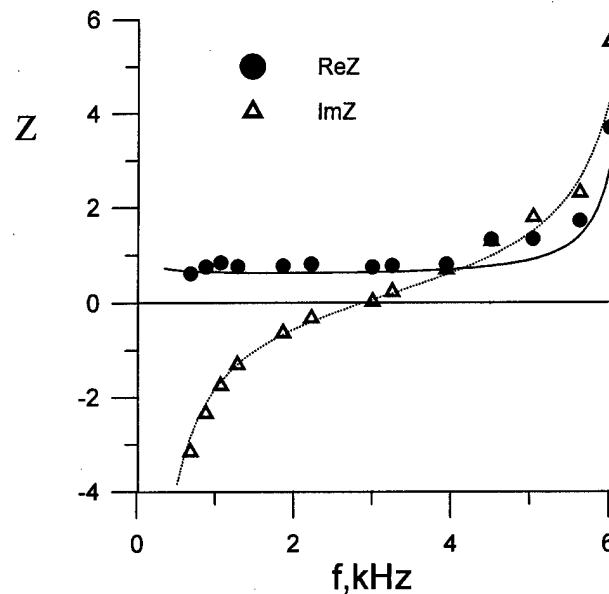


Fig. II.12 The input impedance at atmospheric pressure; the porous sample is at the distance  $l=24$  mm from the tube-plug surface; symbols - experiment, lines - theory.

To determine the dependence of the acoustic absorption on ambient pressure, measurements were performed at low air densities. The pressure was varied in the range 760-180 mm m.c. Figure II.12 shows the input impedance at atmospheric pressure, with the porous material being placed at the distance  $l=24$  mm from the end wall. In Fig. II.13, the absorption coefficient is shown as a function of frequency at various pressures. The frequency band covers the region, in which the resonator impedance is dominated by elastic forces, as well as the resonant-frequency vicinity. The experimental data (symbols) are compared with the theory (lines). Within the considered pressure range, the active component of specific impedance grows as the pressure decreases. This leads to flattening of the resonant curve. The absorption coefficient near the resonant frequency has non-monotonic behavior versus pressure. The absorption phase near the

resonant frequency has a jump. As the pressure decreases this jump decreases and disappears at the active impedance component=1.

For the sample locus  $l=50$  mm, data measured near the resonant frequency at various pressures, are presented in Fig. II.14 (for the absorption coefficient) and 15 (for the phase shift of the absorption coefficient). Figure II.16 shows the active component of the input impedance. As in the case of  $l=24$  mm (Fig. II.13), the data (symbols) agree well with the theoretical predictions (solid and dotted curves). This leads to the conclusion that the theoretical model can be used for calculations of the porous layer characteristics for high frequencies.

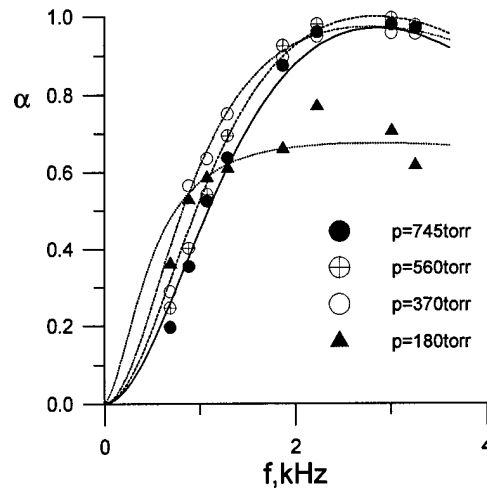


Fig. II.13 The absorption coefficient as a function of frequency at various pressures; the porous sample is at the distance  $l=24$  mm from the tube-plug surface; symbols - experiment, lines - theory.

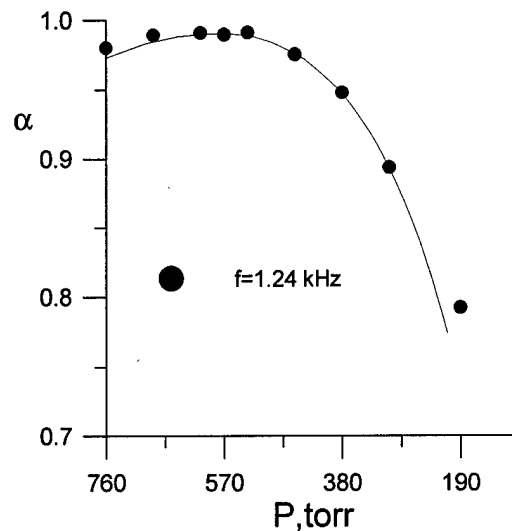


Fig. II.14 The absorption coefficient as a function of pressures at  $f=1.24$  kHz; the porous sample is at the distance  $l=50$  mm from the tube-plug surface; symbols - experiment, lines - theory.

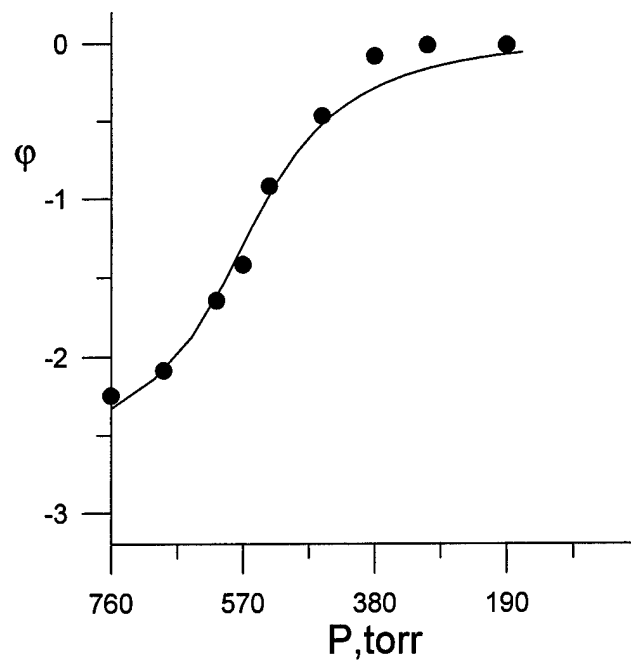


Fig. II.15 The absorption-coefficient phase shift as a function of pressures at  $f=1.24$  kHz; the porous sample is at the distance  $l=50$  mm from the tube-plug surface; symbols - experiment, lines - theory.

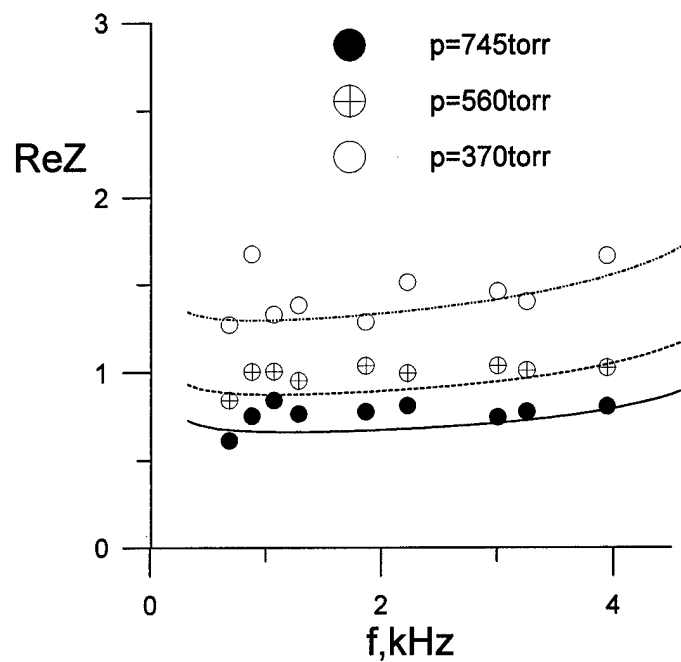


Fig. II.16 The active component of the input impedance at various pressures; the porous sample is at the distance  $l=50$  mm from the tube-plug surface; symbols - experiment, lines - theory.



### 2.3. Summary

The acoustic interferometer has been developed for benchmark measurements of acoustic characteristics of porous materials within the range of frequencies of 0.6 to 8.5 kHz and air pressures of 760 to 30 torr. In this range of parameters, the wave resistance and propagation constant were measured for the UAC of regular microstructure, namely, the metal sheet perforated with equally spaced cylindrical blind micro-holes.

The theoretical model, which is based on the unit problem describing propagation of acoustic disturbances in a long cylindrical tube, was used for prediction of the UAC impedance and absorption coefficient. The benchmark measurements agree well with theoretical predictions.

The theoretical model gives a similarity law, which allows for extrapolation of benchmark data to low pressures and high frequencies typical for hypersonic wind tunnel tests and flight.

Using a combination of theory and benchmark experiment, it is feasible to design ultrasonically absorptive coatings and evaluate their performance for hypersonic laminar flow control.

## Chapter III. Wind Tunnel Experiments and Comparison with Theory

### 3.1. Experimental model

The model is a 7 half-angle sharp cone of 500 mm length. Its general view is presented in Fig. III.2. Schematics of the model are given in Fig. III.2. The model consists of the following main parts:

- Sharp cone nose of 65 mm length
- Middle part of 65 mm length with the electric glow discharge source
- Base part of 370 mm length covered by the porous coating, which leading edge is located at 182 mm distance from the cone tip
- Unit for model turning

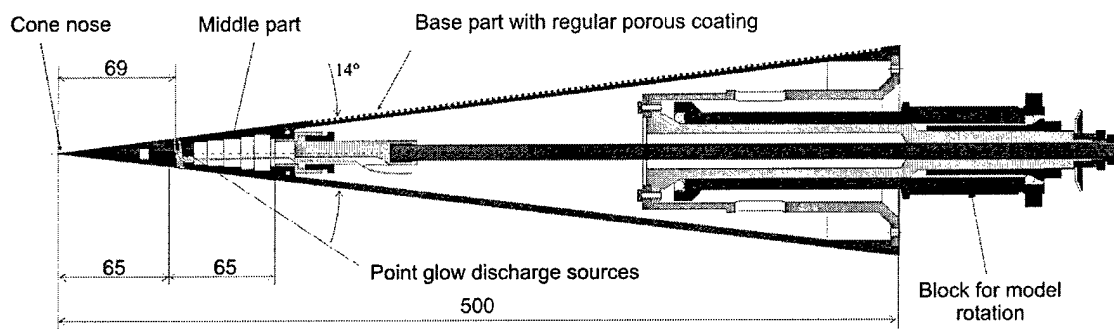


Fig. III.1 General view of the model.

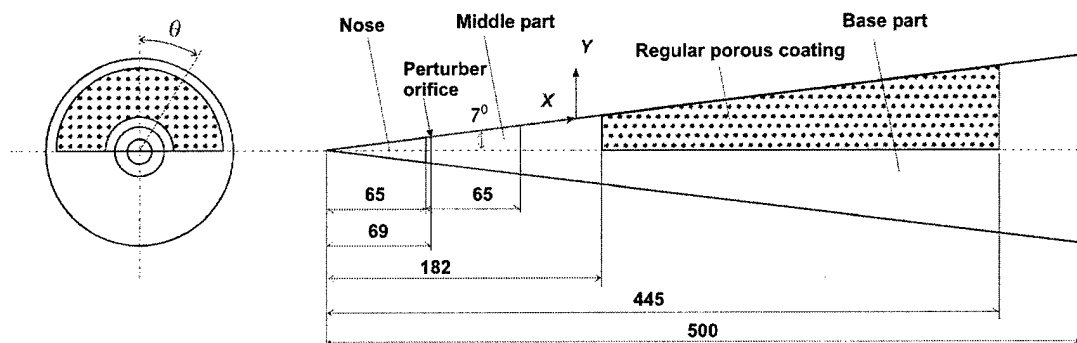


Fig. III.2 Schematics of the model.

### 3.1.1. Perforated sheet

Parameters of the porous coating and manufacturing are similar to the GALCIT T-5 experiments (Rasheed *et al.*, 2001). The laser drilled sheet (see Fig. III.3) of 304SS stainless steel with thickness 450  $\mu\text{m}$  is manufactured by ActionLaser Pty Ltd (Unit 1, 39 King Rd, Hornsby, NSW 2077, Australia). The diameter of round cylindrical microholes is 50  $\mu\text{m}$ , the distance between holes (spacing) is 100  $\mu\text{s}$ , and the open area (porosity) is 0.2. The total perforated area is approximately 33500  $\text{mm}^2$  and the number of holes is about 3.35 millions. Additionally, the rectangular metal sheet (dimensions 109x300 mm) of the same thickness and material was made solid (without holes). A 40x40  $\text{mm}^2$  coupon of the laser-drilled sheet was also manufactured for benchmark measurements of sound absorption (see Chapter II).

The holes have a conical shape. Fig. III.4, III.5 show two sides of the perforated sheet. The average hole diameter is  $64 \pm 6$   $\mu\text{m}$  at the laser beam input (back side) and  $50 \pm 6$   $\mu\text{m}$  at the beam output (face side), so that the hole taper angle is about  $0.9^\circ$ .

The micrograph (Fig. III.6) shows that hole edges are ragged. The holes are situated in rows with spacing about  $100 \pm 4$   $\mu\text{m}$ . The average distance between rows is 100  $\mu\text{m}$  (Fig. III.7).

In some areas of the perforated surface, the hole rows are very close to each other so that neighboring holes are "merged" (Fig. III.7). Four "merged" rows were found on the total coating. The mechanical strength of the perforated sheet perpendicularly to these rows is low. The tensile load is applied in parallel to the "merged" rows direction, so these rows weakly affected the tension.

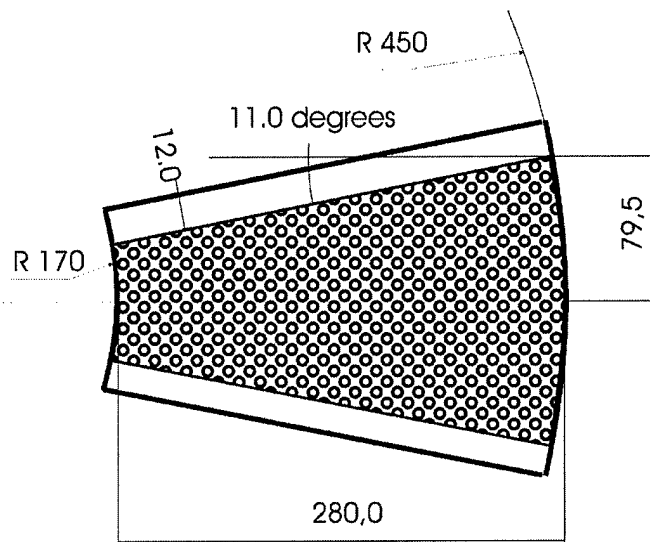


Fig. III.3 Perforated sheet.

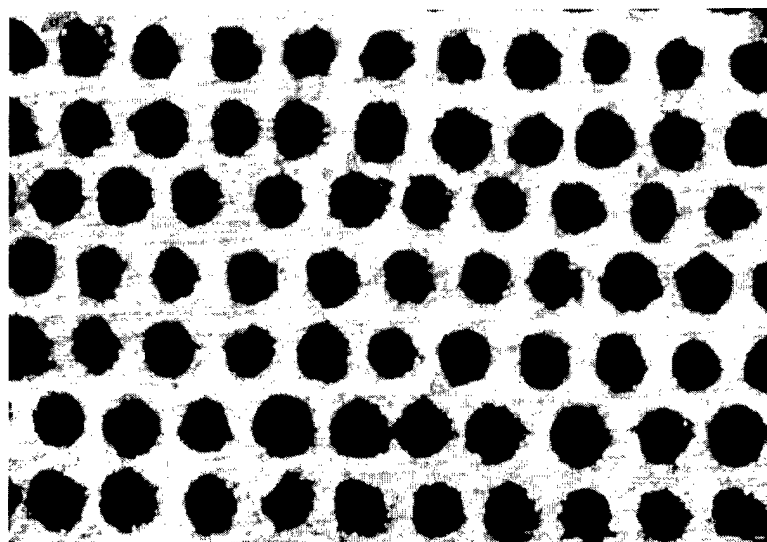


Fig. III.4 Back side of the perforated sheet.

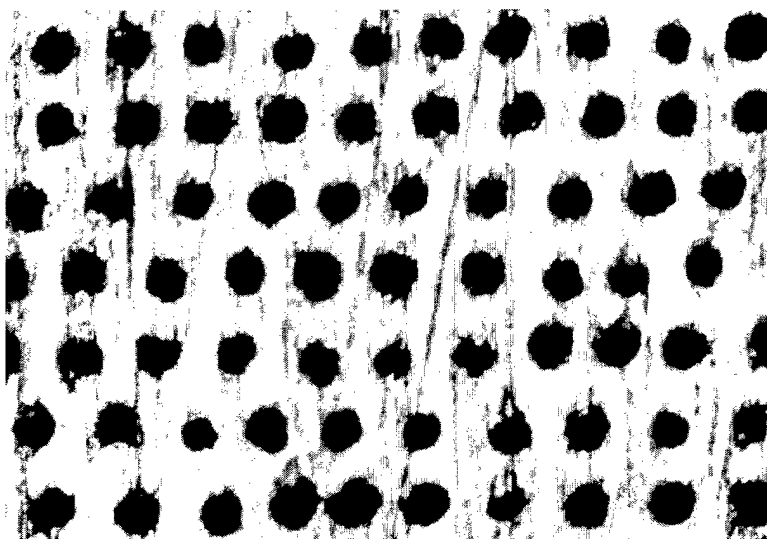


Fig. III.5 Face side of the perforated sheet.

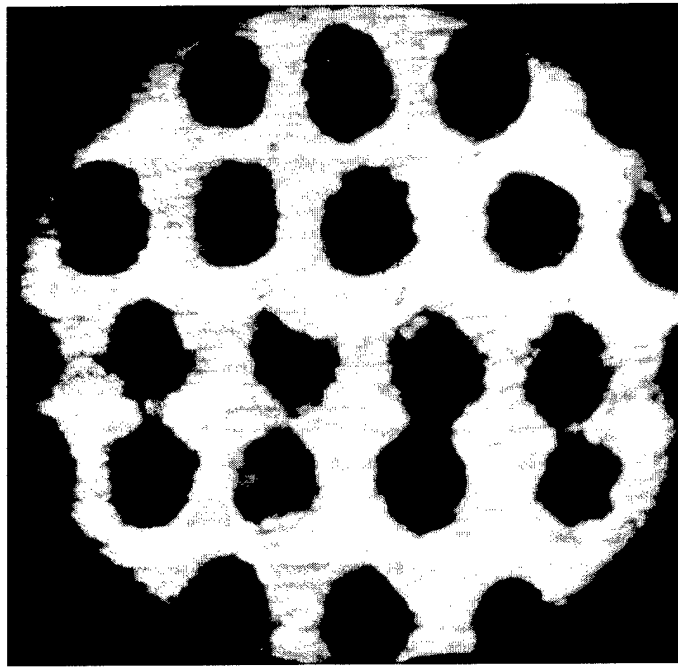


Fig. III.6 Micrograph of holes in the perforated sheet.

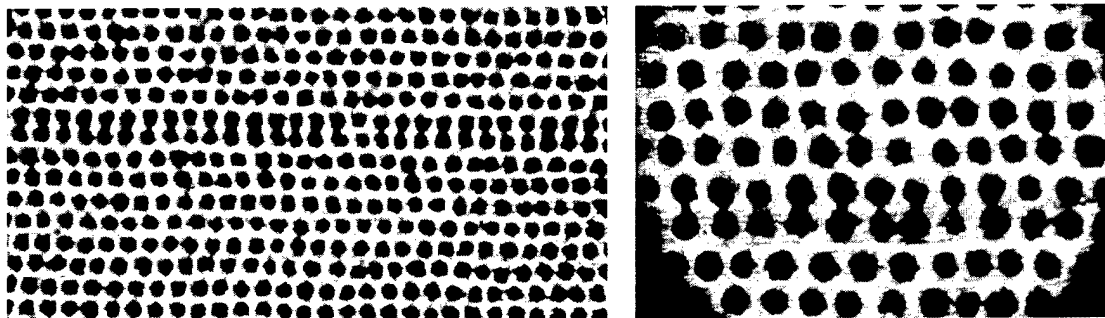


Fig. III.7 Perforated sheet with merged rows of holes.

### ***3.1.2. Technology of manufacturing***

A cross-section of the model base part is schematically shown in Fig. III.8. Manufacturing of this part includes the following steps:

1. Manufacturing of a hollow metal truncated cone.
2. Milling of through grooves of 10 mm width, 276 mm length to tense the perforated sheet.
3. Lathe turning of 0.45 mm depth hollow for the perforated sheet.

4. Filing the hollow with epoxy onto the model opposite side.
5. Leveling of the epoxy surface. To avoid misalignment between the cone surface and the porous coating, the cone surface was turned to the depth equal to the coating thickness.
6. Riveting of cover straps onto the sides of the perforated sheet for tension it onto the model.
7. Cleaning of the perforated sheet in an ultrasonic bath with tetrachlorethylene.
8. Tension of the perforated sheet onto the model by custom built tension mechanism (Fig. III.9). During tension process a bend region was close to the perforation and solid strips at the sides of perforated sheet were break away. Instead of the broken strips, metal strips of 0.25 mm thickness were attached by laser welding. Because of relatively high flexibility of the welded strips, the perforated sheet was successfully tensed onto the model (Fig. III.10).
9. Checking of the porous coating level.
10. Puttying and treatment of the model surface.
11. Final treatment of the model with painting and polishing.

The roughness of the uncovered and polished part of the cone is  $\leq 0.5 \mu\text{m}$ .

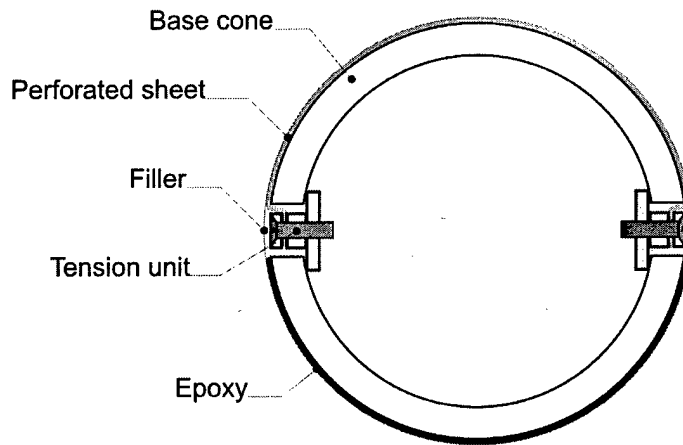


Fig. III.8 The structure of the base part of the model.

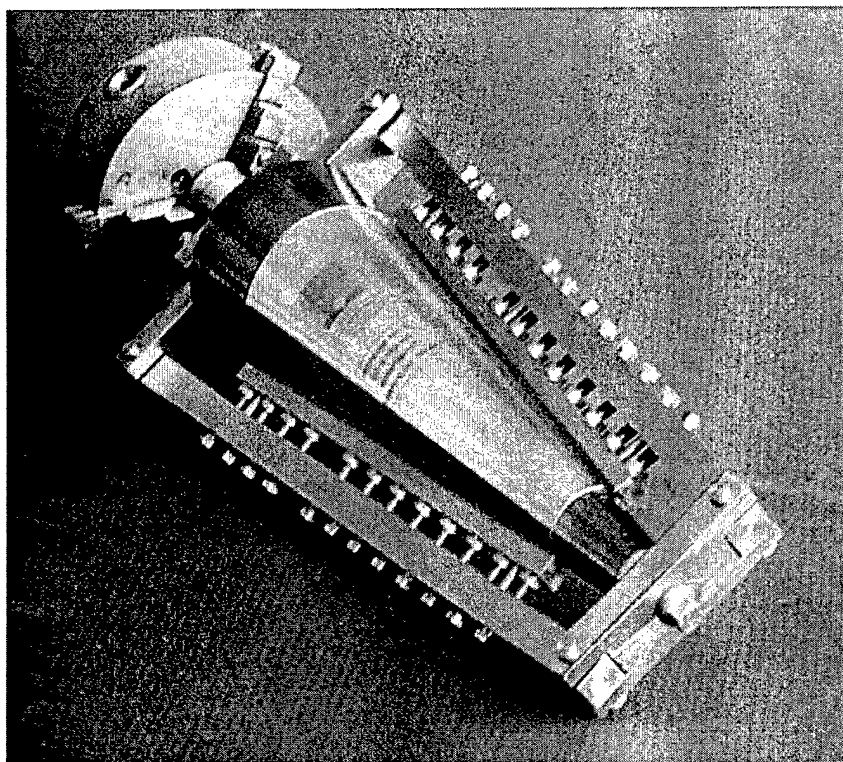


Fig. III.9 Model installed in the tension mechanism.

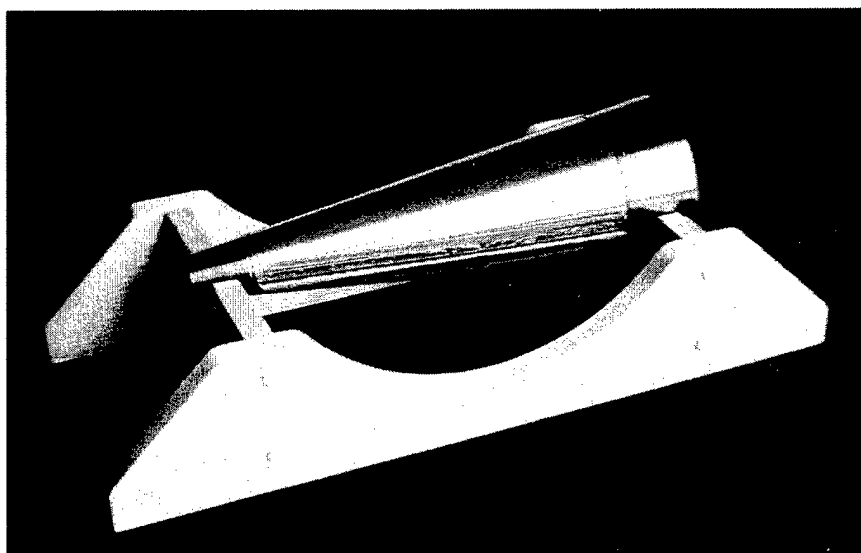


Fig. III.10 Base part with the regular porous coating.

## 3.2. Experimental equipment and techniques

### 3.2.1. Wind tunnel

Experiments were carried out in the hypersonic blow-down wind tunnel T-326 of ITAM SB RAS (see Fig. III.12). This tunnel was designed for the Mach numbers  $M_\infty=6-14$  and the unit Reynolds numbers  $Re_1 = (5 \cdot 10^6 \div 70 \cdot 10^6) \text{ m}^{-1}$ ; there is a set of changeable profiled and conic axis-symmetric nozzles. The tunnel is equipped with a one-step perforated ejector.

The maximum pressure in the settling chamber is of 20 MPa; the pressure in the ejector is of 0.8 MPa; the runtime is up to 30 min. For the Mach numbers range 6-10, an ohmic heater is used for maintaining air temperature in the settling chamber up to 800 K. The open-jet test section has the length of 400 mm with the nozzle end diameter of 200 mm. To increase the sensor lifetime and to exclude effects of dust particles on measurements, a block of fine air cleaning is installed between the air heater and the nozzle. This block filters dust particles of the size  $>2 \mu\text{m}$ . A mechanism of model injection into a free stream allows for protection of models and sensors from non-stationary loadings during tunnel starting. The test section is equipped with two optic windows of 220 mm clear diameter, which are used for model examination and flow visualization.

Experiments were performed at the freestream Mach number  $M_\infty = 5.95$ . The Mach number flow-field nonuniformity is 0.7% in the flow core. The test core diameter is approximately 180 mm. The noise level is about 1% that is typical for conventional hypersonic wind tunnels. The stagnation pressure  $P_0$  and stagnation temperature  $T_0$  were measured during the run and kept at constant with accuracy 0.06% and 0.25%, respectively. The pressure  $P_0$  was measured with the help of the pressure gage IPD-89008 (the measurement ranges are 1.0 MPa, 1.6 MPa and 2.5 MPa). A nameplate error of the pressure gage IPD-89008 is 0.06% of the measurement range. All measurements of  $P_0$  were carried out within the range of 1.6 MPa. The stagnation temperature  $T_0$  was measured by the k-type thermocouple with the sensitivity coefficient of  $4.024 \cdot 10^{-2} \text{ mV/grad}$ . The accuracy of  $T_0$  measurement was 0.1%.

### 3.2.2. Alignment of the model at zero angles

The alignment of the cone along the flow axis was achieved using the following procedure. To be adjusted first was the pylon of the model. The rotation unit with mirror mounted on its face was installed on the pylon (see Fig. III.13). The inclination angle of the mirror to the mounting-face plane of the mirror-rotating unit could be finely adjusted. Further, the settling chamber of the wind tunnel should be removed. Two transparent circular diaphragms with 1.5 mm diameter central orifice were inserted into the inlet and outlet sections of the nozzle. A laser beam was directed through these openings. Displacing the pylon frame we could hit the mirror center by the laser beam. Then, the mirror unit is rotated with simultaneous adjustment of the inclination angle of the mirror to the mounting-face plane of the mirror-rotating unit until the beam reflected from the mirror no longer wobble. After that, the mirror plane was assumed to be normal to the axis of rotation and, hence, to the axis of the drive opening of the pylon. Then, the diaphragm installed at the nozzle exit was removed. Varying the pylon installation angle we forced the reflected beam fall onto the laser output window. Now, the axis of the rotation unit could be believed coincide to the nozzle axis, and the pylon was to be rigidly fixed to the pylon frame, as well as the pylon frame to the base of the test section of the wind tunnel. Subsequently, the model was installed on the rotation unit, and the settling chamber was mounted in its proper place. This alignment procedure allows us to install the model at zero angle of attack with accuracy  $0.05^\circ$ .



### 3.2.3. Traverse system

The T-326 wind tunnel is equipped with a three-component traverse system, which provides 0.01 mm accuracy in motion over the coordinates  $X$ ,  $Y$ ,  $Z$  (the coordinates  $X$ ,  $Y$  are shown in Fig. III.11). The model is turned around the longitudinal axis using the rotation unit providing  $0.1^\circ$  accuracy of the turning angle.

### 3.2.4. Hot-wire anemometer system

Boundary-layer disturbances are measured using the constant current anemometer (CCA) manufactured in ITAM. The CCA consists of the two main circuits:

- Low-frequency (0 to 10 Hz) circuit to provide constant mean resistance of the hot-wire.
- High-frequency (<500 kHz) compensating amplifier to overcome degradation of the hot-wire sensitivity with increasing of frequency.

The measurements are carried out with a single-component hot-wire sensor made of tungsten wire of 1 mm length and 5  $\mu\text{m}$  diameter.

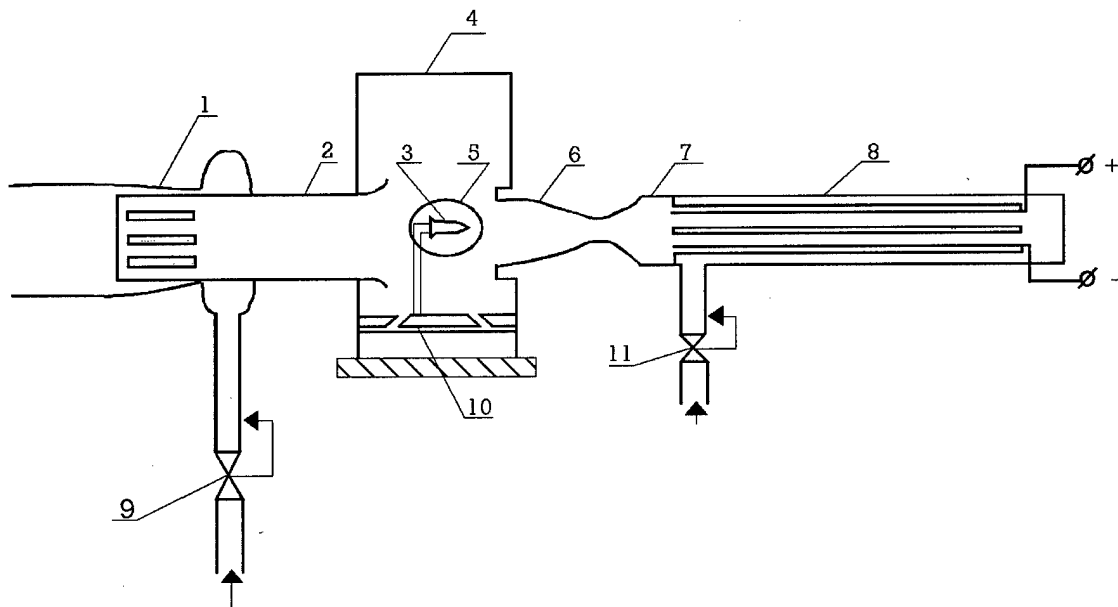


Fig. III.12 Scheme of the T-326 hypersonic wind tunnel of ITAM SB RAS.

1- ejector, 2- diffuser, 3- model, 4- open-jet test section, 5- optical windows, 6- axisymmetric nozzle, 7- prechamber, 8- heater, 9, 11- control valves, 10- device to put model into free stream.

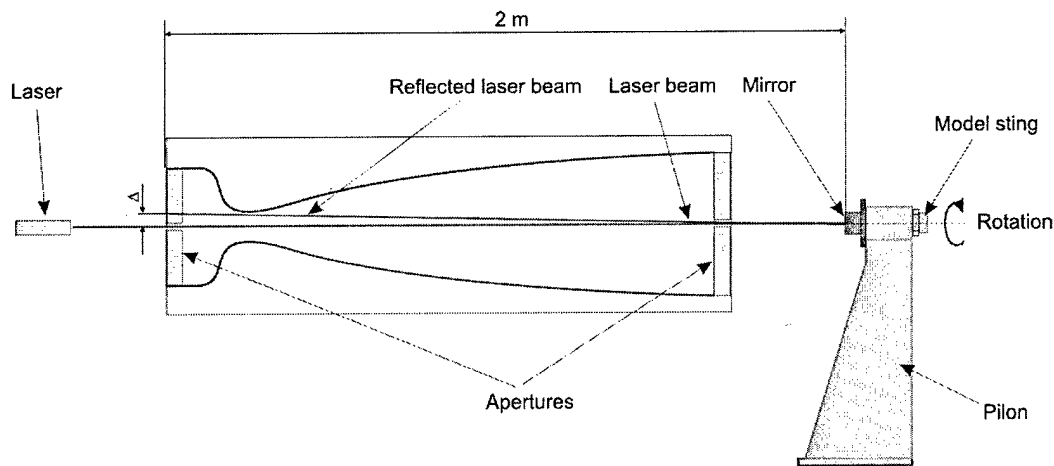


Fig. III.13 Alignment at zero angles procedure.

### 3.2.5. System of measurement control and data acquisition

The system of measurement control and data acquisition structurally consists of the two parts: 1) System of free-stream parameters control, mean parameters ( $P$ ,  $T_0$ ) measurement and traverse system device operating; 2) Computer hot-wire measurements system.

**1) System of freestream parameters control, mean parameters measurement and traverse system device operating.** The freestream parameters are determined from measurements of  $P_0$  and  $T_0$ . To measure  $P_0$ ,  $T_0$ , and  $T_w$ , the ADC PCI-9114HG (© ADLINK Technology Inc., Taiwan) PC data acquisition card is used. This ADC provides the following advanced features:

- 16 differential analog inputs;
- 16 bits high resolution AD conversion;
- Sampling rate up to 100 kHz;
- Input range:  $\pm 10V$ ,  $\pm 1 V$ ,  $\pm 0.1 V$ ,  $\pm 0.01 V$ .

Signals from each sensors and thermocouples are digitized with the frequency of 30 kHz. Each set of 512 samples are averaged and mean values are stored in the personal computer memory.

The traverse gears are controlled using a personal computer or manually. The software developed for this part of the measurement system allows an experimentalist to monitor free-stream parameters during the run, operate the traverse gears, record the experimental data and start up the hot-wire system.

**2) Computer hot-wire measurements system** consists of a personal computer and PCI-9812 (© ADLINK Technology Inc., Taiwan) PC data acquisition card. This ADC provides the following advanced features:

- 4 single-ended analog input channels;
- 12-bit analog input resolution;
- Up to 20MHz A/D sampling rates;

- 4 A/D converters, one converter for each analog channel;
- Trigger Sources: Software, Analog threshold comparator using internal D/A to set trigger level, and External digital trigger.

During hot-wire measurements of natural disturbances, 1 time-series of 401408 samples each are acquired at each measurement station. During measurements of artificial disturbances, 98 time-series of 4096 samples each acquired at each measurement station. Analog signal of main generator initiating the glow discharge is used for triggering ADC. Since the output signal of CCA has a high level of high-frequency signals, the sampling rate is increased up to 5 MHz to avoid aliasing.

The software allows for processing data (spectra, amplitude and phase characteristics of artificial disturbances) in the real time and plotting them on the monitor. During the run, parameters of artificial disturbances, sensor locations and free-stream characteristics were stored into a PC hard disk. At the same time, the experimental program is controlled by the second computer, and exchange of information between computers is performed by Ethernet, protocol TCP/IP. Thus, the experimental process is fully automated. All measured time-traces are stored in PC and burned to CD-ROMs. This allows for carrying out detailed analysis of the data after experiments.

### **3.2.6. The system of high-frequency glow discharge**

The glow-discharge system consists of a clock generator and high-voltage generator. The clock-generator signal is used to initiate the high-voltage generator and synchronize hot-wire measurements with the high-voltage generator starting up. The high-voltage generator produces voltage pulses up to 2000 V, of 1  $\mu$ sec duration and the pulse frequency up to 400 kHz. During the run the glow discharge is controlled visually through optic windows and a mirror in the test section.

Ring and point sources were tested in hypersonic flows. During testing the electrode shapes were optimized to improve the discharge efficiency. Also the new circuit (providing more power, higher frequency range and less electric interference with hot-wire) was successfully examined.

### **3.2.7. Processing of wave characteristics of the disturbances**

To obtain the amplitude  $A$  and phase  $\Phi$  of the controlled disturbances, the discrete Fourier transformation is used

$$A(X, Y, \theta) e^{i\Phi(X, Y, \theta)} = \frac{2}{N} \sum_{j=1}^N \rho U_n(X, Y, \theta, t_j) e^{-i\omega t_j}, \quad (3.1)$$

where  $N$  is the samples count in the time-series,  $\omega$  is frequency of controlled disturbances,  $\rho U_n(X, Y, \theta, t_j)$  is the time-series of mass-flow pulsations.

To compare the experimental and theoretical data, the artificially excited wave packet is decomposed to waves. For this purpose, the transversal wave spectra were computed as

$$SA(x, \beta) e^{iSF(x, \beta)} = \int_{-\theta_0}^{\theta_0} A(x, \theta) e^{i\Phi(x, \theta)} e^{-i\beta\theta} d\theta, \quad (3.2)$$

where  $SA$ ,  $SF$  are the amplitude and phase spectra with respect to the transversal wave

number  $\beta$ .

### 3.2.8. Measurements of natural and artificial disturbances

Fig. III.14 schematically shows the measurement procedure, which includes the following steps:

- **Vertical distribution measurements:** The hot wire is moved up vertically. The measurements are carried out with  $\approx 0.03$  mm step at the distance of 0.9 mm, then with  $\approx 0.05$  mm step at the distance of 1 mm, and then with 0.1 mm step of at the distance of 2 mm.
- **Transversal distribution measurements:** The hot wire is moved vertically down to the pulsation maximum. The maximum locus is determined at the previous step. Then the model is rotated within the angle range  $\theta = \pm(20 \div 30)^\circ$ , depending on wave packet width, and measurements are carried out with the step of  $\approx 0.5^\circ$ . This procedure also allows for checking of the boundary-layer uniformity in the transverse direction.
- **Longitudinal distribution measurements:** The model is turned back to the position  $\theta = 0$ . Then, the hot wire is moved upstream parallel to the cone surface (at  $7^\circ$  angle) with the step  $\Delta X = 0.25$  mm to the distance of 35 mm. This procedure allows for measurements of the artificial wave-packet phase along the cone surface in the layer of maximum mass-flow pulsations
- Then the procedure is repeated

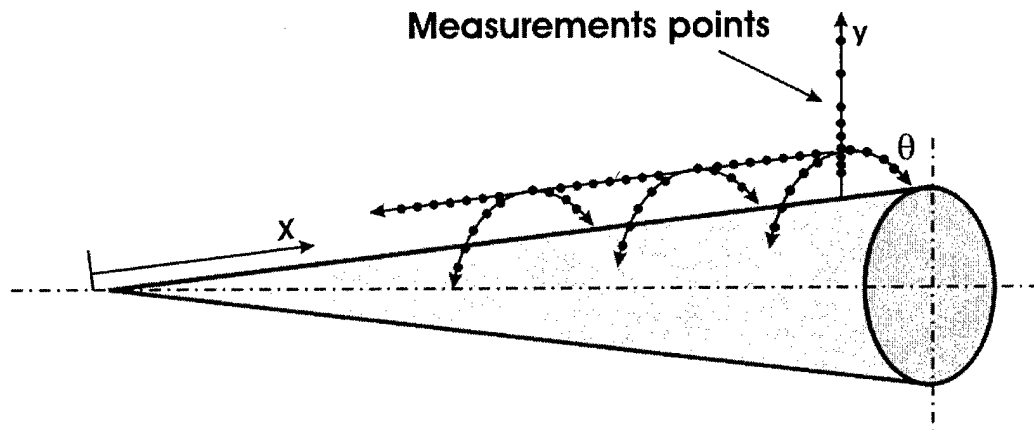


Fig. III.14 Procedure for measurements of natural and artificial disturbances.

### 3.3. Results of measurements

Experiments are carried out at the conditions:

$$P_0=1000 \text{ kPa}; T_0=385\text{-}400 \text{ K}; M_\infty=5.95; \text{Re}_{1\infty}=(11.5\text{-}12.3)\times 10^6 \text{ m}^{-1}; T_w/T_0=0.80\text{-}0.84.$$

#### 3.3.1. Mean flow

Measurements of the mean boundary-layer characteristics are carried out using the hot-wire anemometer described in Section 3.2.4. The upstream end of the investigated region on both solid and porous sides is located ahead of the UAC leading edge, which is  $X=182 \text{ mm}$  ( $\text{Re}_{eX}\approx 2.8\cdot 10^6$ ).

The mean mass flow  $\rho U$ , mean flow velocity  $U$  and RMS mass-flow pulsations are shown in Fig. III.15 ñ Fig. III.20 as functions of the vertical coordinate for the solid and porous sides at various  $X$ -stations. In Fig. III.21 ñ Fig. III.26, the same distributions are presented in nondimensional forms. The mass flow and velocity are normalized using their values at the upper boundary-layer edge. The vertical coordinate  $y$  is normalized with respect to the boundary-layer thickness  $\delta$ .

For  $X=138$  ñ  $287 \text{ mm}$ , the profiles of  $\rho U/(\rho U)_e$ ,  $U/U_e$  on the solid and porous sides are similar to each other; they are close to the correspondent profiles calculated for the laminar boundary layer. The profiles of RMS pulsations are typical for the hypersonic laminar boundary layer. They have a large narrow peak in the vicinity of  $y\approx 0.8\delta$ . These data confirm that boundary layers are laminar on the solid and porous sides.

Fig. III.27 compares  $U$  and  $\langle \rho U \rangle / \rho U$  on the solid and porous sides. These profiles are close to each other; i.e., the porous coating does not affect mean-flow characteristics and RMS mass-flow pulsations.

#### 3.3.2. Natural disturbances

Spectra of mass-flow disturbances were measured at the coordinate  $y$  relevant to maximum pulsations. Hot-wire measurements are conducted at equally spaced  $X$ -stations. The first three stations are located upstream from the UAC leading edge ( $X=182 \text{ mm}$ ). The disturbance spectra are shown in Fig. III.28a and Fig. III.28b for the solid and porous sides, respectively. To illustrate development of natural disturbances, their amplitudes versus  $f$  and  $\text{Re}_{eX}$  are shown by contour (Fig. III.31) and surface (Fig. III.32) plots.

At the three upstream stations, the spectra are similar on the solid and porous surfaces, as shown in Fig. III.29. Downstream from the UAC leading edge, the spectrum behaviors are quite different:

- **On the solid side**, the disturbance spectra look very similar to those measured by Stetson & Kimmel (1992a) on a sharp cone at  $M_\infty=6$ ; they correspond to the second-mode instability. At the first upstream station, the second mode is observed at the frequency  $f \approx 430\text{-}450 \text{ kHz}$ . Its amplitude quickly increases downstream, whereas its central frequency decreases to  $270 \text{ kHz}$  at the last station. In the middle of the measurement region ( $\text{Re}_{eX} \geq 3,42 \cdot 10^6$ ) the second mode disturbances become larger than the first-mode disturbances associated with the frequency

band 50-200 kHz; i.e., the first mode grows slower than the second mode. Measurements at the last downstream station (on both solid and porous sides) indicate the beginning of boundary-layer turbulization.

- **On the UAC side**, the second mode grows quickly in the first three stations (upstream of the UAC). Then, this growth is slowed down on the porous coating. Over the entire measurement region, the second-mode amplitudes are smaller than the first-mode ones. Amplifications of the first-mode disturbances are about the same on both solid and porous surfaces.

To determine amplifications of natural disturbances by the boundary layer, the spectra measured in the boundary layer should be referenced to the spectra of external disturbances in free stream. However, the level of high-frequency ( $>100$  kHz) freestream disturbances is very low at hypersonic speeds (lower than the hot-wire anemometer noise level). Therefore, measurements of these disturbances are not feasible. For this reason, disturbance spectra are referenced to the initial spectra measured in the boundary layer at the first station. The initial spectra are shown in Fig. III.30 for the solid (line 1) and porous (line 2) sides. Since these spectra are close to each other, we use for scaling one initial spectrum (line 3), which is determined by averaging of the spectra 1 and 2. To diminish effects of random fluctuations, the initial spectrum  $A_0$  is smoothed by polynomial using the least squares technique (line 4).

The disturbance spectra  $A/A_0$  (normalized by the initial spectrum) are shown in Fig. III.33a and Fig. III.33b for the solid and porous sides, respectively. The normalized amplitudes versus  $f$  and  $Re_{ex}$  are also shown by contour (Fig. III.34) and surface (Fig. III.35) plots. It is clearly seen that natural disturbances amplify in a wide frequency band (30-450 kHz) on both solid and porous sides:

- **The first-mode disturbances** have nearly equal growth on the both sides. Maximum amplifications are observed in the range 100-130 kHz; they are 3.3 and 3.6 for solid and porous sides, respectively.
- **The second-mode disturbances** amplify essentially stronger than the first-mode disturbances. Their maximum amplifications are 6.9 and 20.4 on the porous and solid sides, respectively.

Comparing these data we conclude that *the UAC of regular structure stabilizes the second mode and weakly affects the first mode under natural flow conditions.*

### 3.3.3. Artificial wave packets

Artificial disturbances were generated in the boundary layer at the frequency 275 kHz. At this frequency the second mode has maximum amplitude in the natural disturbances spectra measured on the solid side.

Fig. III.36 and Fig. III.37 show transversal distributions of the amplitude and phase of wave packets. These distributions are nearly symmetric. They are similar in all cross sections. The amplitude distributions are maximal at the wave-packet center. The phase distributions are very flat. The phase difference between the neighboring stations is approximately 80 rad. Fig. III.38 shows the amplitude wave spectra with respect to the transversal wave number  $\beta$ . These data are obtained using the discrete Fourier transform of the transversal distributions shown in Fig. III.36 and Fig. III.37. The whole wave packet lies within the range of  $\beta = \pm 0.5$  rad/degree, which approximately corresponds to the range of the wave-vector inclination angle of  $\pm 20^\circ$ . The

amplitude maximums are observed at  $\beta=0$ . Dimensionless phase speeds  $C_x \equiv C_x^*/U_e^*$  are shown in Fig. III.38. They weakly depend on the longitudinal coordinate  $X$  and practically coincide on the porous and solid surfaces. These features indicate that the wave packets predominantly consist of the second mode disturbances.

Amplitudes of natural and artificial disturbances on the solid and porous sides are shown in Fig. III.39. The disturbance frequency is 275 kHz. On the porous side, the amplitudes of artificial and natural disturbances practically coincide. Therefore the natural disturbances at this frequency are predominantly two-dimensional waves of the second mode. It is clearly seen that *the UAC leads to substantial decreasing of the amplitude growth: the maximum amplitude is approximately 3 times lower than in the case of solid wall.*

### 3.4. Comparison with linear stability theory

Stability calculations are conducted for two-dimensional disturbances ( $\beta = 0$ ) of the second mode at the flow parameters relevant to the experimental data shown in Fig. III.39. Namely: the local Mach number is  $M_e = 5.325$ ; the stagnation temperature is  $T_0 = 390$  K; the wall temperature is  $T_w = 320$  K that corresponds to the wall temperature ratio  $T_w/T_e = 5.471$ ; the local unit Reynolds number is  $Re_{e1} = 15.2 \times 10^6 \text{ m}^{-1}$ ; the disturbance frequency  $f = 275$  kHz that corresponds to the frequency parameter  $F = 1.3926 \times 10^{-1}$ . The fluid is a perfect gas of  $\gamma = 1.4$  and  $Pr = 0.708$ . The viscosity-temperature dependency is approximated by Sutherland's formula (1.7); the second viscosity is  $\mu_2^* = 0.8\mu^*$ . The spatial growth rate is calculated using the relation (1.30); the nonparallel effects are included as described in Section 1.1.2.

For the porous wall, stability calculations are performed using the boundary conditions (1.46)-(1.48), in which the characteristic impedance and the propagation constant are given by (1.49)-(1.52); i.e., the rarefaction effects are taken into account. The UAC parameters are specified as: the pore radius  $r_0^* = 25 \text{ }\mu\text{m}$ , the pore spacing  $s^* = 100 \text{ }\mu\text{m}$ , the porosity  $\phi = 0.2$ , the porous-layer thickness  $h^* = 450 \text{ }\mu\text{m}$ , the UAC leading edge  $X = 182 \text{ mm}$ .

Figure III.40 compares theoretical amplification curves (solid lines) with experimental data (symbols), which are also shown in Fig. III.39. In these calculations, the amplitudes are adjusted to the experimental values at the initial station. The theory agrees well with the experiment on the solid side (compare the black line with black triangles). The amplification curve calculated for the porous surface (red line) passes above the experimental points (red triangles and blue squares); i.e., the theory underestimates the UAC stabilization effect. One of possible reasons of this discrepancy is a conical shape of actual pores. The green line shows the amplification curve calculated for the pore radius averaged over the pore length ( $r_0^* = 28.5 \text{ }\mu\text{m}$ ). With this correction the agreement of theory with experiment is satisfactory. Another reason may be nonlinear effects, which may slow down the second mode amplification. As mentioned in Section 3.3.2, the nonlinear breakdown of natural disturbances seems to occur at the last station. Since the amplitudes of artificially excited wave packets are significantly larger than those of natural disturbances, the nonlinear effect may be exposed earlier. This assumption is consistent with decreasing of the wave-packet amplitude at the last station (see blue squares in Fig. III.40).

As shown in Figure III.41, the theoretical phase speeds agree well with the phase speeds measured for artificially excited wave packets on both solid and porous sides.

### 3.5. Summary

A model of a  $7^\circ$  half-angle sharp cone with the UAC of regular microstructure was manufactured. The cone has a longitudinal half of its surface solid and the other a porous sheet perforated with equally spaced blind cylindrical holes of the average pore diameter  $50\text{ }\mu\text{m}$ , depth  $450\text{ }\mu\text{m}$  and average spacing  $100\text{ }\mu\text{m}$ . The cone was tested in the T-326 hypersonic wind tunnel at freestream Mach number 5.95. Stability measurements in the boundary layer on the porous and solid cone surfaces were conducted using hot-wire anemometry. Spectra of natural and artificially excited wave packets were obtained at various cross sections of the cone. The wave packets were generated by periodic glow discharge of a fixed frequency.

Measurements of mean profiles and RMS mass-flow pulsations showed that the boundary layer was laminar on the solid and porous sides at all cross-sectional stations. The porous coating did not affect the mean flow and RMS pulsations; i.e., the UAC roughness did not cause premature tripping of the boundary layer.

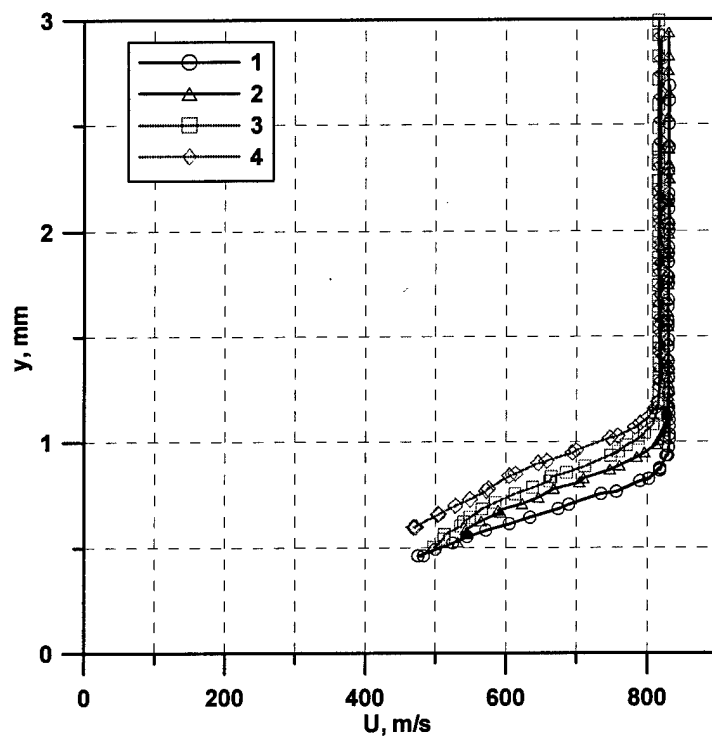
Under natural conditions, the first (low frequency) and second (high frequency) modes were observed in the boundary layer. Analysis of the natural-disturbance spectra showed that the second mode was a dominant instability on the solid side. The UAC stabilizes the second mode and weakly affects the first mode that is consistent with the theoretical predictions.

To evaluate the UAC stabilization effect, the wave packet was artificially excited at the frequency 275 kHz relevant to the second-mode instability. It was found that the two-dimensional wave is a dominant component of the wave packet. The amplification of this component practically coincides with the amplification of natural disturbance of the same frequency. This confirms that natural disturbances of the high-frequency band are predominantly two-dimensional waves relevant to the second-mode instability. It was shown that the UAC leads to substantial decreasing of the wave-packet growth: the maximum amplitude on the porous side is approximately 3 times lower than that on the solid side.

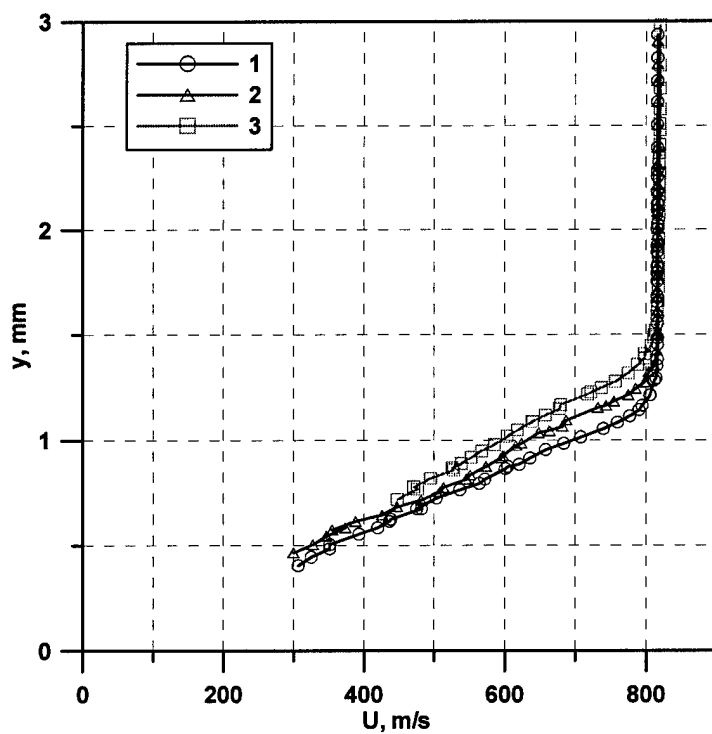
Stability calculations were conducted for the second-mode two-dimensional wave of frequency 275 kHz and compared with experimental data. The theoretical amplification curve agrees well with the experiment on the solid side. The amplification curve calculated for the porous surface passes above the experimental points; i.e., the theory underestimates the UAC stabilization effect. With the correction accounting for conical shape of actual pores, the agreement is satisfactory. It is assumed that the discrepancy between theory and experiment in the downstream measurement station is due to nonlinear effects.

In summary, the LST model discussed in Chapter II satisfactorily predicts the UAC stabilization effect and can be used for evaluations of the UAC performance in connection with hypersonic laminar flow control.



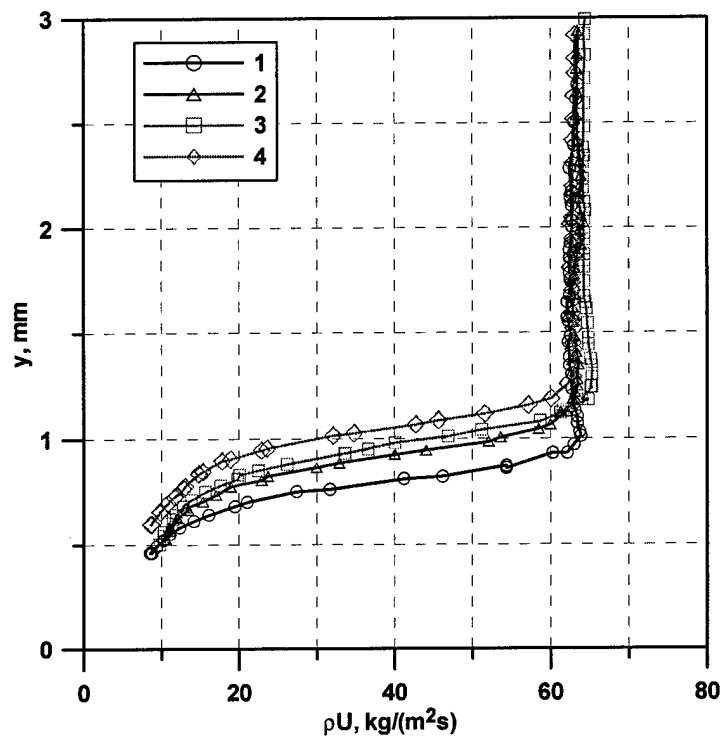


Symbols 1-4 correspond to  $X=146.68, 195.14, 209.33$  and  $244.65$  mm.

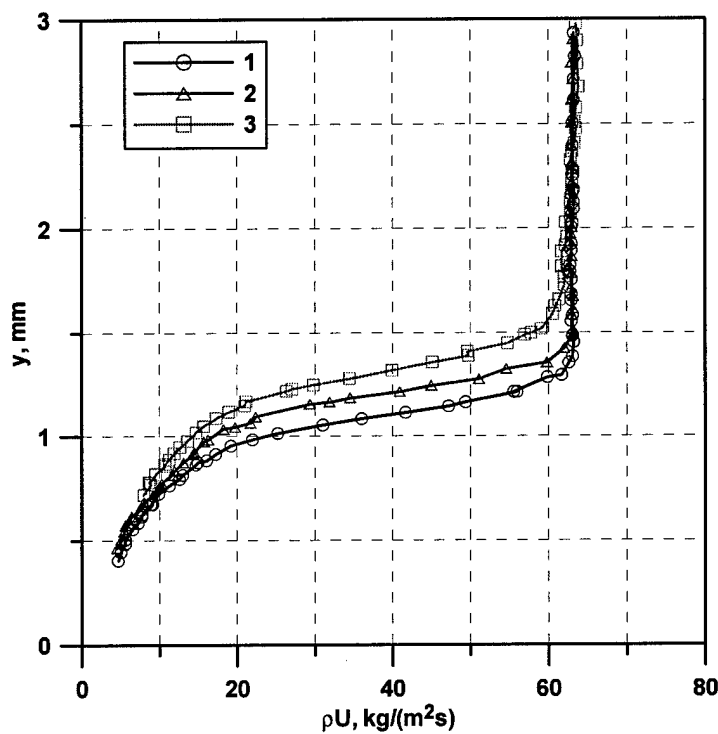


Symbols 1-3 correspond to  $X=271.72, 297.07, 322.4$  mm

Fig. III.15 The mean-flow velocity profiles in the boundary layer on the solid side.

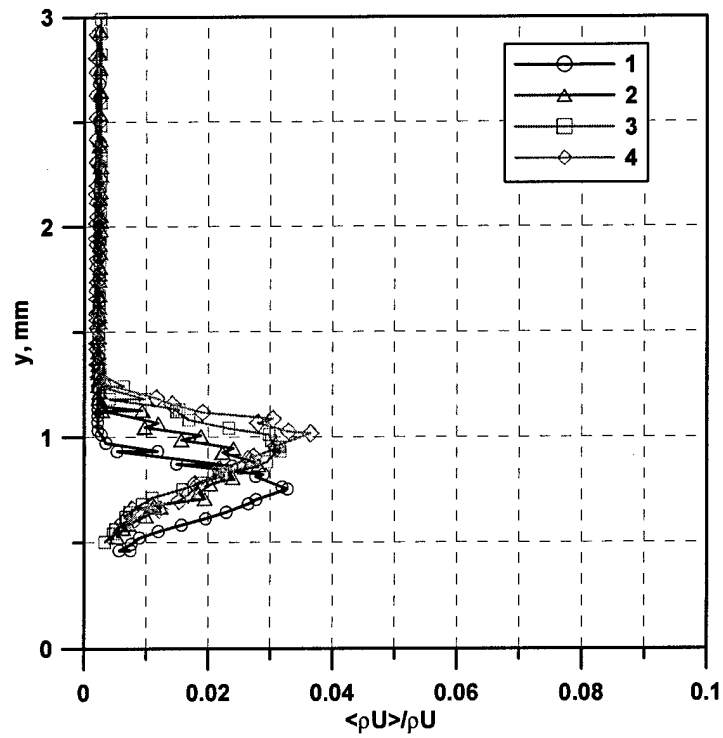


Symbols 1-4 correspond to  $X=146.68, 195.14, 209.33$  and  $244.65$  mm

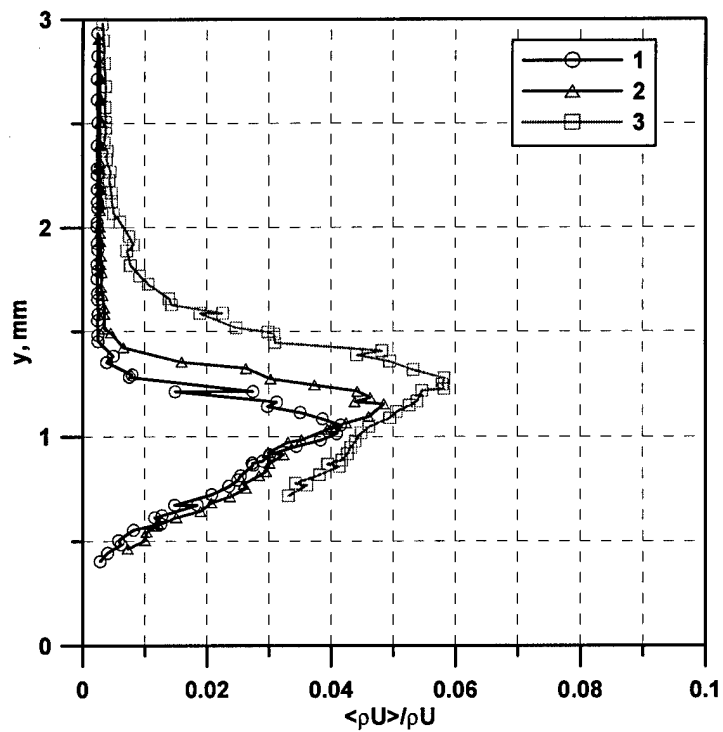


Symbols 1-3 correspond to  $X=271.72, 297.07, 322.4$  mm

Fig. III.16 The profiles of  $\rho U$  in the boundary layer on the solid side.

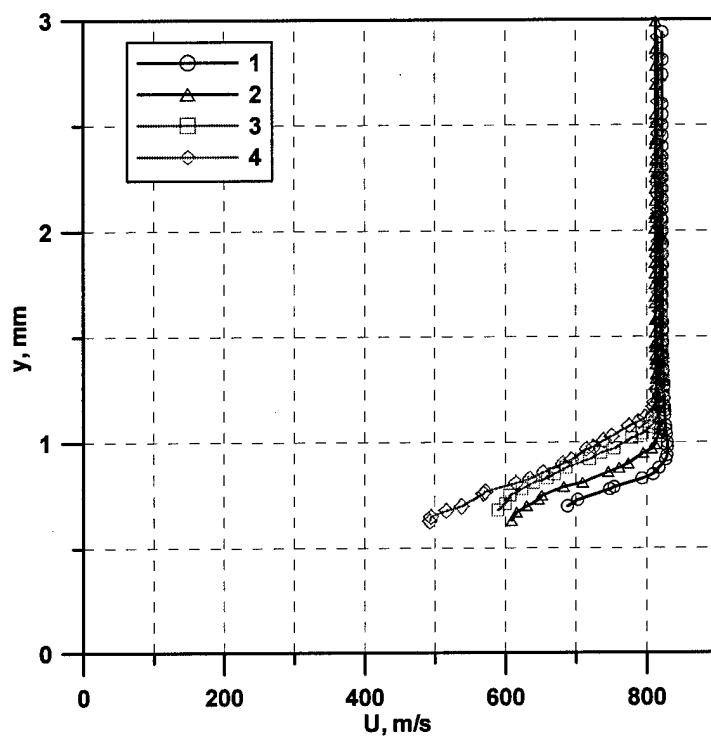


Symbols 1-4 correspond to  $X=146.68, 195.14, 209.33$  and  $244.65$  mm.

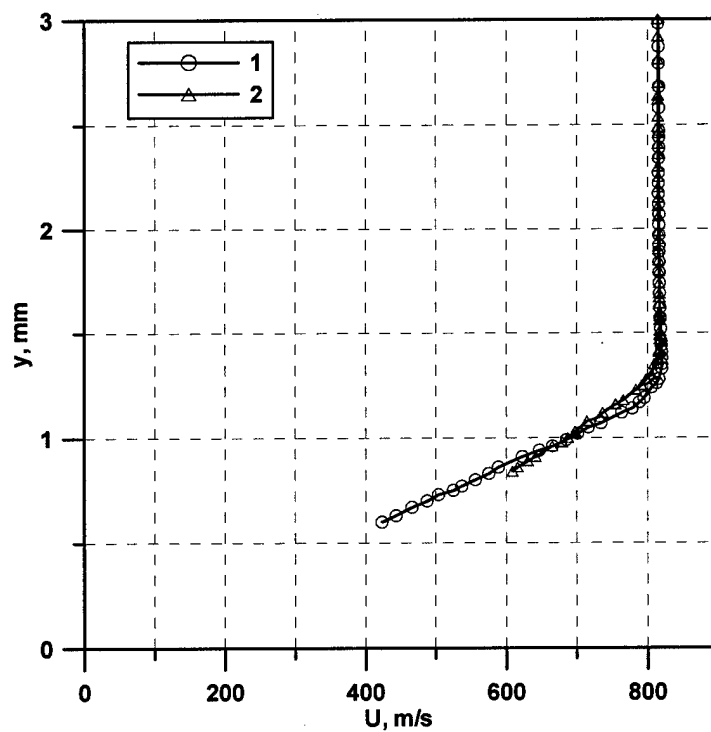


Symbols 1-3 correspond to  $X=271.72, 297.07, 322.4$  mm

Fig. III.17 The RMS pulsations profiles on the solid side.

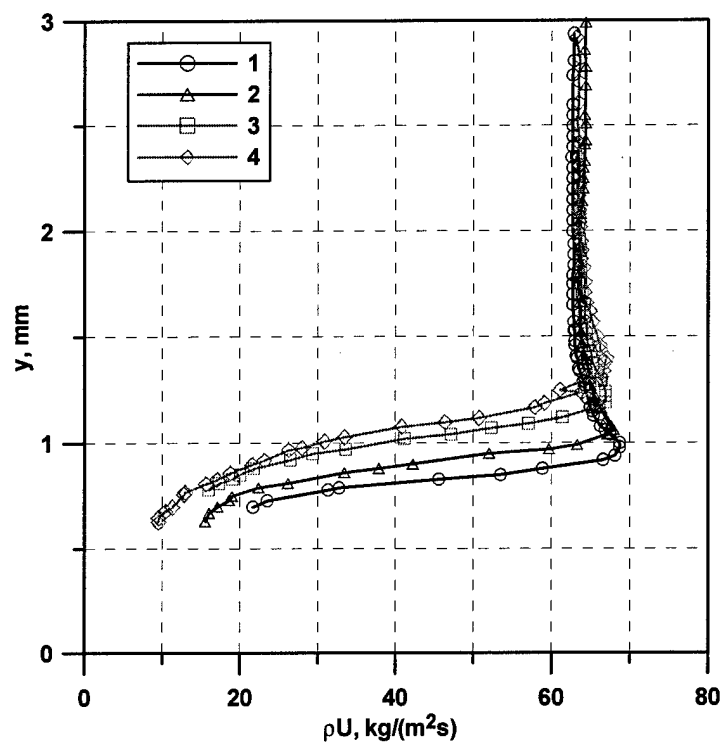


Symbols 1-4 correspond to  $X=145.56, 180.68, 215.7$  and  $251.12$  mm.

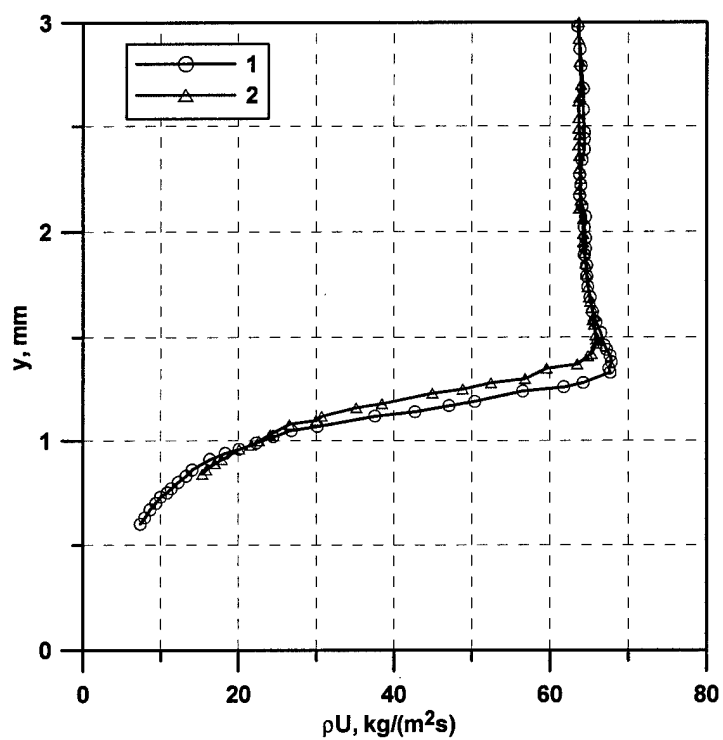


Symbols 1-2 correspond to  $X=287.2, 321.75$  mm

Fig. III.18 The mean flow velocity profiles in the boundary layer on the porous side.

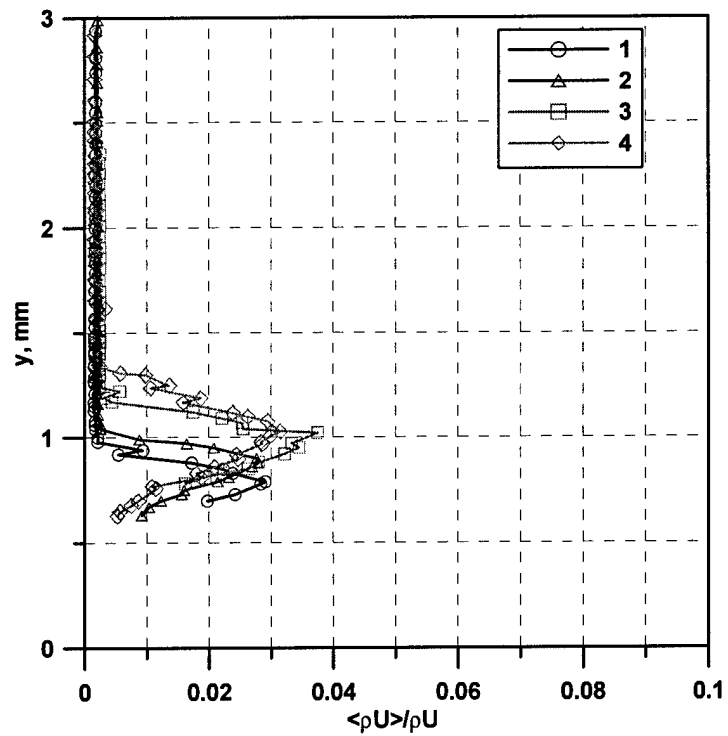


Symbols 1-4 correspond to  $X=145.56, 180.68, 215.7$  and  $251.12$  mm

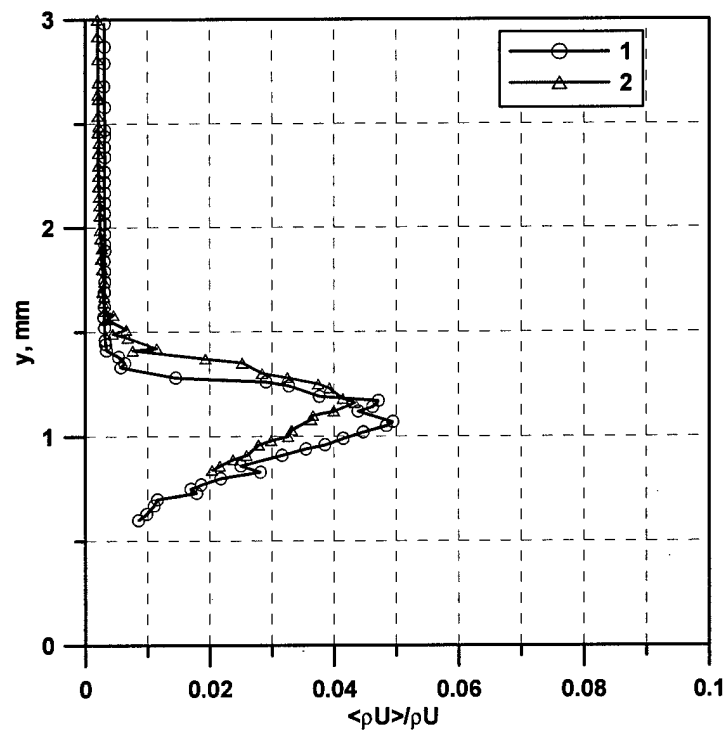


Symbols 1-2 correspond to  $X=287.2, 321.75$  mm

Fig. III.19 The profiles of  $\rho U$  in the boundary layer on the porous side.

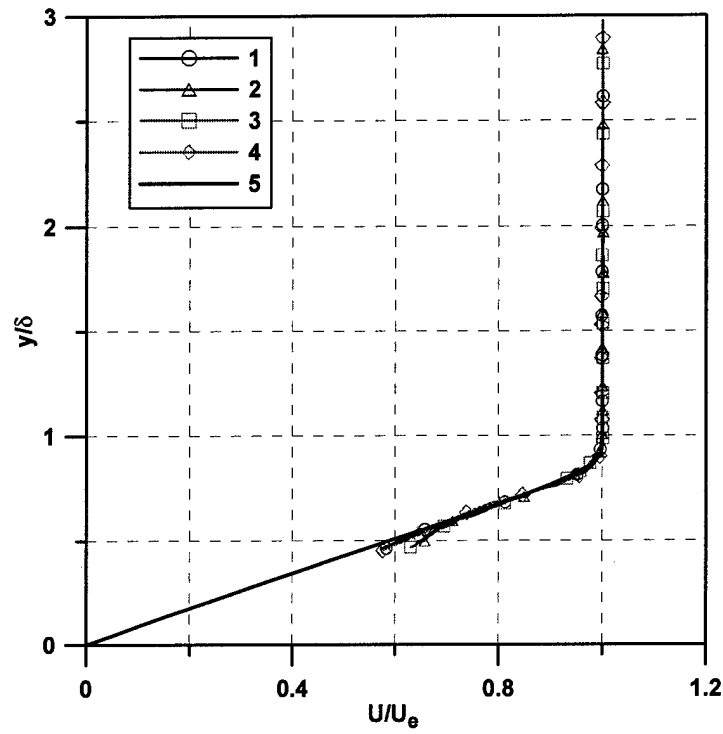


Symbols 1-4 correspond to  $X=145.56, 180.68, 215.7$  and  $251.12$  mm

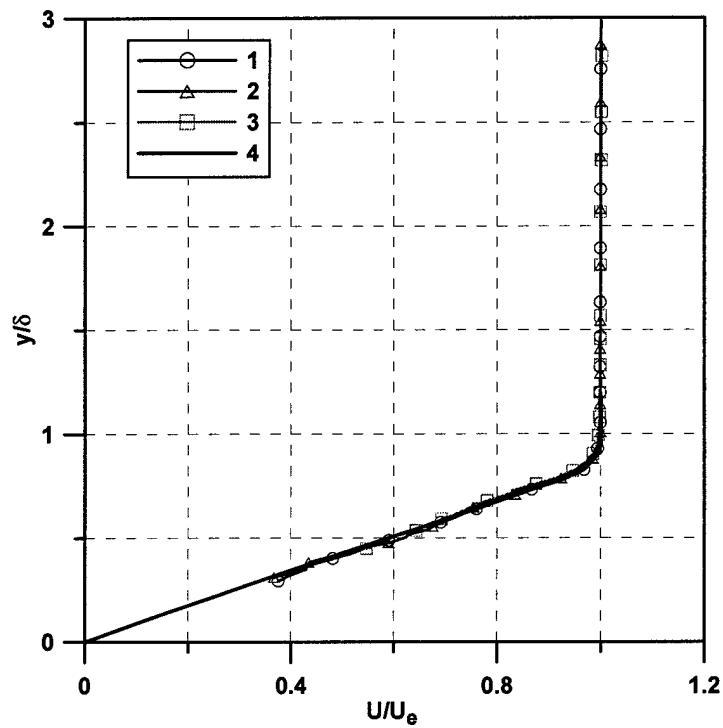


Symbols 1-2 correspond to  $X=287.2, 321.75$  mm

Fig. III.20 RMS pulsations profiles in the boundary layer on the porous side.

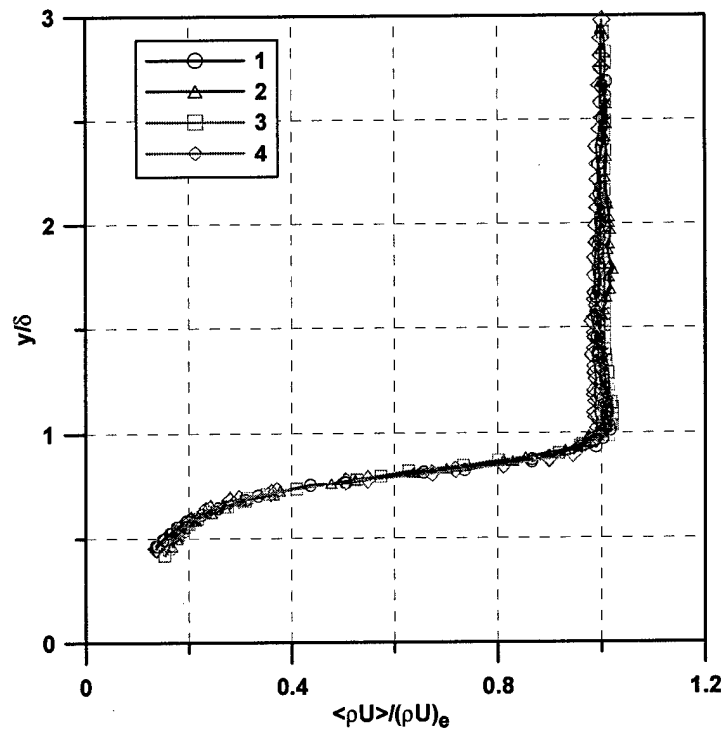


Symbols 1-4 correspond to  $Re_{ex} \Sigma 0^{-6} = 2.18, 2.91, 3.30$  and  $3.79$

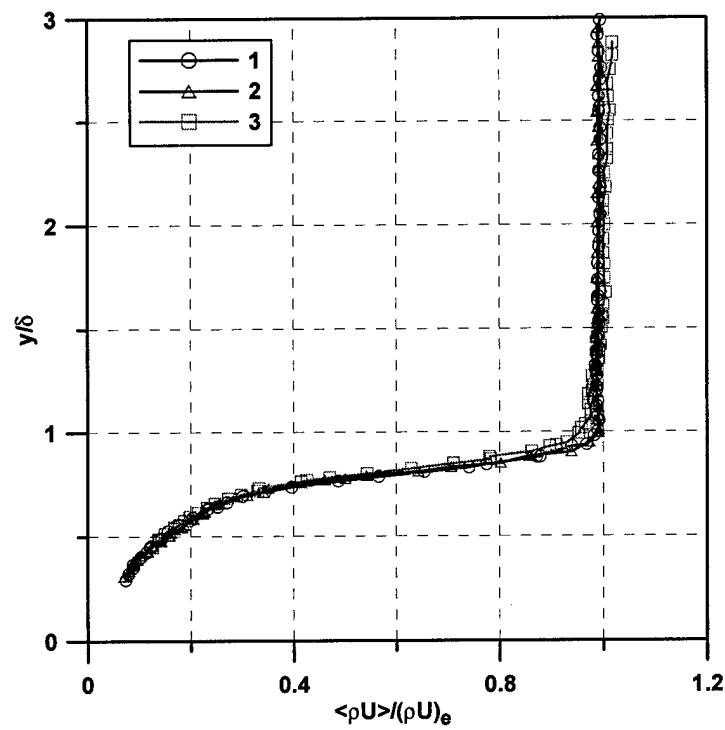


Symbols 1-3 correspond to  $Re_{ex} \Sigma 0^{-6} = 4.23, 4.62, 4.97$

Fig. III.21 Normalized profiles of  $U$  on the solid side.



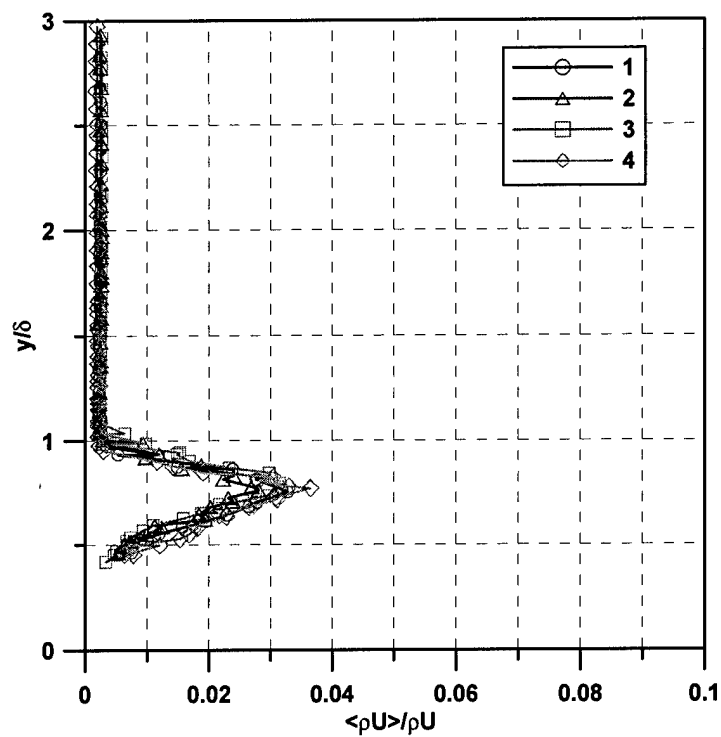
Symbols 1-4 correspond to  $Re_{eX} \Sigma 0^{-6} = 2.18, 2.91, 3.30$  and  $3.79$



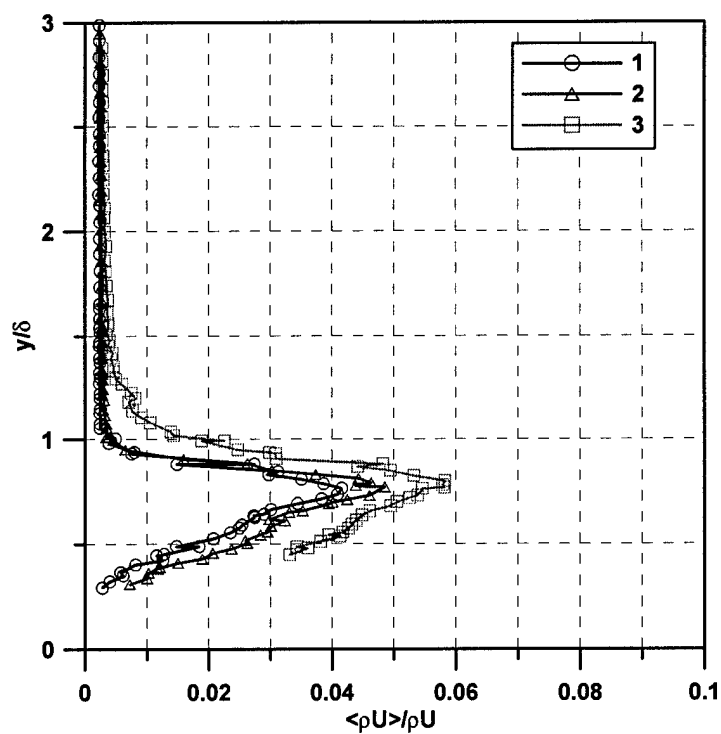
Symbols 1-3 correspond to  $Re_{eX} \Sigma 0^{-6} = 4.23, 4.62, 4.97$

Fig. III.22 Normalized profiles of  $\rho U$  on the solid side.



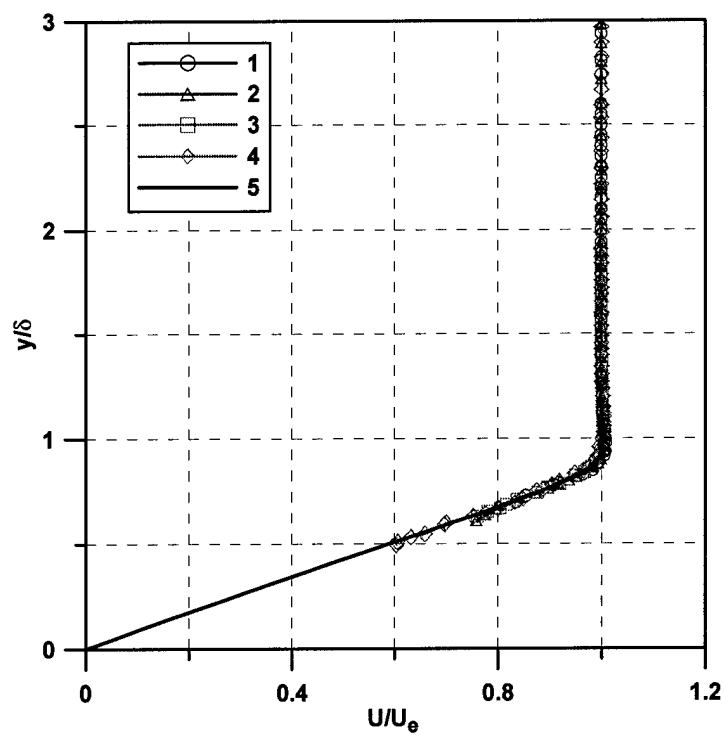


Symbols 1-4 correspond to  $Re_{ex} \Sigma 0^{-6} = 2.18, 2.91, 3.30$  and  $3.79$

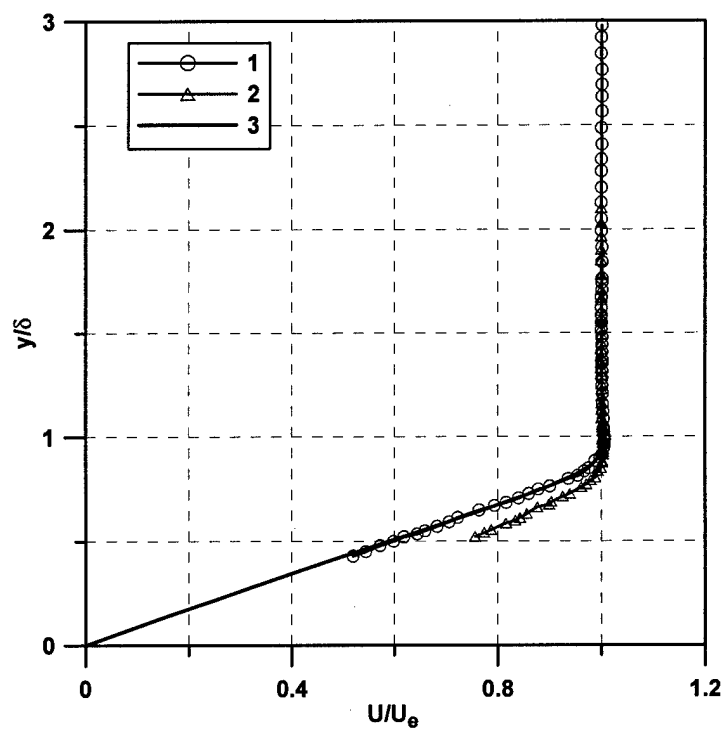


Symbols 1-3 correspond to  $Re_{ex} \Sigma 0^{-6} = 4.23, 4.62, 4.97$

Fig. III.23 Normalized RMS pulsations profiles on the solid side.

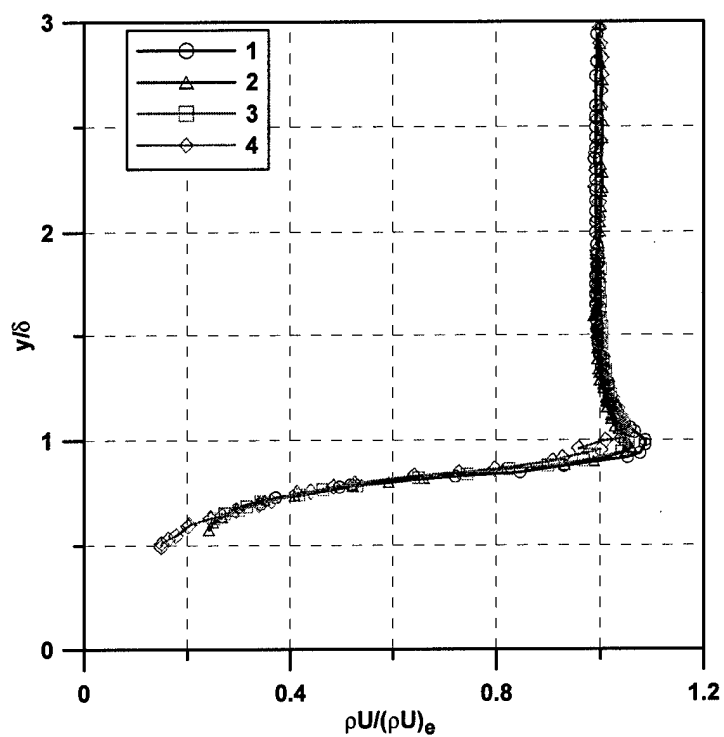


Symbols 1-4 correspond to  $Re_e X 10^{-6} = 2.22, 2.81, 3.35$  and  $3.91$

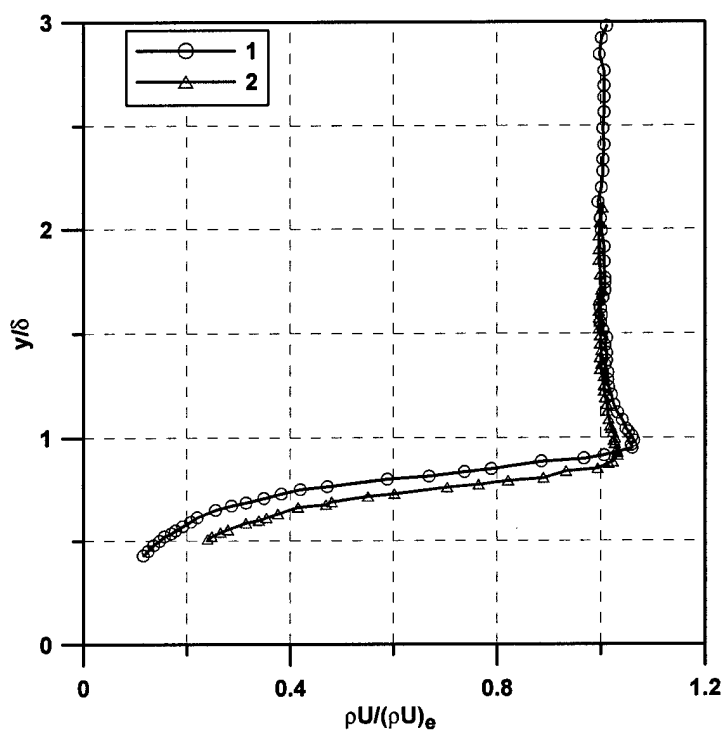


Symbols 1-2 correspond to  $Re_e X 10^{-6} = 4.50, 5.05$

Fig. III.24 Normalized profiles of  $U$  on the porous side.

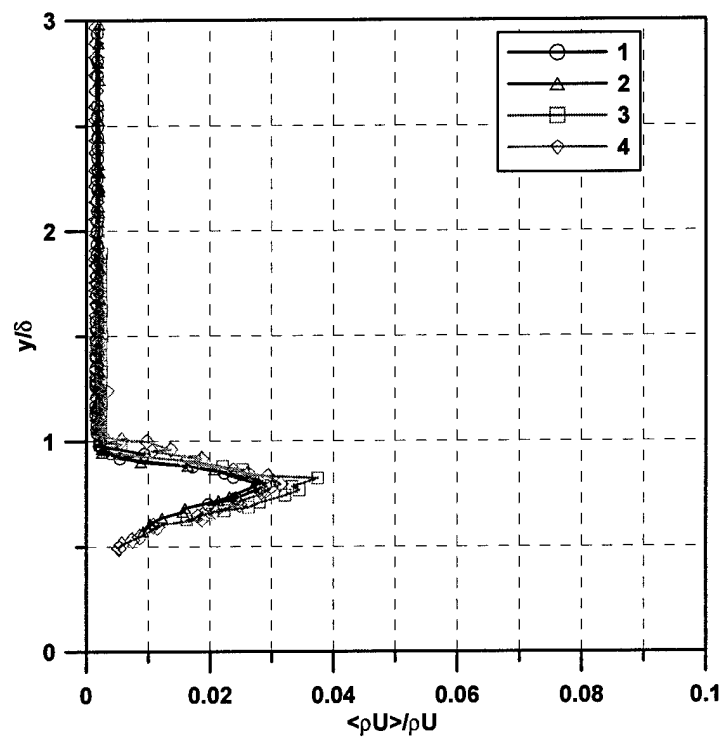


Symbols 1-4 correspond to  $Re_{cX}\Sigma 0^{-6} = 2.22, 2.81, 3.35$  and  $3.91$

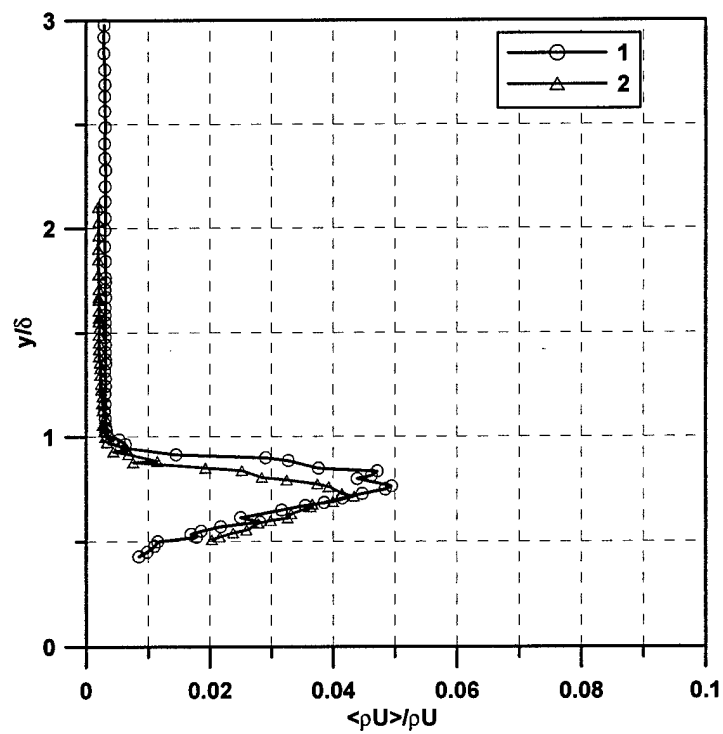


Symbols 1-2 correspond to  $Re_{cX}\Sigma 0^{-6} = 4.50, 5.05$

Fig. III.25 Normalized profiles of  $\rho U$  on the porous side.



Symbols 1-4 correspond to  $Re_{ex} \Sigma 0^{-6} = 2.22, 2.81, 3.35$  and  $3.91$



Symbols 1-2 correspond to  $Re_{ex} \Sigma 0^{-6} = 4.50, 5.05$

Fig. III.26 Normalized RMS pulsations profiles on the porous side.

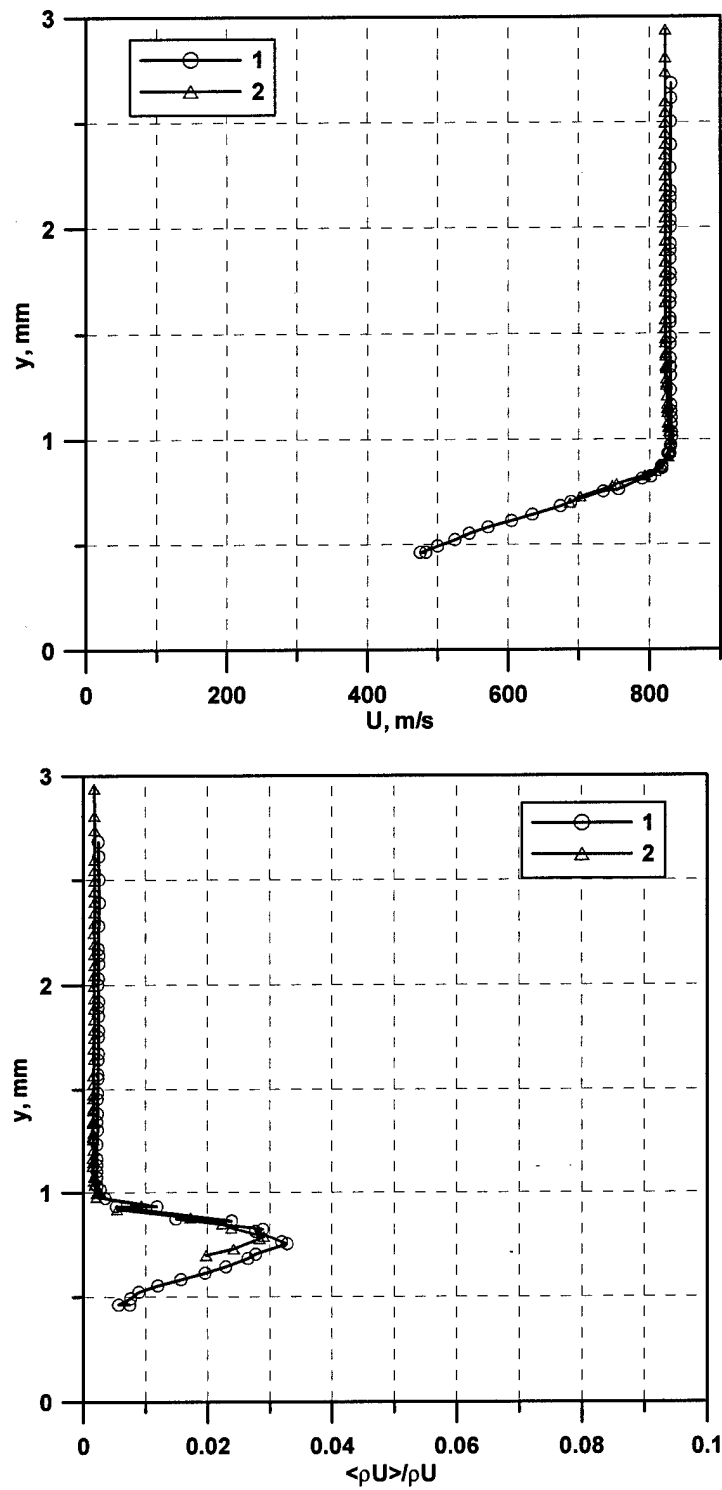


Fig. III.27 Comparison of  $U$  and  $\langle \rho U \rangle / \rho U$  distributions on the solid side (1  $\Re_{ex}=2.18 \cdot 10^{-6}$ ) and on the porous side (2  $\Re_{ex}=2.22 \cdot 10^{-6}$ ).

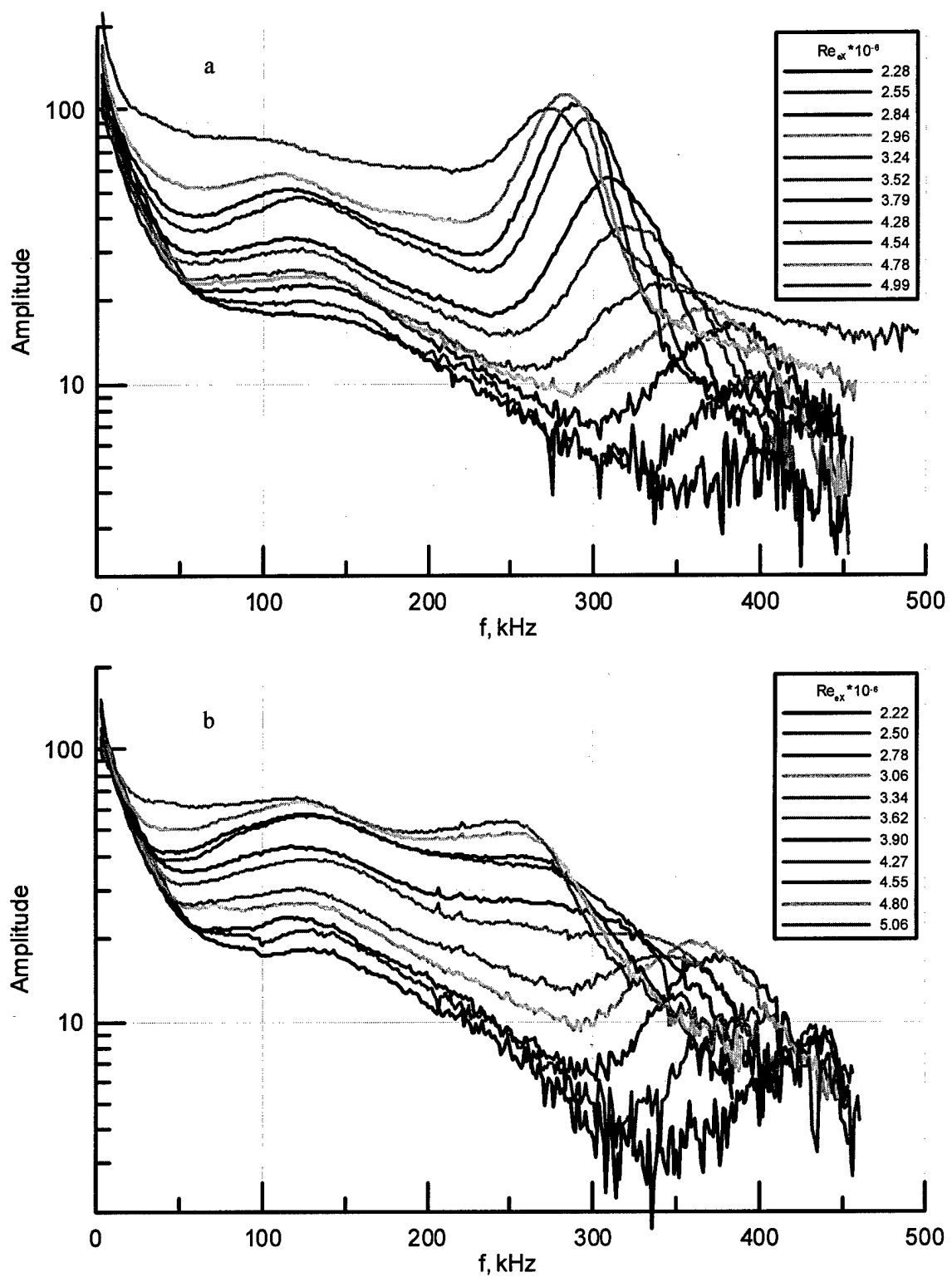


Fig. III.28 Natural disturbances spectra in the boundary layer on the solid (a) and porous (b) surfaces.

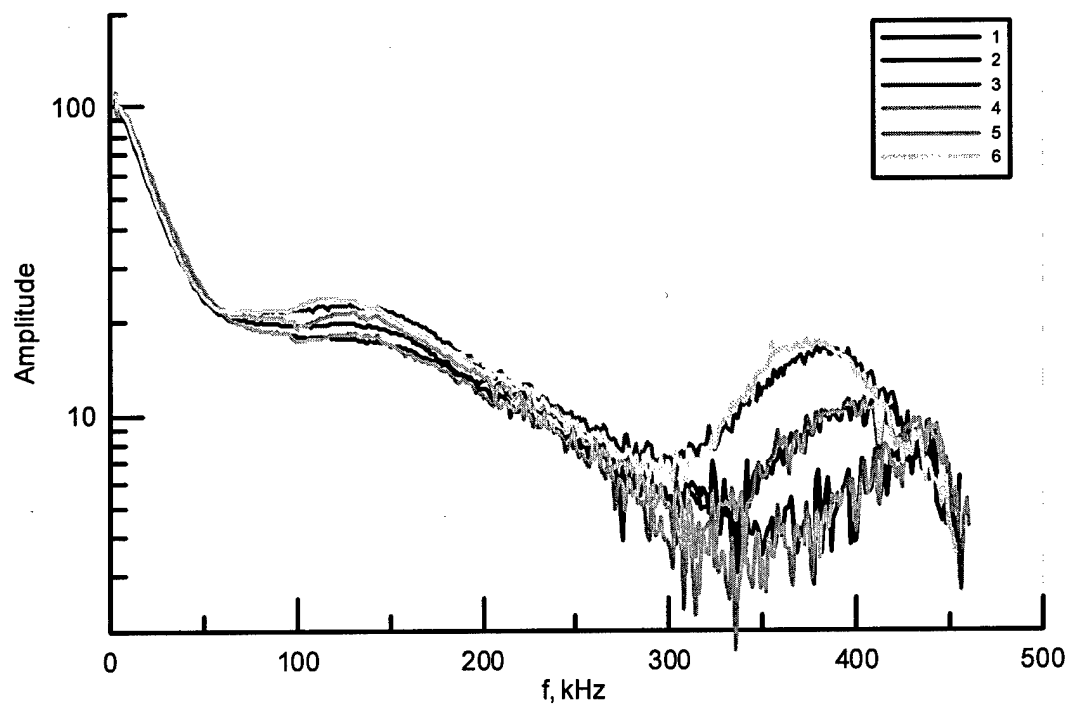


Fig. III.29 Comparison of spectra measured upstream from UAC; 1 ñ 3 ñ solid side,  $Re_{ex} \cdot 10^{-6} = 2.28, 2.55, 2.84$ ; 4 ñ 6 ñ side with UAC,  $Re_{ex} \cdot 10^{-6} = 2.22, 2.50, 2.78$ .

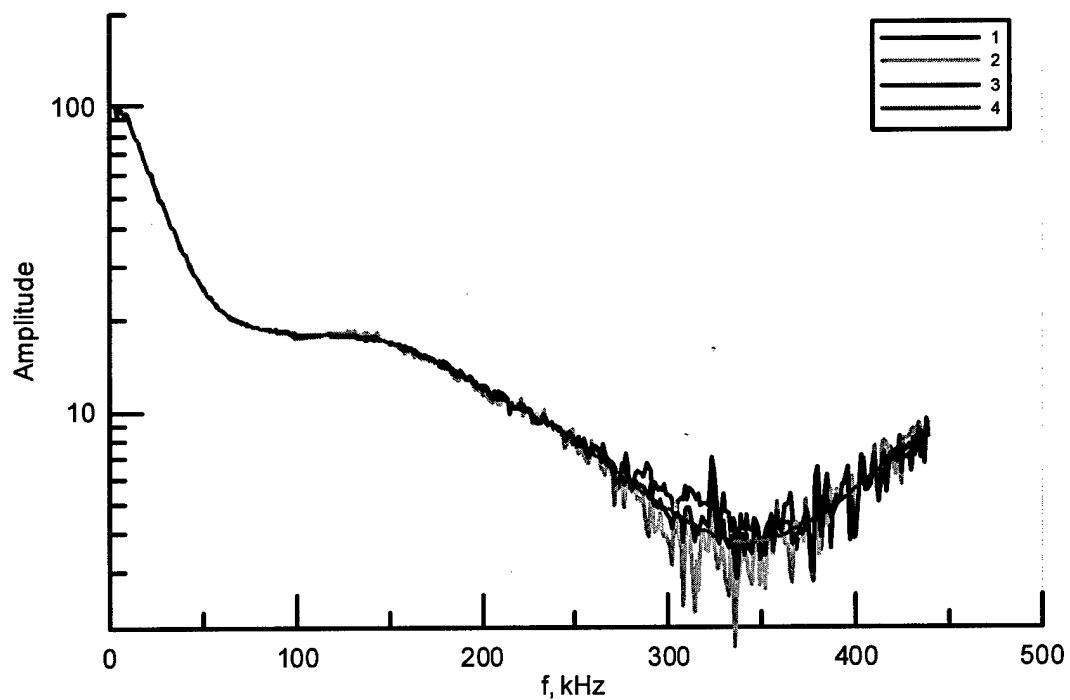
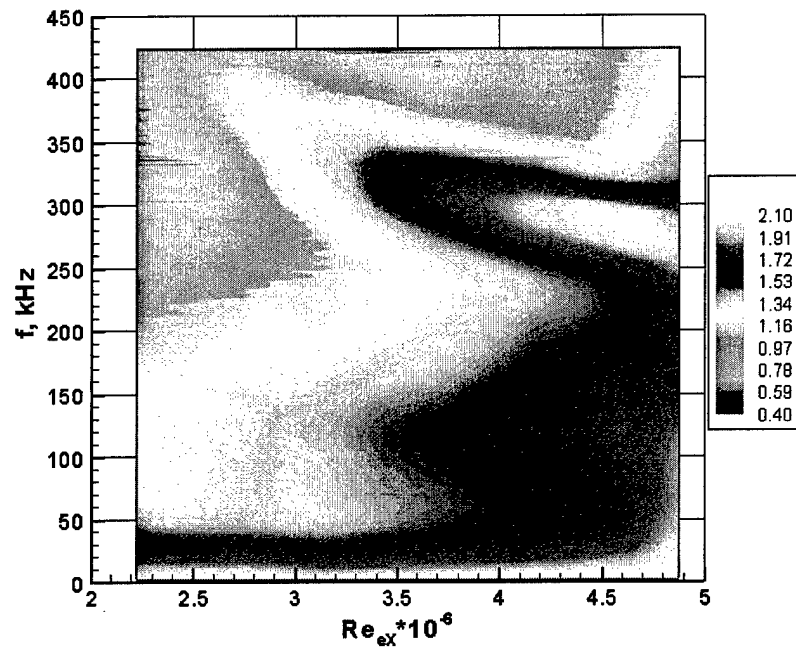


Fig. III.30 The initial spectra.

1 ñ solid side ( $Re_{ex} \cdot 10^{-6} = 2.28$ ); 2 ñ side with UAC ( $Re_{ex} \cdot 10^{-6} = 2.22$ ); 3 ñ average spectrum; 4 - smoothed average spectrum.

a



b

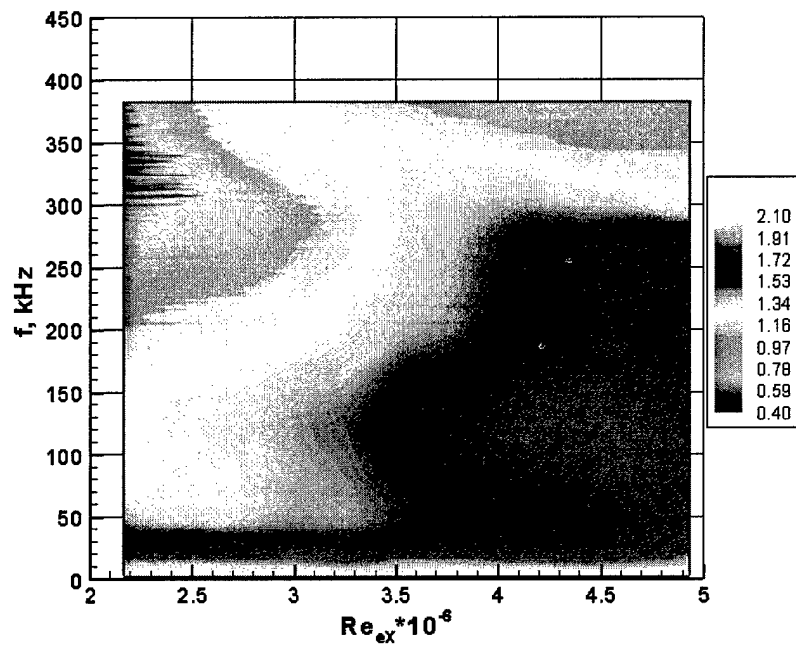


Fig. III.31 Contour plot of natural-disturbance spectra for solid (a) and porous (b) surfaces.



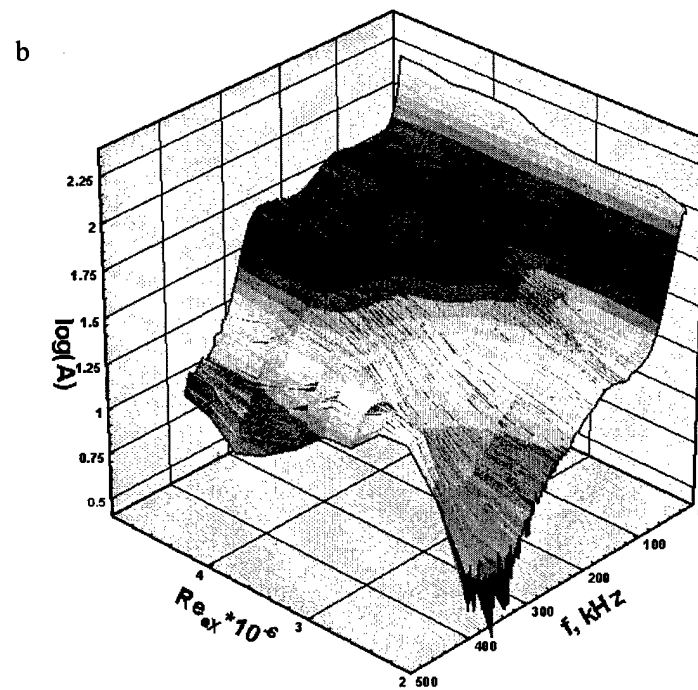
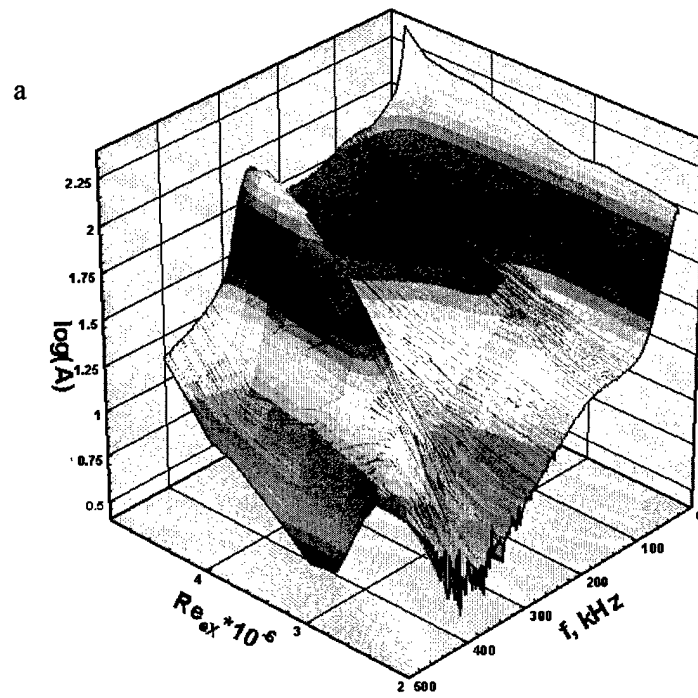


Fig. III.32 Surface plot of natural-disturbance spectra for solid (a) and porous (b) surfaces.

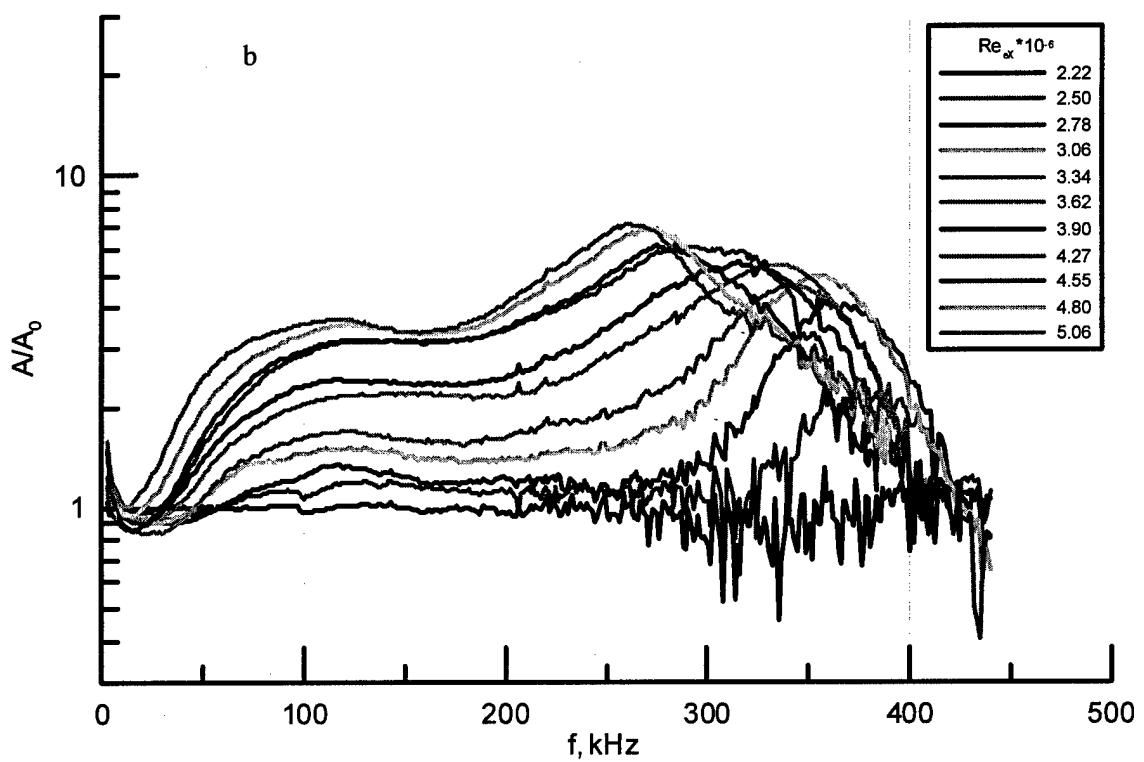
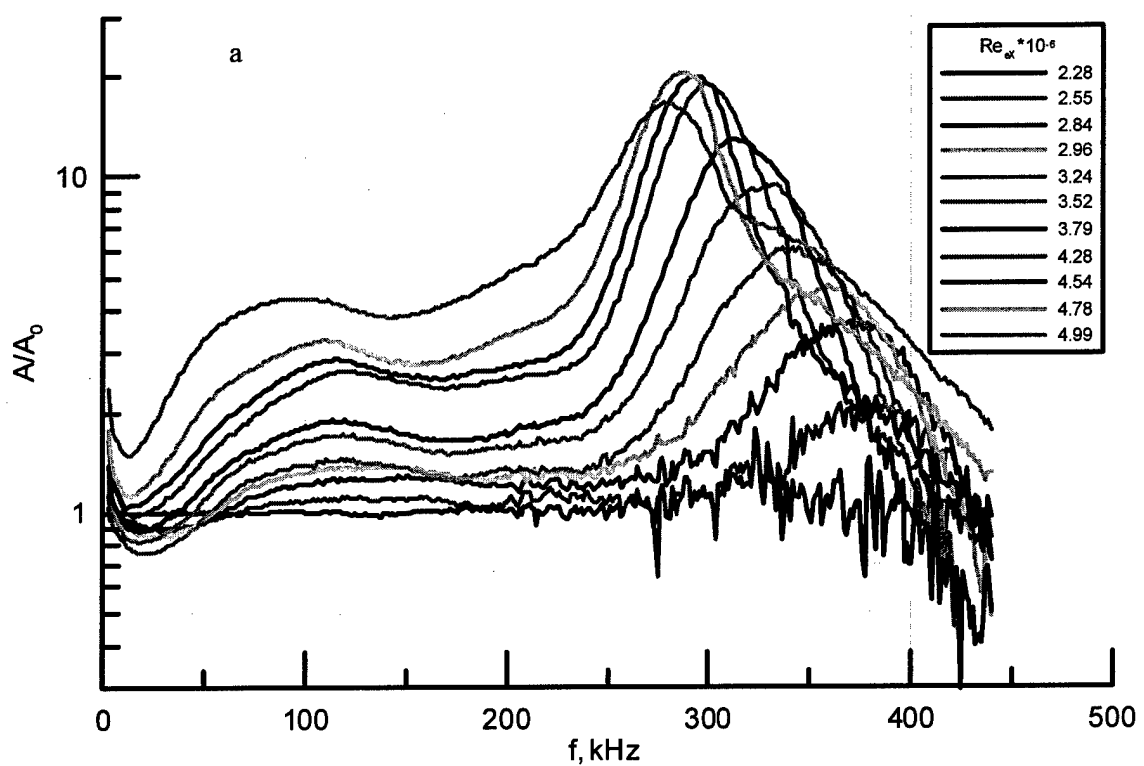


Fig. III.33 Normalized natural-disturbance spectra for solid (a) and porous (b) surfaces.

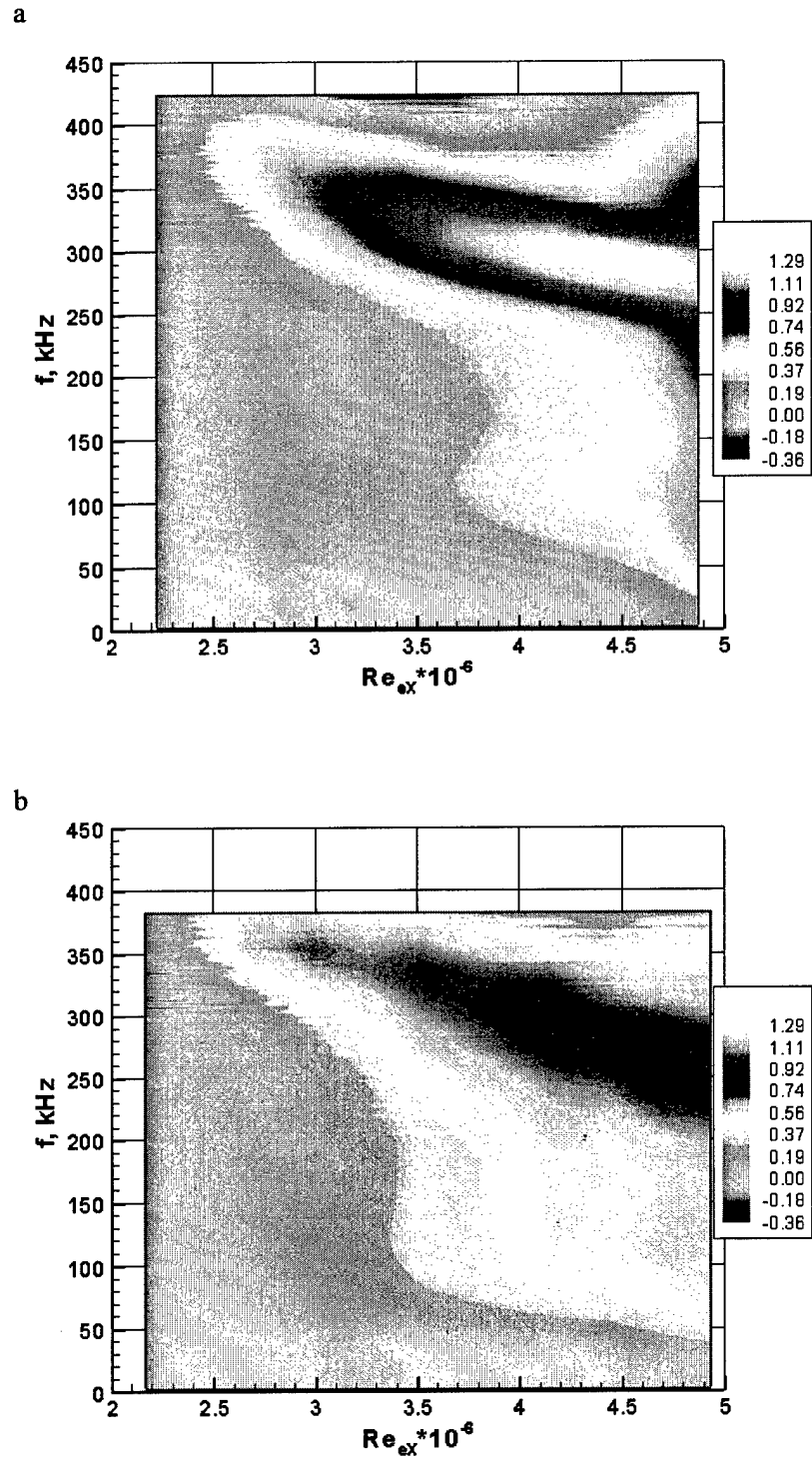


Fig. III.34 Contour plot of normalized natural-disturbance spectra for solid (a) and porous (b) surfaces.

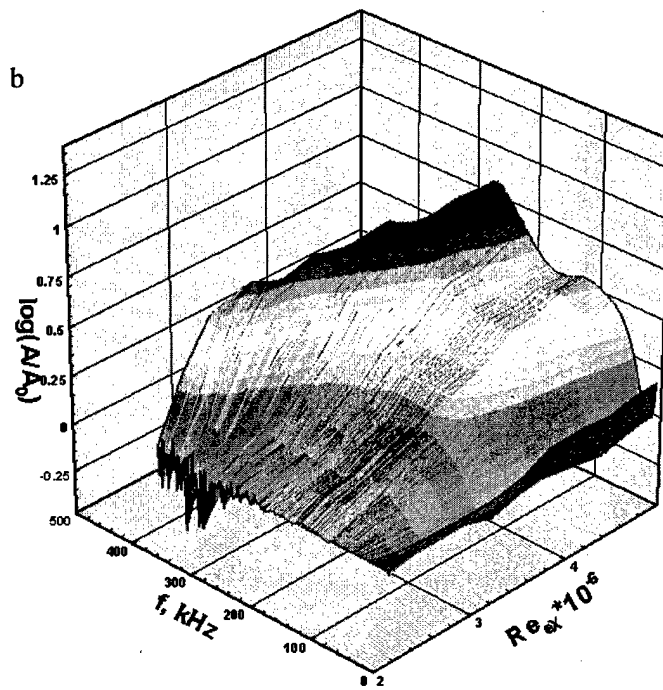
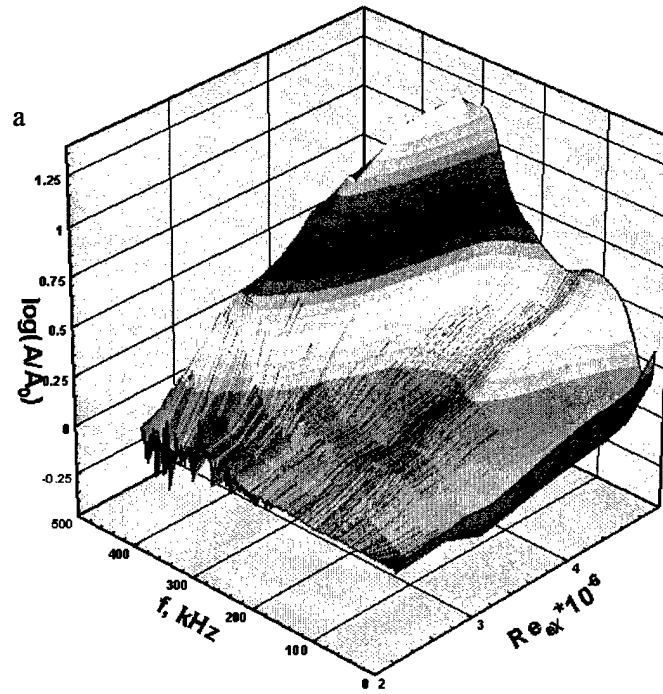


Fig. III.35 Surface plot of normalized natural-disturbance spectra for solid (a) and porous (b) surfaces.

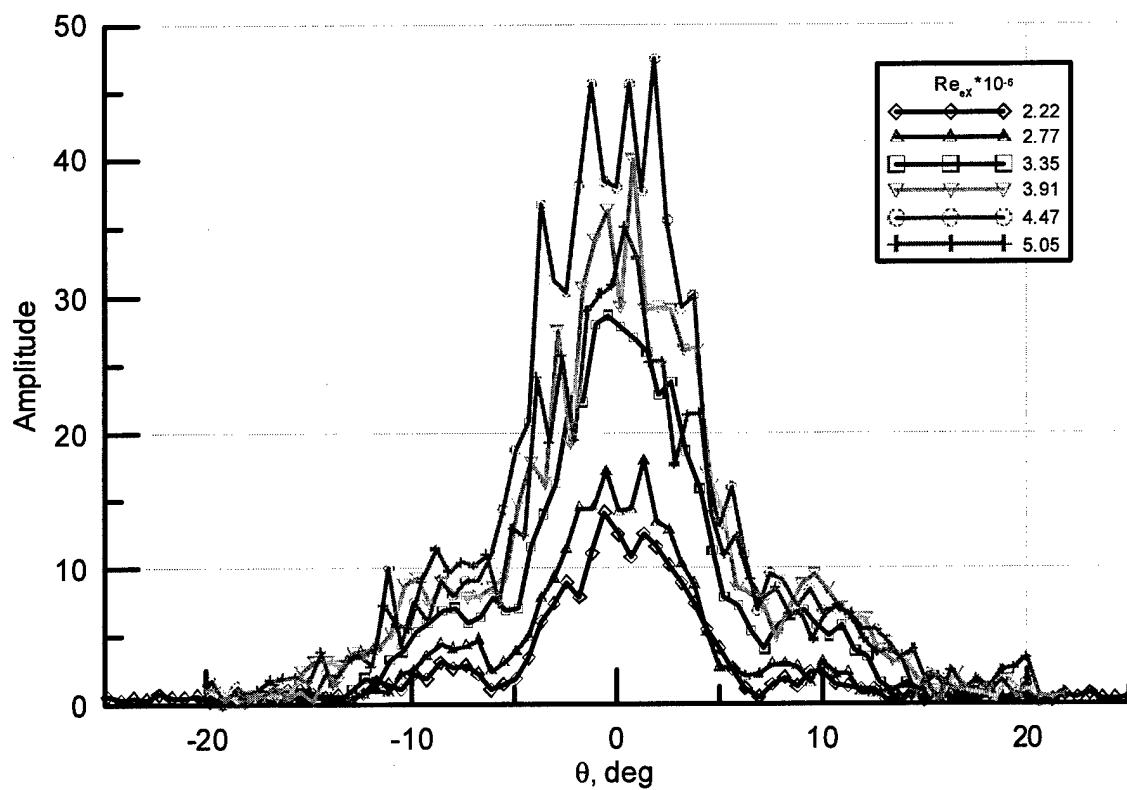


Fig. III.36 Transversal distributions of the artificial wave-packet amplitude on the porous side.

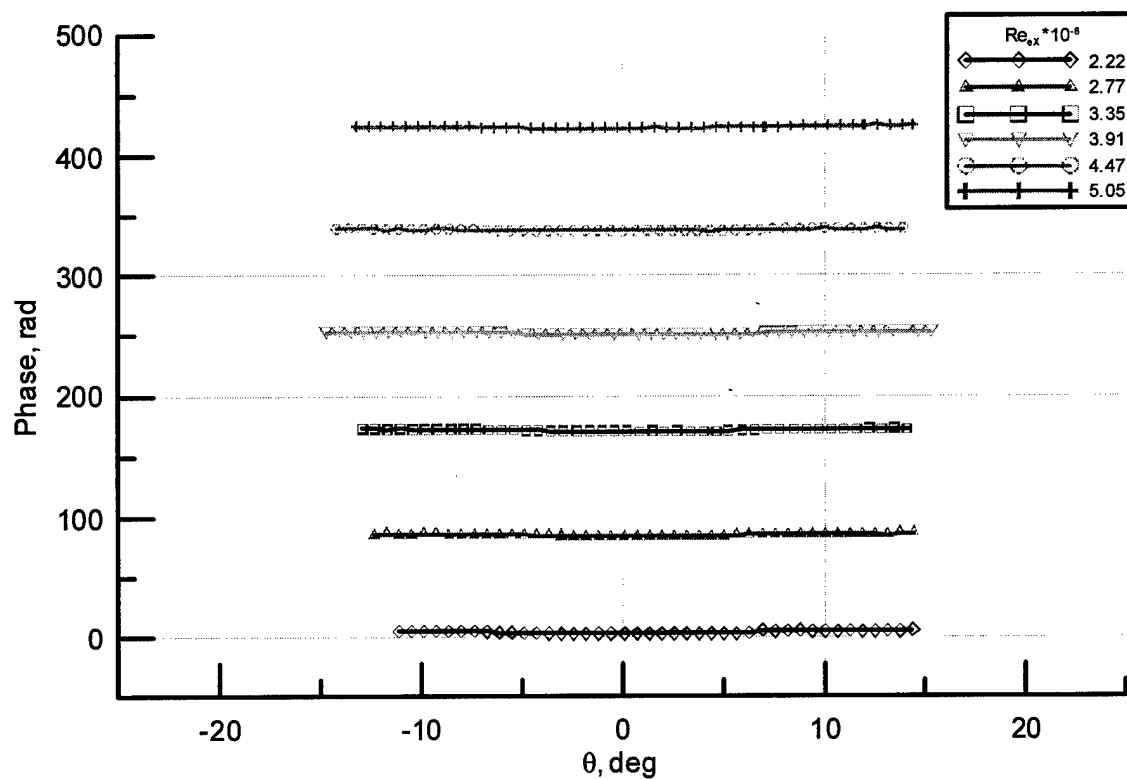


Fig. III.37 Transversal distributions of the artificial wave-packet phase on the porous side.

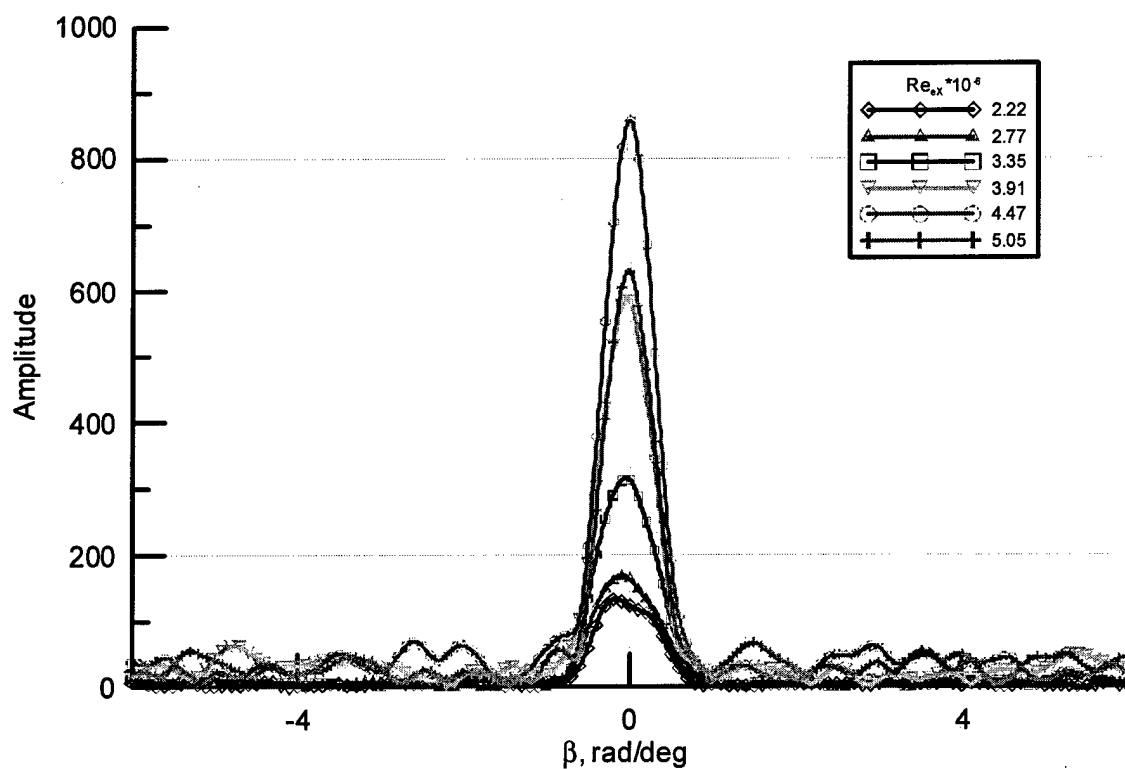


Fig. III.38 Amplitude wave spectra with respect to the transversal wavenumber  $\beta$  for porous side.

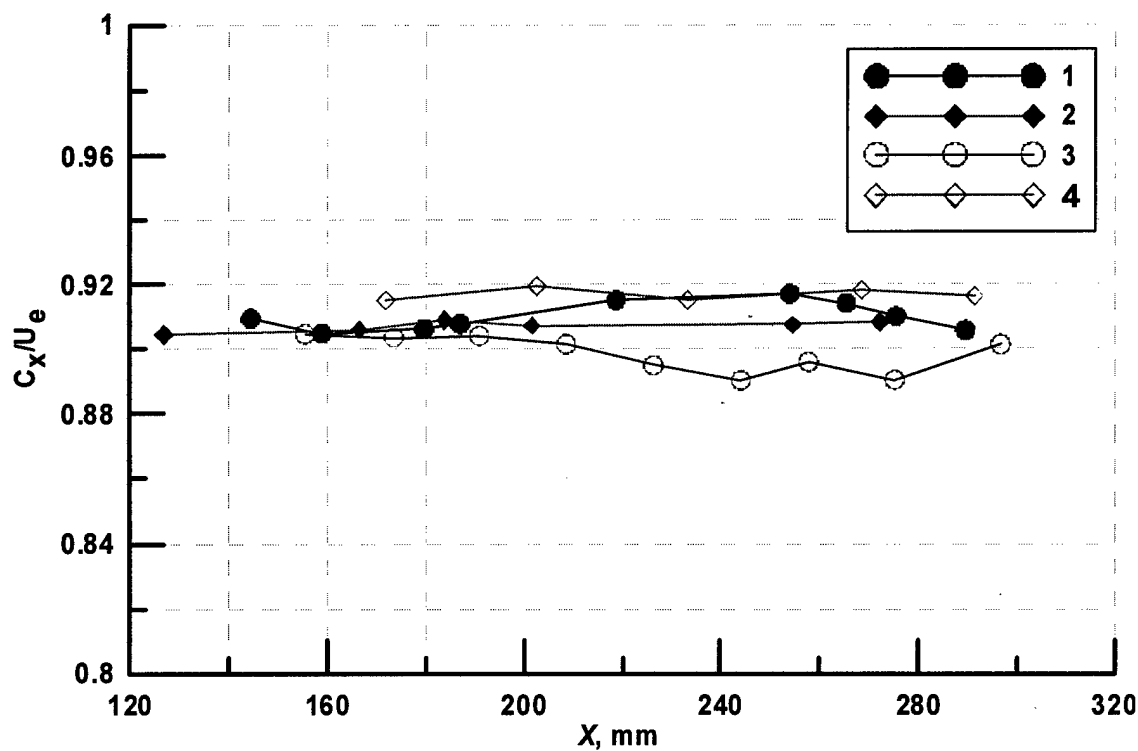


Fig. III.38 Phase speeds of artificial disturbances at  $f = 275$  kHz.

1, 2  $\bar{n}$  solid side; 3, 4  $\bar{n}$  porous side

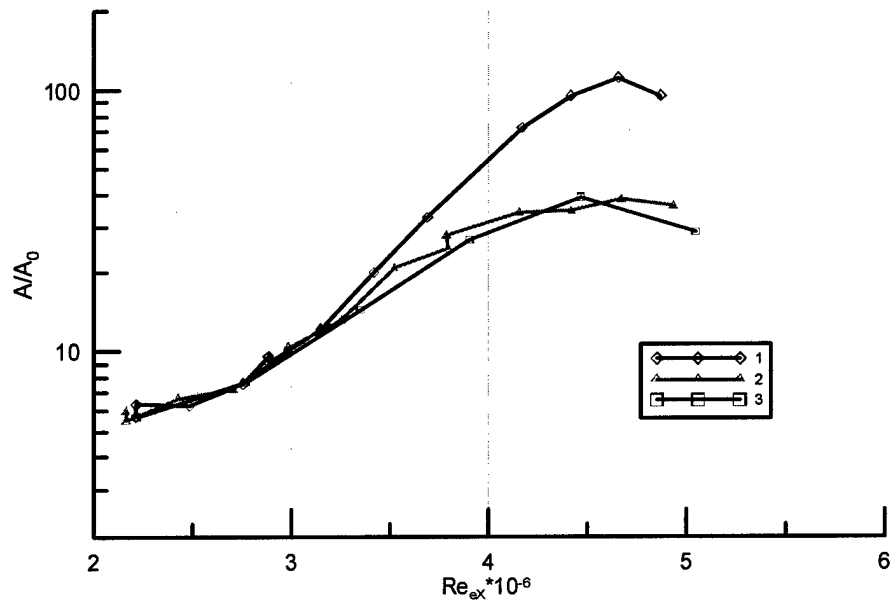


Fig. III.39 Downstream development of the second-mode disturbances of frequency 275 kHz. 1  $\hat{n}$  natural disturbances on solid side; 2  $\hat{n}$  natural disturbances on porous side; 3  $\hat{n}$  artificial disturbance at  $\beta=0$ , porous side

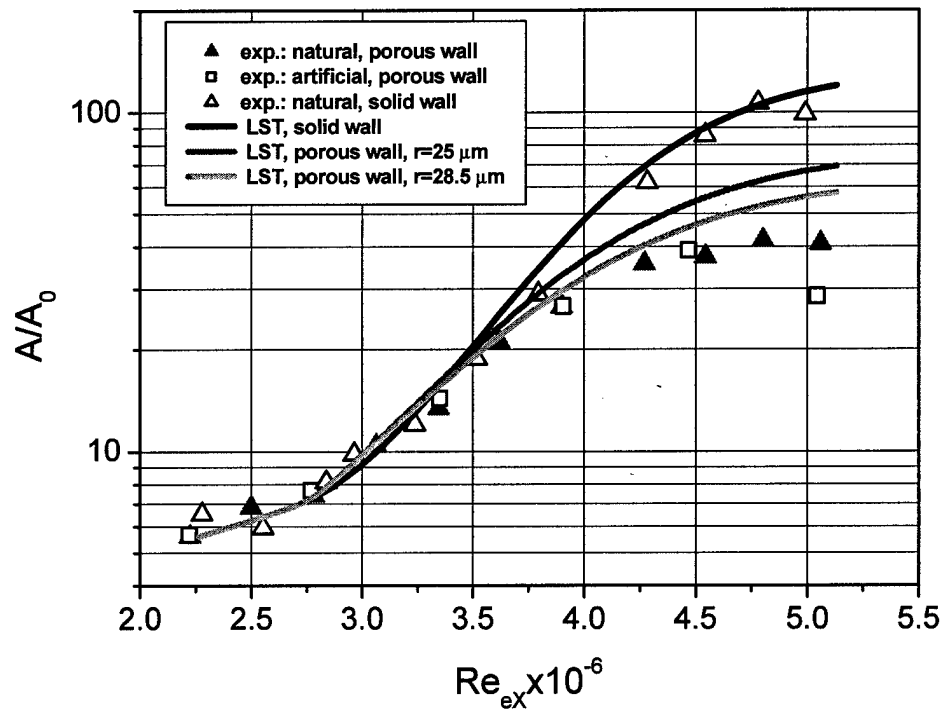


Fig. III.40 Comparison of theoretical amplification curves (lines) with experiment (symbols) for porous and solid sides; disturbances of frequency 275 kHz.

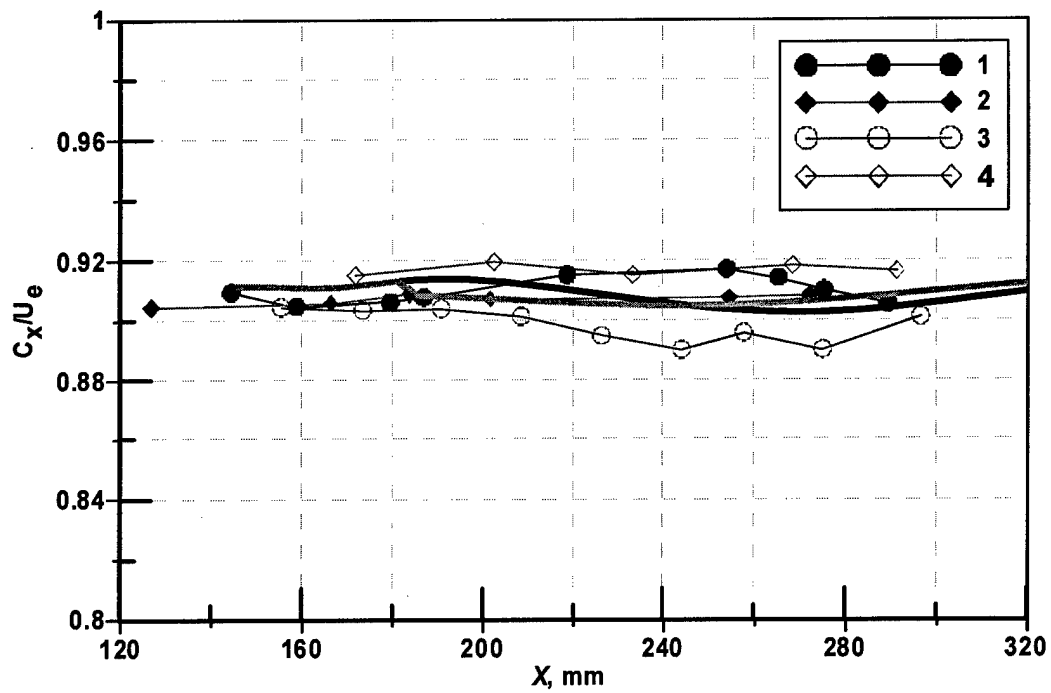


Fig. III.41 Comparison of theoretical phase speeds (black and magenta lines) with experiment (symbols) for artificial disturbances on porous and solid sides;  $\beta = 0$ ,  $f = 275$  kHz.

1, 2  $\rightarrow$  solid side; 3, 4  $\rightarrow$  porous side



## Conclusions

Experimental and theoretical studies of hypersonic boundary-layer stabilization using a passive ultrasonically absorptive coating (UAC) of regular microstructure were conducted in order to evaluate the UAC performance for hypersonic laminar-flow control. The results of these studies are summarized as follows:

1. Linear stability problem for three-dimensional disturbances in two-dimensional boundary layers on a porous wall was formulated in the framework of the asymptotic method of multiple scales. This problem differs from the typical stability problem because of new boundary conditions associated with absorption of disturbance energy by a porous coating. The boundary conditions are formulated in terms of the porous-wall acoustic admittances, which depend on the UAC microstructure.
2. Acoustic properties of a cylindrical pore were analyzed in the framework of linear acoustic theory. Dependencies of the dynamic density and dynamic compressibility on gas pressure and disturbance frequency were derived including the gas rarefaction effects. The analysis is focused on the most practical case when the molecular mean free path is smaller (or much smaller) than the pore radius. Calculations indicate that acoustic properties of the perforated panel essentially depend on Knudsen number in practical ranges of pressure and frequency.
3. Parametric calculations of the UAC effect on the second-mode stability are performed for the T-326 wind tunnel conditions including the gas rarefaction effect. In the case of adiabatic wall, the net stabilization effect is small or even negative for disturbances of relatively small frequencies. The UAC stabilization dramatically increases as the wall temperature ratio decreases. This trend is preferable for practice because surfaces of actual hypersonic vehicle are maintained at low wall-temperature ratios.
4. The rarefaction effect is appreciable for the T-326 conditions. The presence of the Knudsen layer on the pore wall leads to deeper penetration of disturbances into pores and provides stronger stabilization of the second mode.
5. The acoustic interferometer has been developed for benchmark measurements of acoustic characteristics of porous materials within the range of frequencies of 0.6 ÷ 8.5 kHz and air pressures of 760 ÷ 30 torr. In this range of parameters, the wave resistance and propagation constant were measured for the UAC of regular microstructure, namely, the metal sheet perforated with equally spaced cylindrical blind micro-holes.
6. The theoretical model, which is based on the unit problem describing propagation of acoustic disturbances in a long cylindrical tube, was used for prediction of the UAC impedance and absorption coefficient. The benchmark measurements agree well with theoretical predictions.
7. The theoretical model gives a similarity law, which allows for extrapolation of benchmark data to low pressures and high frequencies typical for hypersonic wind tunnel tests and flight. Using a combination of theory and benchmark experiment, it is feasible to design ultrasonically absorptive coatings and evaluate their performance for hypersonic laminar flow control.
8. A model of a  $7^\circ$  half-angle sharp cone with the UAC of regular microstructure was manufactured. The cone has a longitudinal half of its surface solid and the other a porous sheet perforated with equally spaced blind cylindrical holes of the average pore diameter 50

$\mu\text{m}$ , depth 450  $\mu\text{m}$  and average spacing 100  $\mu\text{m}$ . The cone was tested in the T-326 hypersonic wind tunnel at freestream Mach number 5.95. Stability measurements in the boundary layer on the porous and solid cone surfaces were conducted using hot-wire anemometry. Spectra of natural and artificially excited wave packets were obtained at various cross sections of the cone. The wave packets were generated by periodic glow discharge of a fixed frequency.

9. Measurements of mean profiles and RMS mass-flow pulsations showed that the boundary layer was laminar on the solid and porous sides at all cross-sectional stations. The porous coating did not affect the mean flow and RMS pulsations; i.e., the UAC roughness did not cause premature tripping of the boundary layer.
10. Under natural conditions, the first (low frequency) and second (high frequency) modes were observed in the boundary layer. Analysis of the natural-disturbance spectra showed that the second mode was a dominant instability on the solid side. The UAC stabilizes the second mode and weakly affects the first mode that is consistent with the theoretical predictions.
11. To evaluate the UAC stabilization effect, the wave packet was artificially excited at the frequency 275 kHz relevant to the second-mode instability. It was found that the two-dimensional wave is a dominant component of the wave packet. The amplification of this component practically coincides with the amplification of natural disturbance of the same frequency. This confirms that natural disturbances of the high-frequency band are predominantly two-dimensional waves relevant to the second-mode instability. It was shown that the UAC leads to substantial decreasing of the wave-packet growth: the maximum amplitude on the porous side is approximately 3 times lower than that on the solid side.
12. Stability calculations were conducted for the second-mode two-dimensional wave of frequency 275 kHz and compared with experimental data. The theoretical amplification curve agrees well with the experiment on the solid side. The amplification curve calculated for the porous surface passes above the experimental points; i.e., the theory underestimates the UAC stabilization effect. With the correction accounting for conical shape of actual pores, the agreement is satisfactory. It is assumed that the discrepancy between theory and experiment in the downstream measurement station is due to nonlinear effects.

In summary, the LST model, benchmark measurements of acoustic absorption by the porous coating samples and stability measurements on a sharp cone in Mach=6 wind tunnel confirmed the concept of hypersonic boundary-layer stabilization using passive porous coatings of regular microstructure. Theoretical and experimental results of this effort can be used for evaluation of the UAC performance and design of hypersonic laminar flow control systems.

## Future Effort

The following issues need to be addressed in further studied:

1. The wall temperatures of actual hypersonic vehicles are substantially lower than the adiabatic wall temperature. Stability calculations showed that the UAC performance dramatically increases as the wall temperature ratio decreases. These theoretical predictions need to be verified by stability experiments on the model with cooled wall. Such experiments can be conducted in the T-326 Mach=6 wind tunnel of ITAM.
2. Roughness of the porous coating may lead to premature tripping of the boundary layer. Detailed studies of this detrimental effect on stability and transition are required to formulate tolerances on pore size and spacing.
3. It remains to be shown that the second-mode stabilization leads to the increase of laminar run. At present, we have only indirect experimental evidence in favor of this connection. Namely, the experiments in the GALCIT T-5 shock tunnel of Caltech (Rasheed *et al.*, 2001) showed significant increase of the transition Reynolds number on the porous surface. Further experimental studies are needed to clarify this issue.
4. Systematic benchmark measurements of acoustic properties of various porous materials may help to identify optimal UAC microstructures. Such measurements can be performed in ITAM using the acoustic interferometer discussed in Chapter II of this report.
5. Further refinements of the theoretical model are also needed to address the pore end effects and treat acoustic disturbances in porous materials of complex microstructure. The theory may be verified by the benchmark experiments of Item 4.

## References

- Abramowitz, M. & Stegun, I. A.** 1964 *Handbook of mathematical functions with formulas, graphs and mathematical tables*. National Bureau of Standards, Applied Mathematical Series.
- Allard, J.-F. & Champoux, Y.** 1992 Empirical equations for sound propagation in rigid frame porous materials. *J. Acoust. Soc. Am.* **91**, No. 6, pp. 3346-3353.
- Attenborough, K.** 1987 On the acoustic slow wave in air-filled granular media. *J. Acoust. Soc. Am.* **81**, No. 1, pp. 93-102.
- Benade, A.H.** 1968 On the propagation of sound waves in a cylindrical conduit// *Journal of the Acoustical Society of America*, Vol.44, No2, pp. 616-623
- Biot, M.A.** 1956a Theory of propagation of elastic waves in a fluid-saturated porous solid. Part 1. Low-frequency range. *J. Acoust. Soc. Am.*, **28**, No. 1, pp. 168-178.
- Biot, M.A.** 1956b Theory of propagation of elastic waves in a fluid-saturated porous solid. Part 2. High-frequency range. *J. Acoust. Soc. Am.*, **28**, No. 2, pp. 179-191.
- Bogolepov, I.I.** 1986 Sound protection in industry. Theory, researches, designing. Leningrad: Shipbuilding, 428 pp.
- Carpenter, P.W. & Porter, L.J.** 2001 Effects of passive porous walls on boundary-layer stability. *AIAA J.* **39**, No. 4, pp. 597-604.
- Chang, C-L., Malik, M.R., Erlebacher, G., & Hussaini, M.Y.** 1991 Compressible stability of growing boundary layers using parabolized stability equations. *AIAA Paper* 91-1636.
- Daniels, F.B.** 1950 On the propagation of sound waves in a cylindrical conduit// *Journal of the Acoustical Society of America*, Vol.22, pp. 563-564
- Delany, M.A. & Bazley, E.N.** 1970 Acoustic properties of fibrous absorbent materials. *Appl. Acoust.* **3**, pp. 105-116.
- Demetriades, A.** 1974 Hypersonic viscous flow over a slender cone. Part III: Laminar instability and transition. *AIAA Paper* No. 74-535.
- Deryagin, B.** 1946 Specific surface of porous and dispersion bodies measurements by means of determination of rarefied gas flow resistivity. *Doklady Akademii Nauk SSSR, Fizicheskaya Khimiya*, vol. LIII, No. 7, pp. 627-630 (in Russian).
- Dulnev, G.N., Zarichnyak, & Ju.P.** 1974 *The heat conductivity of mixtures and composite materials*. Leningrad, Publishing House iEnergia (in Russian).
- El-Hady, N.M.** 1980 On the stability of three-dimensional compressible nonparallel boundary layers. *AIAA Paper* No. 80-1374.
- Fedorov, A.V. & Khokhlov, A.P.** 2002 Receptivity of hypersonic boundary layer to wall disturbances. *Theoret. Comput. Fluid Dynamics* **15**, No. 4, pp. 231-254.

**Fedorov, A. V. & Malmuth, N. D.** 2001 Stabilization of hypersonic boundary layers by porous coatings. *AIAA J.* **39**, No. 4, pp. 605-610.

**Fedorov A., Shiplyuk, A., Maslov, A., Burov, E., & Malmuth, N.** 2003a Stabilization of high speed boundary layer using a porous coating, *AIAA Paper* No. 2003-1270, Reno NV, Jan. 6-9.

**Fedorov, A., Shiplyuk, A., Maslov, A., Burov, E., & Malmuth, N.** 2003b Stabilization of a hypersonic boundary layer using an ultrasonically absorptive coating. *Journal of Fluid Mechanics*, **479**, pp. 99-124.

**Gaponov, S.A.** 1971 Influence of porous layer on boundary layer stability. *Izv. SO AN SSSR. Ser. Tekh. Nauk* **1**, No. 3, pp. 21-23 (in Russian).

**Gaponov, S.A.** 1975 Influence of gas compressibility on stability of boundary layer on porous surface at subsonic speeds. *Zhurnal Prikl. Mekh. i Tekh. Fiz.* No. 1, pp. 121-125 (in Russian).

**Gaponov, S.A.** 1977 Stability of supersonic boundary layer on porous wall with heat conductivity. *Izv. AN SSSR. Mekh. Zhidkosti i Gaza*, No. 1 (in Russian).

**Gaponov, S.A.** 1980 Effect of nonparallel flow on propagation of disturbances in a supersonic boundary layer. *Izv. AN SSSR. Mekh. Zhidkosti i Gaza*, No. 2, pp. 26-31 (in Russian).

**Gaster, M.** 1974 On the effects of boundary-layer growth on the flow stability. *J. Fluid Mech.* **66**, pp. 465-480.

**Goodman, F. O. & Wachman, H. Y.** 1976 *Dynamic of gas-surface scattering*, Academic Press, N.-Y.

**Grigoriev, V.D., Klemenkov, G.P., Omelaev, A.I. & Kharitonov, A.M.** 1972 Hypersonic wind tunnel T-326. In *Aerofizicheskie Issledovaniya* (ed. A.M. Kharitonov), pp. 16ñ18. Novosibirsk (in Russian).

**Gushchin, V.R. & Fedorov, A.V.** 1989 Asymptotic analysis of inviscid perturbations in a supersonic boundary layer. *Zhurnal Prikl. Mekh. i Tekh. Fiz.*, No. 1, pp. 69-75 (in Russian).

**Hayes, W.D. & Probstein, R.F.** 1959 *Hypersonic flow theory*. Academic Press, New York.

**Johnson, D.L., Koplik, J. & Dashen, R.** 1987 Theory of dynamic permeability and tortuosity in fluid saturated porous media. *J. Fluid Mech.* **176**, pp. 379-402.

**Kendall, J.M.** 1967 Supersonic boundary layer stability experiments. *Proceedings of Transition Study Group Meeting*, Vol. II, ed by W.D. McCuauley, Aerospace Corp., San Bernardino, CA.

**Kendall, J.M.** 1975 Wind tunnel experiments relating to supersonic and hypersonic boundary-layer transition. *AIAA J.* **13**, No. 3, pp. 290-299.

**Kimmel, R.L.** 2003 Aspects of hypersonic boundary-layer transition control. *AIAA Paper* No. 2003-772, Jan. 6-9, Reno NV.

**Kimmel, R., Demetriades, A. & Donaldson, J.** 1995 Space-time correlation measurements in a hypersonic transitional boundary layer. *AIAA Paper* No. 95-2292.

- Kirchoff, G.** 1868 über den einfluss der wärmeleitung in einem gase auf die schallbewegung. *Poggendorfer Annalen*, **134**, pp. 177-193.
- Kosinov, A.D., Maslov, A.A. & Shevelkov, S.G.** 1990 Experiments on the stability of supersonic laminar boundary layers. *J. Fluid Mech.* **219**, pp. 621-633.
- Kundt, A. & Warburg, E.** 1875 On friction and thermal conductivity in rarefies gases. *Phil. Mag.*, **50**, p. 53.
- Lecoudis, S.G.** 1978 Stability of boundary layers over permeable surfaces. *AIAA Paper* No. 78-203.
- Lin, T.C., Grabowsky, W.R., & Yelmgren, K.E.** 1984 The search for optimum configurations for re-entry vehicles. *J. Spacecraft and Rockets*, **21**, No. 2, pp. 142-149.
- Lysenko, V.I. & Maslov, A.A.** 1984 The effect of cooling on supersonic boundary-layer stability. *J. Fluid Mech.* **147**, pp. 38-52.
- Mack, L.M.** 1984 Boundary-layer stability theory. Special Course on Stability and Transition of Laminar Flow, edited by R. Michel, AGARD Rep. No. 709, pp. 3-1 to 3-81.
- Malik, M.R.** 1989 Prediction and control of transition in supersonic and hypersonic boundary layers. *AIAA J.* **27**, No. 11, pp. 1487-1493.
- Malik, M.R., Zang, T.A., & Bushnell, D.M.** 1990 Boundary layer transition in hypersonic flows. *AIAA Paper* No. 90-5232.
- Malmuth, N.D., Fedorov, A.V., Shalae, V., Cole, J. & Khokhlov, A.** 1998 Problems in high speed flow prediction relevant to control. *AIAA Paper* No. 98-2695.
- Maslov, A.A., Shpiyuk, A.N., Sidorenko, A.A. & Arnal, D.** 2001 Leading-edge receptivity of a hypersonic boundary layer on a flat plate. *J. Fluid Mech.* **426**, pp. 73-94.
- Maxwell J. C.** 1952 On the condition to be satisfied by a gas at the surface of a solid body. *Scientific Papers*, **2**, Niven, W.D., ed., New York, Dover, p. 706.
- Padhye, A.R. & Nayfeh, A.H.** 1979 Nonparallel stability of three-dimensional flows. *AIAA Paper* No. 79-1278.
- Patterson, G. N.** 1956 *Molecular flow of gases*. John Wiley & Sons. Inc., New York, Chapman & Hall, Lmted, London.
- Rasheed A.** Passive hypervelocity boundary layer control using an ultrasonically absorptive surface. PhDthesis, California Institute of Technology, 2001, 151p.
- Rasheed, A., Hornung, H.G., Fedorov, A.V. & Malmuth, N.D.** 2001 Experiments on passive hypervelocity boundary layer control using a porous surface. *AIAA Paper* No. 2001-0274.
- Reshotko, E.** 1969 Stability theory as a guide to the evaluation of transition data. *AIAA J.* **7**, No. 6, pp. 1086-1091.
- Reshotko, E.** 1994 Boundary layer instability, transition and control. *AIAA Paper* 94-0001.

- Rosin, G.S.** 1972 Measurements of dynamic characteristics of sound absorption coatings. Moscow: Building, 269 pp.
- Rzhevkin S.N.** Lecture course on sound theory. Moscow: MSU. 1960. 335p.
- Shidlovski V.P.** 1965 *Introduction in dynamics of rarefied gas*, Moscow, Nauka.
- Smoluchowski, M. V.** 1899 Über den Temperatursprung bei Wärmeleitung in Gasen. *Akad. Wiss. Wien.* 107, p. 304, 1898; 108, p. 5.
- Strutt, J. (Lord Rayleigh)** 1894 *Theory of Sound*, 2, Dover.
- Stetson, K.F. & Kimmel, R.G.** 1992 On hypersonic boundary-layer stability. *AIAA Paper* No. 92-0737.
- Stetson, K.F. & Kimmel, R.G.** 1992a Example of second-mode instability dominance at a Mach number of 5.2. *AIAA J.* 30, No. 12, pp. 2974-2976.
- Stetson, K.F., Thompson, E.R., Donaldson, J.C. & Siler, L.G.** 1983 Laminar boundary layer stability experiments on a cone at Mach 8. Part 1: Sharp cone. *AIAA Paper* No. 83-1761.
- Stinson, M.R. and Champoux, Y.** 1992 Propagation of sound and the assignment of shape factors in model porous materials having simple pore geometries // *Journal of the Acoustical Society of America*, Vol. 91 No. 12, pp.685-695.
- Tartabini, P.V., Lepsch, R.A., Korte, J.J., & Wurster, K.E.** 2000 A multidisciplinary performance analysis of a lifting-body single-stage-to-orbit vehicle. *AIAA Paper* No. 2000-1045, Jan. 10-13.
- Tumin, A.M. & Fedorov, A.V.** 1982 On the weakly nonparallel effect on characteristics of flow stability. *Uchenye Zapiski TsAGI* 13, No. 6, pp. 91-96 (in Russian).
- Voschukova, E.A.** 1985 Effect of viscosity and thermal conductivity on acoustical characteristics of any sound absorption coatings. Ph. D. Thesis, Moscow, MSU.
- Whitehead, A.** 1989 NASP aerodynamics. *AIAA Paper* No. 89-5013, July.
- Zhigulev, V.N. & Tumin, A.M.** 1987 *Onset of turbulence*. Nauka, Novosibirsk (in Russian).
- Zwikker, C. & Kosten, C. W.** 1949 *Sound absorbing materials*. Elsevier, New York.

## Appendix

$D = d/dy$ ,  $\mu' = d\mu/dT$ ,  $m = 2(e-1)/3$ ,  $r = 2(e+2)/2$ , where  $e = 1.2$  corresponds to the ratio of the second viscosity to the first viscosity  $\mu_2/\mu = \frac{2}{3}e = 0.8$ ;  $\chi = [\frac{R}{\mu} + ir\mathcal{M}_e^2(\alpha U - \omega)]^{-1}$ .

Non-zero elements of the matrix  $\mathbf{H}_0$  in (1.14) are

$$H_{12} = H_{56} = H_{78} = 1;$$

$$H_{21} = \alpha^2 + \beta^2 + i(\alpha U - \omega)\frac{R}{\mu T}, \quad H_{22} = -\frac{D\mu}{\mu}, \quad H_{23} = -i\alpha[(m+1)\frac{DT}{T} + \frac{D\mu}{\mu}] + \frac{RDU}{\mu T},$$

$$H_{24} = i\frac{\alpha R}{\mu} - (m+1)\mathcal{M}_e^2\alpha(\alpha U - \omega), \quad H_{25} = (m+1)\frac{\alpha}{T}(\alpha U - \omega) - \frac{D(\mu' DU)}{\mu},$$

$$H_{26} = -\frac{\mu' DU}{\mu};$$

$$H_{31} = -i\alpha, \quad H_{33} = \frac{DT}{T}, \quad H_{34} = -i\mathcal{M}_e^2(\alpha U - \omega), \quad H_{35} = \frac{i}{T}(\alpha U - \omega), \quad H_{37} = -i\beta;$$

$$H_{41} = -i\alpha\chi(r\frac{DT}{T} + 2\frac{D\mu}{\mu}), \quad H_{42} = -i\alpha\chi,$$

$$H_{43} = \chi[-\alpha^2 - \beta^2 + r\frac{D\mu DT}{\mu T} + r\frac{D^2 T}{T} - i\frac{R}{\mu T}(\alpha U - \omega)],$$

$$H_{44} = -i\chi r\mathcal{M}_e^2[\alpha DU + (\frac{DT}{T} + \frac{D\mu}{\mu})(\alpha U - \omega)],$$

$$H_{45} = i\chi[r\alpha\frac{DU}{T} + \alpha\frac{\mu' DU}{\mu} + r\frac{D\mu}{\mu T}(\alpha U - \omega)], \quad H_{46} = i\chi\frac{r}{T}(\alpha U - \omega),$$

$$H_{47} = -i\beta\chi(r\frac{DT}{T} + 2\frac{D\mu}{\mu}), \quad H_{48} = -i\beta\chi;$$

$$H_{62} = -2\text{Pr}(\gamma-1)\mathcal{M}_e^2 DU, \quad H_{63} = R\text{Pr}\frac{DT}{\mu T} - 2i\alpha(\gamma-1)\mathcal{M}_e^2 \text{Pr} DU,$$

$$H_{64} = -iR\text{Pr}\frac{(\gamma-1)\mathcal{M}_e^2}{\mu}(\alpha U - \omega),$$

$$H_{65} = \alpha^2 + \beta^2 + iR\text{Pr}\frac{(\alpha U - \omega)}{\mu T} - (\gamma-1)\mathcal{M}_e^2 \text{Pr}\frac{\mu'(DU)^2}{\mu} - \frac{D^2 \mu}{\mu}, \quad H_{66} = -2\frac{D\mu}{\mu};$$



$$H_{83} = -i\beta[(m+1)\frac{DT}{T} + \frac{D\mu}{\mu}], \quad H_{84} = i\frac{\beta R}{\mu} - (m+1)\gamma M_e^2 \beta(\alpha U - \omega),$$

$$H_{85} = (m+1)\frac{\beta}{T}(\alpha U - \omega), \quad H_{87} = \alpha^2 + \beta^2 + i(\alpha U - \omega)\frac{R}{\mu T}, \quad H_{88} = -\frac{D\mu}{\mu}.$$

The vector  $\mathbf{G} = \mathbf{H}_1 \mathbf{F}_0$  in (1.18) are expressed as

$$\mathbf{F}_0 \equiv (f_1, f_2, \dots, f_8)^T,$$

$$G_1 = G_5 = G_7 = 0,$$

$$G_2 = \frac{R}{\mu} \left[ \frac{f_1}{T} \frac{\partial U}{\partial x_1} + \frac{V_0}{T} \frac{\partial f_1}{\partial y} + \left( \frac{\gamma M_e^2 f_4}{T} - \frac{f_5}{T^2} \right) \left( U \frac{\partial U}{\partial x_1} + V_0 \frac{\partial U}{\partial y} \right) \right],$$

$$G_3 = \frac{f_1}{T} \frac{\partial T}{\partial x_1} + \gamma M_e^2 f_4 \frac{U}{T} \frac{\partial T}{\partial x_1} - f_5 \frac{2U}{T^2} \frac{\partial T}{\partial x_1} - \left( \gamma M_e^2 f_4 - \frac{f_5}{T} \right) \left( \frac{\partial U}{\partial x_1} + \frac{\partial V_0}{\partial y} \right) \\ - \gamma M_e^2 V_0 \left[ \left( \frac{\partial f_4}{\partial y} - \frac{f_4}{T} \frac{\partial T}{\partial y} \right) - \frac{1}{T} \frac{\partial f_5}{\partial y} + \frac{2f_5}{T^2} \frac{\partial T}{\partial y} \right],$$

$$G_4 = -\frac{1}{T} \left( V_0 \frac{\partial f_3}{\partial y} + f_3 \frac{\partial V_0}{\partial y} \right),$$

$$G_6 = -\frac{R \text{Pr}}{\mu} \left[ -\frac{V_0}{T} \frac{\partial f_5}{\partial y} - \left( \frac{\gamma M_e^2 f_4}{T} - \frac{f_5}{T^2} \right) \left( U \frac{\partial T}{\partial x_1} + V_0 \frac{\partial T}{\partial y} \right) + (\gamma - 1) M_e^2 \left( V_0 \frac{\partial f_4}{\partial y} - \frac{f_1}{T} \frac{\partial T}{\partial x_1} \right) \right],$$

$$G_8 = \frac{R V_0}{\mu T} \frac{\partial f_7}{\partial y}.$$